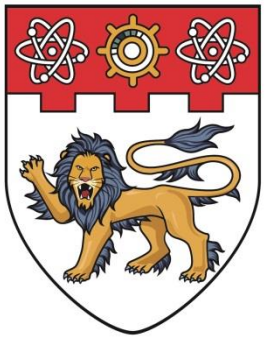

NANYANG TECHNOLOGICAL UNIVERSITY
SINGAPORE

NUMERICAL CHARACTERIZATION OF NANO-DROPLET FORMATION IN 3D NANO-INKJET PRINTING

SUPHANAT APHINYAN

SCHOOL OF MECHANICAL AND AEROSPACE ENGINEERING

2018

NUMERICAL CHARACTERIZATION OF NANO-DROPLET FORMATION IN 3D NANO-INKJET PRINTING

SUPHANAT APHINYAN

School of Mechanical and Aerospace Engineering

A thesis submitted to the Nanyang Technological University
in partial fulfilment of the requirement for the degree of
Doctor of Philosophy

2018

Acknowledgements

First and foremost, I would like to express the deepest gratitude in my life to Her Royal Highness Princess Maha Chakri Sirindhorn of Thailand for granting me the prestigious opportunity to pursue this doctoral degree in the School of Mechanical and Aerospace Engineering at Nanyang Technological University.

Secondly, I would like to express my sincere gratitude to my supervisor, Associate Professor Ng Teng Yong for giving me the great opportunity to do this interesting research project. Not only his expertise and experience in this research area, but also his encouragement, patience, and inspiration truly guided and supported me along the path of my study.

My gratitude also goes to my co-supervisor, Dr. Yeo Jingjie from Agency for Science, Technology and Research (A*STAR) who also guided me with a lot of technical knowledge and precious suggestions. He was an outstanding mentor leading me through the project.

Thirdly, I would like to thank Miss Ang Yun Mei, Elisa and Dr. Geetha Lakshmi who were my colleagues for their encouragement, guidance and support throughout my research. They have brought interesting guidelines to my attention and supported me to achieve this accomplishment.

I would also like to thank my Thesis Advisory Committee (TAC), Associate Professor Wong Teck Neng, Associate Professor Li Hua and the committee chair in my examinations, Associate Professor Tai Kang for their valuable advice.

Furthermore, I must acknowledge the funding that was supported by Singapore Centre for 3D Printing (SC3DP), High Performance Computing Centre (HPCC) and Nanyang Technological University which enabled the completion of these studies.

Last but not least, I would like to specially thank my beloved parents, my beloved aunt and Penn, the only one in my heart. Without moral support from them, I would not able to complete this doctoral study.

ABSTRACT

The process of nano-droplet formation is crucial to the development of 3D nano-inkjet printing. In this thesis, nano-droplet formation is numerically characterized using dissipative particle dynamics (DPD). Due to size constraints and challenges in the development and optimization of 3D nano-inkjet printer nozzles, experimental means to characterize the nano-droplet formation process is currently impractical. Hence, numerical method becomes a valuable tool to characterize this process effectively. Dissipative particle dynamics (DPD) and many-body DPD (MDPD) are employed in this work to study nano-droplet formation process. Such mesoscale particle-based Molecular Dynamics (MD) simulation techniques provide cost effective means to study such systems.

This project starts by investigating agglomeration, which is a process that leads to nozzle clogging in 3D nano-inkjet printing. Nozzle clogging is one of the major hurdle in the development of 3D nano-inkjet printing today. Using DPD, a UV ink system, which comprises of oligomers and monomers of polyethylene glycol (PEG) and polystyrene (PS) with benzophenone (BZP) as the photo-initiator, is modelled. The results show that a 3:1 ratio of PEG to PS provides the best morphology in terms of particle uniformity, agglomerate size, and particulate dispersion. A surfactant, sodium dodecyl sulphate (SDS), is added to the model to improve these agglomeration behaviors. It is found that SDS can help to prevent further agglomeration while reducing the average size of the agglomerates from

520 Å to 440 Å and improving their distribution from 7 clusters to 14 smaller clusters.

Next, a nano-nozzle together with UV ink system is modelled using MDPD to simulate the process of nano-droplet formation through a 3D nano-inkjet nozzle. Comparison with microscale experiment confirms that the model gives good agreement and consistency within 10% range of error. The validated model is subjected to varying temperature and pressure in order to predict the influence of these external parameters on nano-droplet formation. It is found that higher temperatures and applied pressures increase droplet velocity and reduce droplet break-up time. In addition, higher temperatures increase the droplets' diameter while higher effective pressures reduce it. The MDPD simulation also revealed that apart from ink agglomeration, ink deposition on the nozzle's wall is another potential source of nozzle clogging. Simulation results show the addition of surfactant can effectively reduce such ink deposition. Only a small amount of surfactant between the interval of 0.2-3.0 wt% is sufficient to reduce ink deposition by 60%. Increasing the amount of surfactant beyond 3.0 wt% does not give better improvements. To further reduce ink deposition, other de-agglomeration techniques are suggested to modify the interaction between ink and wall of nozzle. This can be achieved via physical or chemical techniques such as electric field or application of a non-wetting coat. By combining these de-agglomeration techniques, it is shown that ink deposition can be reduced by nearly 92%.

Thus, nano-droplet formation in 3D nano-inkjet printing and challenges in its breakthrough such as agglomeration, which can lead to nozzle clogging, may be

numerically studied by MDPD, as a cheaper alternative approach, and providing approximate guidelines for further experimental research and development.

LIST OF PUBLICATIONS

Published Journal Papers

1. **Aphinyan, S**.; Geethalakshmi, K. R.; Yeo, J.; Shakouri, A.; Ng, T. Y. Numerical Characterization of Ultraviolet Ink Fluid Agglomeration and the Surfactant Effect in Nanoinkjet Printing. *Polym. Adv. Technol.* **2017,** 28, (9), 1057-1064.

Journal Manuscripts Waiting for Publication

1. Numerical Study of Surface Agglomeration of Ultraviolet Polymeric Ink and its Control during 3D Nano-Inkjet Printing (The Journal of Polymer Science, Part B: Polymer Physics)

Journal Manuscripts under Review

1. Many-Body Dissipative Particle Dynamics Simulations of Nano-Droplet Formation of Polymeric Ink Fluid in 3D Nano-Inkjet Printing

Peer Reviewed International Conference Papers

1. **Aphinyan S.**, K. R. Geethalakshmi, Yeo J. and Ng T. Y., “Numerical Investigation of Ultraviolet Ink Agglomeration Issues in 3D Inkjet Printing," 2nd International Symposium of Frontiers in Applied Mechanics, China, 7 -10 November 2015.
2. **Aphinyan S.**, Geethalakshmi K. R., Yeo J. & Ng T. Y., "Dissipative particle dynamics study of ultraviolet ink agglomeration in 3D inkjet printing", 2nd International Conference on Progress in Additive Manufacturing, Singapore, 16 - 19 May 2016.
3. **Aphinyan S.**, Elisa Ang Y. M., Yeo J., Ng T. Y., Lin Rongming and K. R. Geethalakshmi, "Numerical Study of Surfactants’ Effect in Surface Agglomeration during 3D Nano-Inkjet Printing by Many-Boby Dissipative Particle Dynamics", 3rd International Conference on Progress in Additive Manufacturing, Singapore, 14 - 17 May 2018.

Table of Contents

TABLE OF FIGURES

TABLE OF TABLES

COMMON ABBREVIATIONS

3D - Three-dimensional

BZP - Benzophenone

CAD - Computer-aided Design

CPU - Central Processing Unit

DEM - Discrete Element Modeling

DOD – Drop on Demand

DPD - Dissipative Particles Dynamics

FDA - Food and Drug Administration

LAMMPS - Large-scale Atomic/Molecular Massively Parallel Simulator

LBM - Lattice Boltzmann Method

MD - Molecular Dynamics

MDPD - Many-Body Dissipative Particle Dynamics

PEG - Polyethylene glycol

PS - Polystyrene

RESS - Rapid Expansion of Supercritical Suspension

RDF - Radial Distribution Function

SDS - Sodium Dodecyl Sulfate

SDSH - SDS’s hydrophilic Head

SDST - SDS’s lipophilic Tail

UV – Ultraviolet

LIST OF IMPORTANT SYMBOLS

Physical Quantities	Symbols
Average Primary Particle Radius	a
Boltzmann Constant	k_B
Bond Dquilibrium Distance	r_0
Bond Potential	U_H
Coarse-graining Parameter	N_m
Conservative Force	$\boldsymbol{F_{ij}^C}$
Conversion Factor	C
Cut-off Radius	$\boldsymbol{r}_c$
Density	ρ
Dissipative Force	$\boldsymbol{F_{ij}^D}$
Distribution Function	ρ
Dissipative Force Coefficient	γ
Effect of Stochastic Interactions	λ
Effective Range of Repulsive Force	r_d
Energy	ε
Flory-Huggins Parameter	χ_{ij}
Fractal Dimension	D_f

Harmonic Bond Force Constant	k_h
H-Monomer Attraction	A_{HM}
H-Oligomer Attraction	A_{HO}
H-T Attraction	A_{HT}
H,T-Wall Attraction	A_{SW}
Gaussian Random Variable	θ_{ij}
Interaction Parameter	a_{ij}
Interfacial Tension	γ
Internal Energy	U
Isothermal Compressibility	κ_T
Liouville Operator	L^C
Liquid-liquid Attraction	A_{ll}
Liquid-liquid Repulsion	B_{ll}
Local Density	ρ_i
Magnitude of Zeta Potential	ξ
Mass	m
Mean Molar Volume	V_{ref}
Molar Volume	V_m
Molecular Weight	M_w
Momentum	$\boldsymbol{p_i}$
No. Density of Molecules	n
No. of Particles in an Agglomerate	N

Pi	π
Position	$\boldsymbol{r_i}$
Pressure	P
Radius of Gyration	R_g
Random Force	$\boldsymbol{F_{ij}^R}$
Random Force Coefficient	σ
Solid-liquid Attraction	A_{sl}
Solid-liquid Repulsion	B_{sl}
Solid-solid Attraction	A_{ss}
Solid-solid Repulsion	B_{ss}
Solubility Parameter	δ_i
Summation of Force	$\boldsymbol{F_{ij}}$
T-Monomer Attraction	A_{TM}
T-Oligomer Attraction	A_{TO}
Temperature	T
Time	t
Time Step	Δt
Unit Factor	$\boldsymbol{e}_{ij}$
Value between 0.101 ± 0.001	α
Velocity	$\boldsymbol{v_i}$
Weight Function of Conservative Force	ω^C
Weight Function of Dissipative Force	ω^D

Weight Function of MDPD's Attraction	$\omega^{C}(r)$
Weight Function of MDPD's Repulsion	$\omega^{d}(r)$
Weight Function of Random Force	ω^{R}
Weight Percent	wt%

CHAPTER 1 INTRODUCTION

This thesis aims to investigate in detail the process of nano-droplet formation, which is important in the development of 3D nano-inkjet printing. The thesis focuses on agglomeration and ink deposition, which is one of the main challenges in the breakthrough of 3D nano-inkjet printing because it can potentially lead to nozzle-clogging. Computational dissipative particle dynamics (DPD) simulation technique, a mesoscale numerical approach, is used in this work due to its cost effectiveness and also because its length and time scale fitted the scope of the problem. In this chapter, the background of the project is introduced, followed by the research objectives and an overview of this thesis report.

1.1 BACKGROUND

1.1.1 Additive Manufacturing

Additive manufacturing is a rapidly developing fabrication technique which is predicted to play a key role in industrial manufacturing. It creates 3D physical objects from the bottom-up by adding each cross-sectional layer of material layer-by-layer [1]. By rapid prototyping of a 3D model in computer-aided design (CAD) software, the complete digital format can be transformed into a physical object in three dimensions. Additive manufacturing provides increased freedom in engineering design as compared to conventional manufacturing techniques, enabling the creation of physical objects in more advance shapes and geometries. There are many different additive manufacturing processes differentiated by the method of creating each layer, such as polyjet (3D inkjet printing), stereolithography, fused deposition modeling, laminated object manufacturing, selective laser sintering, and electron beam melting. Various categories of additive manufacturing processes are shown in Figure 1.1 [2-4].

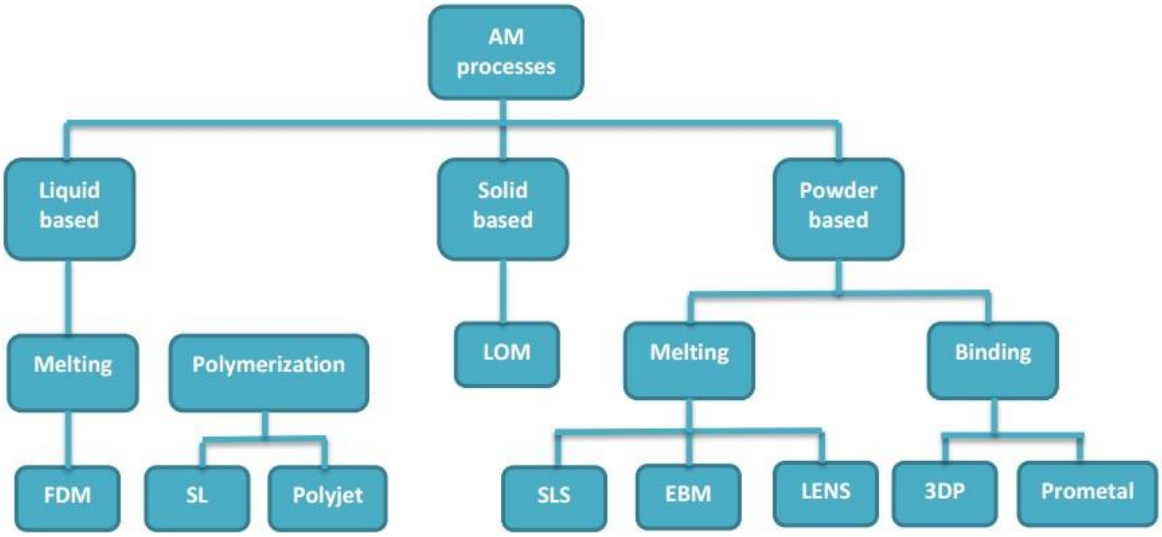

Figure 1.1: Processes in additive manufacturing.

Industrial demand is an important factor driving the continuous development of additive manufacturing. For instance, additive manufacturing can create advanced materials with complex structures in order to fulfill the need in the aerospace industry. This demand is heavily driven by aerospace conglomerates such as NASA, the German Space Center (DLR), Aerojet/Rocketdyne, and Snecma. [5]. Apart from the aerospace industry, additive manufacturing is also important in biomedical applications for the fabrication of tissues and organs to heal the human body [6]. These are some examples of the importance of additive manufacturing to industrial manufacturing and scientific processes.

1.1.2 3D Inkjet Printing

3D inkjet printing is an additive manufacturing technique that combines 3D printing and inkjet printing technology. 3D printing is a process originally invented

at MIT in 1990. The 3D printer prototype deposited powdered material in thin layers which are selectively bound by droplets through continuous-jet inkjet printing. By repeating this layer-by-layer formation, unbound materials could subsequently be removed to obtain a 3D printed object [7]. 3D printing is evolving over three distinct phases [8]. Currently, 3D printing technology is still in the first phase, which is that of prototyping and developing new designs. Changing styles of manufacturing from subtractive to additive techniques eschews traditional processes such as molding, casting, machining, and forming. Thus, final products are not limited by the capabilities of the tools used in the manufacturing processes. If the performance of 3D printing is promoted and enlarged in scale for industrial manufacturing, it will continue to the next phase. The second phase of 3D printing is industrial production of goods that can be finished into final products. As a consequence of direct digital manufacturing, human workforce in almost all manufacturing processes can be reduced, allowing rapid production that will greatly decrease production time while increasing the amount of goods produce. For the last revolutionary phase, 3D printers could be used in almost every house as household appliances. This last phase might be achieved by hugely reducing the production cost of 3D printers and the raw materials required for printing, leading to a direct reduction of its purchase price and operating cost. Almost every house may be no different to a factory in the future.

Inkjet printing is a technology modernized by breakthroughs in 3D printing. Instead of printing on a single plane like a conventional inkjet printer, 3D inkjet printing adds layers of materials on top of each other sequentially until these layers

form a 3D structure [9]. There are two standard types of conventional inkjet technologies: drop on demand (DOD) and continuous inkjet [10]. DOD is a more modern inkjet technology compared to continuous inkjet because multiple nozzles are used in DOD printing with 2 and 3 dimensional applications. Both methods have different manners of generating ink droplets. Uniformly-sized small droplets are produced with high accuracy in the DOD technique by digital signal response. In continuous inkjet, droplet formation is separately generated from a continuous stream of liquid by harmonic modulation of jet velocity. The modulation frequency can be adjusted to provide high speed printing with moderate quality. For DOD inkjet technology, piezoelectric, thermal, and electromagnetic actuators can be applied to control ink drop dispensing and improve the accuracy and precision [11].

Technological advancements in conventional inkjet printers led to its development into 3D inkjet printing. The main advancement was the progress in printhead movement that allows printing in three dimensions. Another important factor was the ability to solidify liquid ink to obtain 3D structural connection of each droplet. These advances allow 3D inkjet printing to possess good speed, high precision, fine details, smooth surface of product, and the flexibility to use various types of printing materials [11]. Because of these advantages, 3D inkjet technology is adopted in many 3D inkjet printer models from additive manufacturing companies such as Polyjet (Stratasys) [12].

1.1.3 3D Inkjet Printing in Nanoscale

The rapid advent and decreasing costs of additive manufacturing are leading to material production in the nanometer scale. A number of printing technologies are currently available for creating submicron physical structures [13] . These structures can be printed using a wide range of materials, from biomaterials to nanomaterials in engineering research and actual manufacturing. While printing in the nanoscale can be generalized to many materials with different properties, an appropriate material may be chosen as a representative prototype. Polymers are ideal materials as they are frequently used in modern additive manufacturing techniques and inkjet printing [10, 14] and they are compatible with many printing methods [13]. Other potential materials include metals and ceramics, but the usage of these materials is constrained by manufacturing complexities such as relatively high processing temperatures. For instance, a temperature of 537K is needed in the crucible for sintering of metal droplets generated from a pneumatic DOD generator [15]. Similar high temperature heat treatment is required in other experimental studies as well [16, 17]. High sintering temperatures are also needed for ceramics and some processing techniques rely on high temperature control of rheological variables to allow proper droplet formation [18-21]. In contrast, polymers can be printed at lower temperatures. For example, polymers can be printed in the form of hot melt inkjet inks that solidify on a substrate [22]. Another method is the printing of polymer colloidal suspensions which deposits the polymer on a substrate after the solvent vaporizes [23, 24]. For 3D inkjet printing, the main type of ink being used nowadays with exceptional performance is

polymeric ultraviolet (UV) curable ink which mainly composes of oligomers, monomers, photo-initiator and additives [25, 26]. The greatest advantage of such ink is its UV light curability. When each layer is completely printed on the substrate, the layer is solidified by UV light layer-by-layer. This allows 3D inkjet printing to be one of the most advance additive manufacturing technologies.

At this moment, one of the main challenges of modern additive manufacturing in nanoscale applications is nozzle clogging due to ink agglomeration [14]. Due to the length scale involved is extremely small, then, experimental appoarch is difficult and expensive, hence, computational characterization can be a potential and more attractive alternative to investigate 3D nano-inkjet printer nozzles to overcome size constraints. In this thesis, nano-droplet formation in these nozzles will be characterized computationally. Rheological properties in relation to nozzle clogging due to ink agglomeration will be investigated. To effectively investigate and study this phenomenon, dissipative particle dynamics (DPD) can be used to provide numerical characterization to determine the dynamic fluid flow and static droplet properties in 3D nanoscale DOD inkjet printing. DPD is a coarse-grain method that allows a reduction of the degrees of freedom for particles , thus overcoming the limit of atomistic length scales in conventional fully atomistic molecular dynamic simulations. Therefore, the advantages of this mesoscale simulation technique is highly compatible for investigating the dynamics of nanoscale inket nozzle clogging.

1.2 SIGNIFICANCE & INNOVATION

Trending to very small scale of resolution in 3D printing, one of the main challenges in the breakthrough of 3D nano-inkjet printing is agglomeration. The problem can potentially disturb printing process and lead to nozzle clogging especially very small scale that it becomes extremely severe. Not only agglomeration but nano-droplet formation is also most important concern in the development of 3D nano-inkjet printing. Due the size constraints and challenges in experimental approaches to optimize 3D nano-inkjet printer nozzles, computational methods seem to offer a more practical alternative than experimental methods which is impractical nowadays. Utilizing the Dissipative Particle Dynamics (DPD) method, it can better significant cost effectiveness in computation compared to classical Molecular Dynamics (MD) as a particle-based mesoscale simulation mean. DPD addresses the limits on the time and length scale inherent in classical MD simulations and provide length and time scale of simulation fitted the scope of the problem by coarse graining and reducing the degrees of freedom for each particle. Moreover, DPD is an obviously suitable computational method for UV curable ink in 3D printing technology with high nature of compatibility because it can effectively capture hydrodynamic behavior of various polymeric systems as its all important details will be presented in the second chapter of this thesis. Thus, DPD simulation method promises to be a good choice providing numerical understanding at low cost with standardly acceptable predictability in comparison.

1.3 RESEARCH OBJECTIVES

This research work composed of three main objectives. The first objective is to numerically investigate the agglomeration morphology of a UV ink model commonly used in 3D inkjet printing through DPD simulation. The agglomeration behavior of components mimicking commercial 3D inkjet ink will be studied to determine methods of preventing and reducing agglomeration and nozzle clogging. The use of additives to stabilize the system, improve rheological properties, and uniformly distribute the particles will be investigated.

The second objective is to numerically characterize nano-droplet formation in 3D nano-inkjet printing. A small nozzle is used to form nano-droplets via many-body dissipative particle dynamics (MDPD) simulation that allows free-surface fluid dynamics between gases and liquids during nano-droplet formation to be implemented. The nano-droplet formation of a polymeric UV ink with proper MDPD parameters is investigated through comparisons with existing experimental results. The effects of important physical parameters in nano-droplet formation, such as temperature and pressure will also be studied.

The last objective is to investigate the dynamics of polymeric ink deposition on the nozzle's wall, which is also a potential source for nozzle clogging especially at the tip of the nozzle. The effects of surfactant on such depositions during the nano-droplet formation process will also be studied. The study will be done for both the general case of a UV ink based on proper MDPD parameters in order to understand the effect of each attraction parameter and a specific case of a commercial ink in order to determine the actual dynamics of the

ink and nozzle in industrial applications. Additives such as surfactants can be a physical strategy to de-agglomerate the particles. Combinations of physical and chemical conditions will enable greater optimization of the printing process by reducing agglomeration in printing fluid before printing and enhancing properties such as the smoothness of droplet deposition for greater uniformity and quality.

1.4 THESIS OVERVIEW

This thesis is organized as follows. All the simulation methods and fundamental knowledge is presented in Chapter 2. The research methodology and simulation results for achieving each objectives is discussed in Chapters 3, 4, and 5 respectively. The study of agglomeration morphology of a UV ink model commonly used in 3D inkjet printing is laid out in Chapter 3. Numerical characterization of nano-droplet formation in 3D nano-inkjet printing is described in detail in Chapter 4. Finally, the effects of surfactants during nano-droplet formation to reduce and control agglomeration is discussed in Chapter 5. Chapter 6 will finally conclude all the important findings, recommendations and future impact of the thesis.

CHAPTER 2 LITERATURE REVIEW

The literature review begins by looking at the different UV ink compositions typically used in inkjet inks. The agglomeration of nanoparticles will then be discussed with a focus on agglomeration of polymeric ink system. The different numerical techniques that have been used to study the agglomeration process will additionally be introduced. Next, the concepts of dissipative particle dynamics (DPD) simulation will be reviewed and the general concepts of polymer simulations through DPD techniques will be given. Lastly, the need for many-body dissipative particle dynamics (MDPD) to better model the free surface problem in nano-droplet formation is explained.

2.1 UV INK COMPOSITIONS

Due to the wide variety of inkjet ink compositions, it is important to choose the most relevant type. There are four categories of inkjet ink: phase-change, water-based, solvent-based, and ultraviolet (UV) ink. Phase-change inks are a poor choice for extremely small nozzles because they are hot melt inks requiring high temperatures and nozzle clogging can occur easily [22]. Solvent-based inks either dry too rapidly creating nozzle clogging, or dry too slowly causing imperfections in the 3D printed product [27]. Water-based inks require porous substrates which are unsuitable for industrial applications because of incompatibility between industrial printheads and formulation of water-based ink. Like solvent-based ink, these inks are also difficult to dry or cure into solid state. Water- and solvent-based inks also require more extraction to get rid of the solvent and the water [28]. In contrast, UV curable ink can provide better reliability to a printhead and is more appropriate for 3D nano-inkjet printing. For example, UV ink does not evaporate so it is easy to control the amount of printed droplet. It also provides faster printing speed, wider range of use of rigid substrates and better shade of colors because of implementation of photopolymers. Another advantage is that it can be cured easily and rapidly by exposure to UV light [29]. These advantages led to greater support of UV ink or photopolymeric ink in commercial 3D inkjet printers such as the Polyjet from Stratasys, photopolymerization desktop printers (The Pegasus Touch from FSL3D, XFab and OWL Nano), and Objet Geometries Ltd.'s Polyjet (Eden family). Most photopolymers used in commercial 3D inkjet printing are cured by UV light through photopolymerization [12]. When UV light is radiated on each

layer, photopolymerization begins by an initiation step through a photochemical process, then a propagation step before finishing with a termination step (see Figure 2.1 for illustration). The details of mechanisms is different based on the type of photopolymerization, and this can be mainly categorized into, cationic , anionic and coordination polymerization [30].

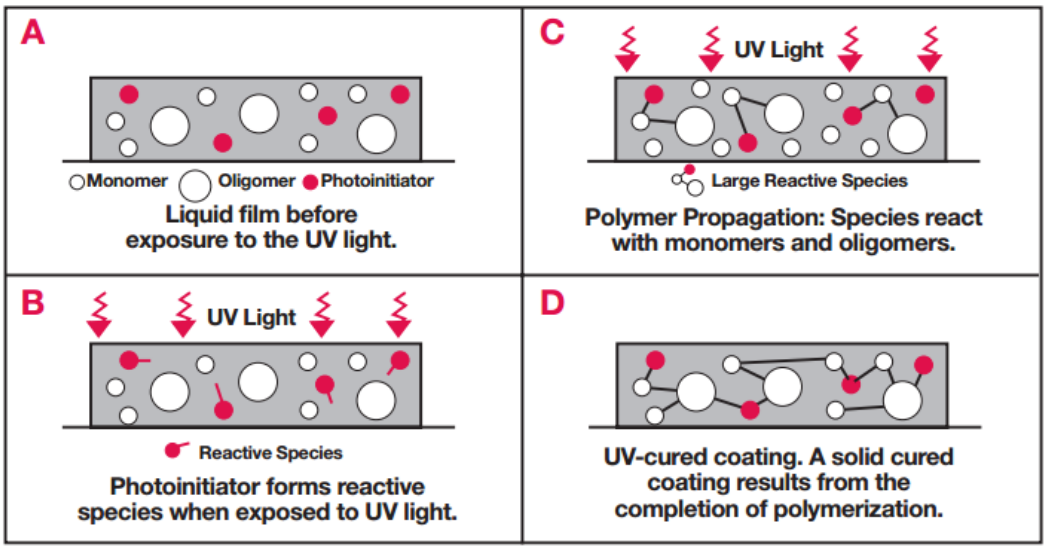

Figure 2.1: Photopolymerization process [31].

From Figure 2.2, UV ink normally composes of oligomers, monomers, photo-initiator, pigments, and additives, with the major component being oligomer of photopolymers [31]. These components are further discussed in the subsections below and the molecular structures used in this study are appeared in Figure 2.3.

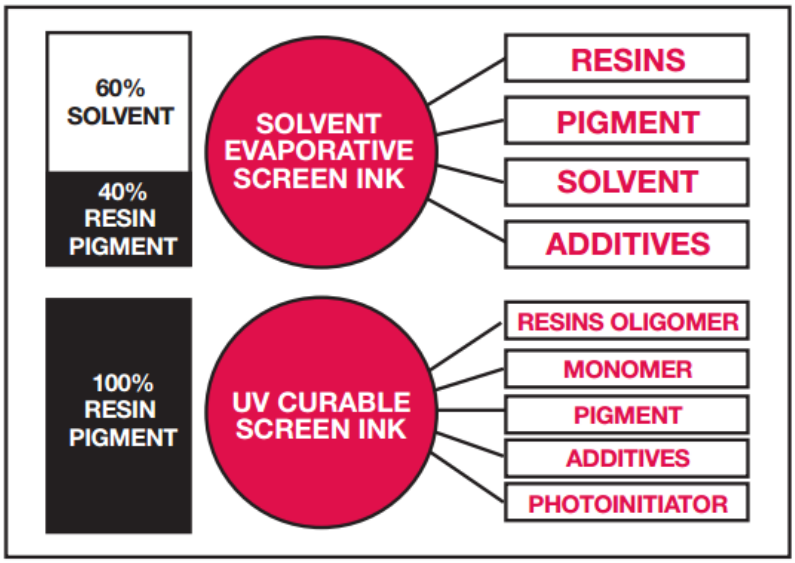

Figure 2.2: UV ink composition vs. solvent-based ink [31].

2.1.1 Polymers, Oligomers, and Monomers

The photopolymers considered here are styrene and ethylene glycol [32-34], which are typically seen in UV ink compositions. Polystyrene is chosen because at present, it is one of the most commonly used commercial photopolymers in 3D inkjet printing. Main properties of polystyrene (PS) are clear, durable, light, good processability, hard, and rather brittle. It is a widely used plastic because of those properties and inexpensive price per unit weight. Due to these advantages, its applications are common in industrial and packaging sectors for many decades. Also, in commercial 3D inkjet printing, polystyrene provides amazing properties in a wide range of outstanding applications [35].

For ethylene glycol, its main function is to lower and optimize the viscosity of UV ink as a viscosity modifier [28, 36-38]. Almost all UV inkjet ink are high viscous fluids because they are mostly composed of polymers. Thus, it is necessary

to have ethylene glycol in the main photopolymer composition to reduce the viscosity. This is especially important in nanoscale 3D inkjet printing as the flow path and nozzles are extremely small. Polyethylene glycol (PEG) is currently mainly applied in the biomedical field for 3D printing. In tissue engineering application, copolymers and blends of other biopolymers with nondegradable PEG have been created, such as block copolymers of PEG with poly(L-lactide) (PLLA), PLGA, and PCL to increase wettability, biocompatibility, or softness of 3D-printed scaffolds [39, 40]. PEG and polypropylene glycol (PPG) are FDA-approved because of their superior biocompatibility and biodegradability in biomedical applications to create high quality, biocompatible and biodegradable 3D printing of synthetic tissue scaffolds [41].

PEG and PS are not only considered for commercial 3D printing [35], they are also used in many other interesting applications. It is thought that 3D nano-inkjet printing with PEG and PS may support and improve the product process for some of these applications in the future. For instance, it can be used to fabricate multifunctional micro- and nano-porous structures due to phase separation in immiscible polymer blends of PEG and PS. This is achieved through a new technique of lithography by spin coating of the polymer blend followed by a rinsing of deionized water to eliminate PEG [42]. The periodic striping pattern with microscale pore sizes can be developed on the surface of the thin films by spin-casting polystyrene (PS) and polyethylene glycol (PEG) at a ratio of 70/30 in a 90 wt% benzene solvent. [43]. Another interesting application is as foams, which are highly porous materials with many interesting physical and mechanical properties

such as high stiffness, low specific weight, high thermal conductivity, and high gas permeability [44]. In a similar application, PEG/PS blends that undergo physical CO_2 foaming process display a unique bimodal cellular structure, in which the large-size cells are occupied by PEG particle. Due to the foaming condition, the average size of smallest cells is less than 20 μm [45]. In the case of block copolymers, PEG and PS block copolymers can be used to produce polymersomes: spherical vesicles with a bilayer architecture formed by the self-assembly of amphiphilic block copolymers in an aqueous environment. Its main applications are in drug delivery, cell-tracking, or as nanoreactors [46]. PEG and PS also can be used as commercial resin and graft polymer for polymeric support of solid-phase methods for syntheses of organic compounds and biomolecules such as peptides and oligonucleotides [47].

2.1.2 Photo-initiator

In this model, benzophenone (BZP), a well-known commonly used photo-initiator, is selected as the main photo-initiator. It has been shown that BZP is compatible to be used with PEG and PS in photopolymerization [48, 49].

2.1.3 Surfactant as Additives

Sodium dodecyl sulfate (SDS) is the most widely used of the anionic alkyl sulfate surfactants [50]. SDS is an anionic surfactant which can reduce polymer bead hydrophobicity and create additional support in charge stabilization of the

suspension. It contains amphiphilic properties which have both hydrophilic (polar) head (SDSH) and lipophilic (apolar) tail (SDST) molecules. SDS is considered for use with the polymeric ink system because PEG is polar, whereas PS is non-polar. For BZP, it is slightly non-polar because of C=O bond. Thus, SDS as a surfactant may potentially create good results to the system in term of reducing and controlling agglomeration.

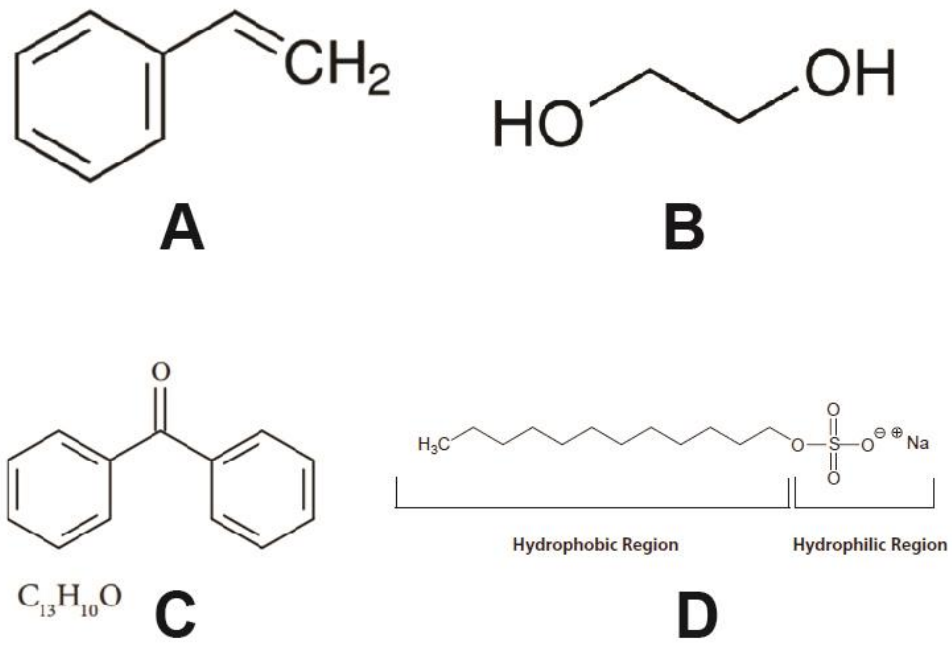

Figure 2.3: Chemical structure of the UV ink's compositions in this simulation. **(A)** Styrene **(B)** Ethylene glycol **(C)** BZP as the photo-initiator **(D)** SDS as the surfactant composing of SDSH and SDST [51].

2.2 AGGLOMERATION OF NANOPARTICLES

Agglomeration of particles is a common phenomenon where tiny particles interact and attach together to form larger agglomerates [39, 40, 52, 53]. Nanoparticles with naturally high surface energy have greater tendencies to form large clusters of agglomerates. These agglomerates need to be broken up and dispersed to maintain the consistency of the system and retain the properties of the nanoparticles [54]. As 3D nano-inkjet printing requires the formation of nano-droplets, polymer agglomeration is an important phenomenon which is crucial for controlling print quality and to prevent nozzle clogging. Due to the difficulty in experimental observations of nanoscale agglomeration, numerical studies become especially useful in understanding such phenomenon. In this section, various numerical studies that were undertaken in published literature to characterize polymer agglomeration is first discussed. The parameters that are found to influence agglomeration are than enumerated and elaborated. Lastly, some techniques that can help to de-agglomerate nanoparticles to prevent nozzle clogging is reviewed.

2.2.1 Numerical Methods used to characterize Polymer Agglomeration

Numerical methods that were used by researchers to characterize polymer agglomeration include discrete element modeling (DEM) [55], molecular dynamics (MD) simulations [56], and mesoscale methods [57-60].

The DEM method was introduced by Cundall and Stack in 1979 [61]. This is a technique that computes each particle's position, velocities and accelerations at each time step, with suitable force models employed, according to Newton's 2nd law. The DEM's main advantage is its ability to resolve rotational motions. However, as it resolves both translational and rotational motions for each particle considered, this is a very computationally expensive method. This method was used by Peng et al in 2010 to study aggregation in nanoparticles suspensions [55]. Specifically, for polymer particles, Kroupa et al studied using DEM the stability of polymer particles colloidal systems. Their research developed a comprehensive force model that can accurately capture the behavior of polymer particles colloidal systems, and investigated the impact of velocity distribution and stability of the colloidal system to agglomeration behavior [62]. Whilst DEM has been shown to accurately model agglomeration behavior, the computation resource needed is a major pitfall of this method. Hence, it is generally restricted to smaller simulation setups.

MD simulation is similar to DEM, but less computationally intensive as it does not take into account rotation degree-of-freedom, and each particle is assumed spherical. It was initially developed by Fermi, Pasta, Ulam and Tsingou in 1955 [63] and the validity of this numerical method was famously confirmed with the accurate prediction of physical properties of liquid argon by Rahman in 1964 [64]. The MD's way to capture microscopic phenomena can be done by computing forces acting on each atom in a system at every time step, and then continuously updating the position and velocity based on the computed forces. The trajectories

of the whole MD system is computed using Newton's 2nd law of motion. With application of necessary conditions such as molecular mechanic force field, boundary conditions, temperature, pressure, ensemble, etc., the dynamic evolution of the system can be obtained through repeated calculation under the algorithm of an integrator's scheme [65]. Although MD is a very useful molecular computational method, it is not suitable in to investigate the nano-droplet formation process, which is a mesoscale phenomena (in the range of 100-1000 nm) [66]. Due to computational cost, conventional fully atomistic MD are fundamentally limited to system sizes that are a few angstrom up to less than a few hundreds of nanometers and time scales that are a few femtoseconds up to below several microseconds [67].

The main drawback of the first two methods is the computational cost. Mesoscale methods aimed to overcome this by increasing the length scale considered beyond atomistic. From Figure 2.4 [68], there are several mesoscale particle-based methods, for example, grid-based techniques such as lattice Boltzmann method (LBM) and particle based method like dissipative particle dynamics (DPD)[57-59]. In this thesis, DPD is the chosen tool for analysis, due to two main reasons. First, although both DPD and LBM are widely applied for soft matter systems, especially colloidal suspensions which is being studied in this thesis, DPD is a off-lattice technique, so it does not incur lattice artifacts and is not affected by restrictions inducted by lattice as in LBM [69]. Second, DPD also conserves momentum with strict Galilean invariant thermostat that is consistent with macroscopic isothermal thermodynamics, and provides better hydrodynamics

result [70, 71]. These makes the application of DPD with polymer ink system more straightforward than LBM and the DPD is potentially one of the best mesoscale simulation techniques [68].

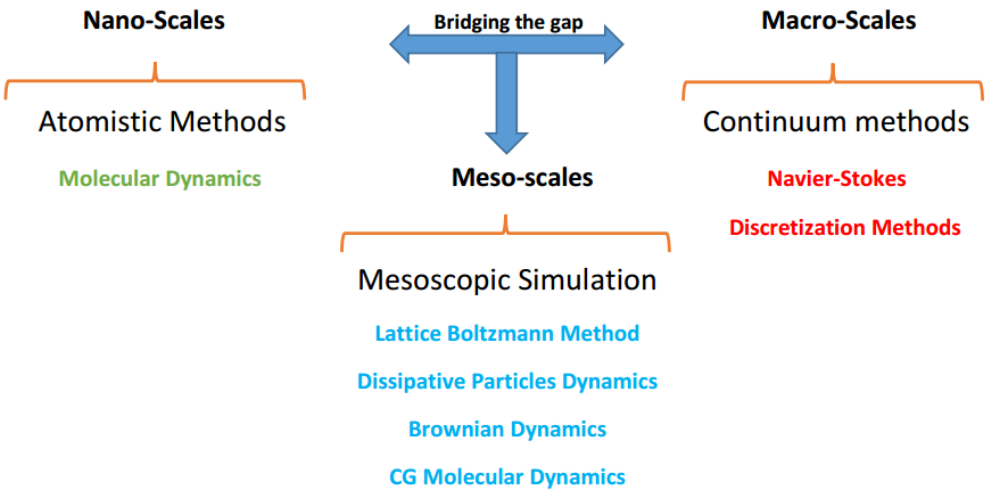

Figure 2.4: Dissipative Particle Dynamics: a mesoscale method for closing the void between the microscales and macroscales.

2.2.2 Parameters that are found to influence Agglomeration

The parameters of interest that has been found to influence agglomeration include temperature and radius of gyration. In terms of temperature, Fiedler et al reported in 2007 that temperature significantly affects agglomeration and it is proportional to the particle's kinetic energy and the coagulation efficiency (see Figure 2.5) [72]. Fiedler et al reported that agglomerates are larger at low temperatures. This is because coagulation of particles tends to occur after collision when kinetic energy of particles in collision is smaller than the effective potentials.

At lower temperatures, particles have low kinetic energy resulting in high agglomeration probability. When the temperature is sufficiently high, colliding particles will have enough energy to depart from the potential well.

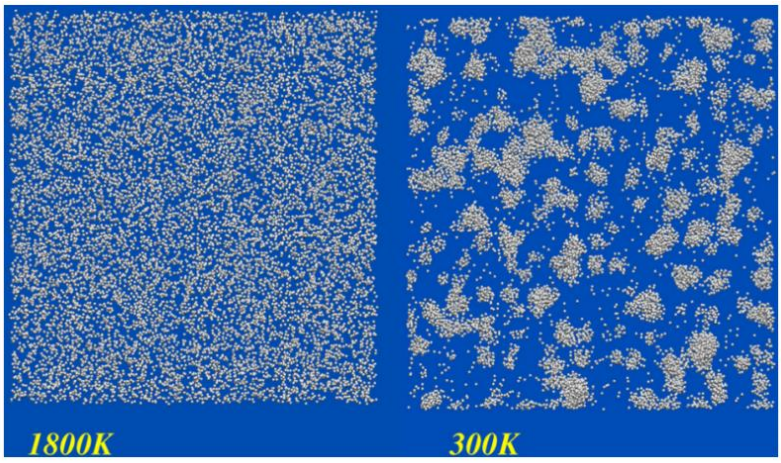

Figure 2.5: The snapshot of equilibrated 13,960 nanoparticles at 1800 K and 300 K [72].

Through the use of MD coupled to a LBM solver, Jimenez [73] found that the number of monomers N in a cluster can be related to the radius of gyration R_g using a power law as shown in Equation 2.1.

$$N = k_f \left(\frac{R_g}{a}\right)^{D_f} \qquad \textit{Equation 2.1}$$

Here, N is the number of particles in the agglomerates; a is the average primary particle radius; D_f is the fractal dimension; and R_g is the radius of gyration that is the parameter that explains radial distance from the rotation point or the center of mass of an agglomerate. Thus, this physical parameter is one of an important tool in order to estimate the size of agglomerate [74-78].

2.2.3 De-agglomeration

Because of the tendency of nanoparticles and molecules to agglomerate and settle, de-agglomeration is important to prevent nozzle clogging. In nanoscale additive manufacturing processes, nozzle clogging can be caused by high loading of nanomaterials due to both agglomeration within the printing materials and elevated velocity of agglomerates as it is illustrated in Figure 2.6. Further research is necessary to determine how different types of nanoparticles affect viscosity and how to induce these suspensions to flow freely though very small printing nozzles [14]. There are several common methods to break up agglomeration of nanoparticles such as rapid expansion of supercritical suspension (RESS), ultrasonication, organic solvents, pH modifiers, and surfactants. RESS harnesses the chemical properties of supercritical fluids or high-pressure gases to separate agglomerates via motion of the fluid through rapid expansion [79]. This method can be applied effectively in the flow path before the nozzle to de-agglomerate and increase uniformity and stability of the printing fluid.

Surfactants are another viable alternative to disintegrate agglomerates. Surfactant and polymer interactions were studied through MD simulations [80] to prevent and stabilize small crystal agglomerates. Together with experiments with laser diffraction, it was observed that surfactants played an important role in controlling the size of the crystals to be significantly smaller than 4.7 μm in suspension. Surfactants also heavily influence the total growth rate of each crystal.

Polymer entanglement can also be a barrier to nanoparticle agglomeration. As polymers have higher molecular weight, increases in their length leads to

greater entanglement among these polymer chains. Nanoparticles would require higher amounts of energy to break the barrier as a result of these entanglements [81].

Ultrasonication is another efficient method in de-agglomeration [82]. Research has revealed the underlying mechanisms of fragmentation by ultrasound based on the energy consumption required to break agglomerates and disperse primary size particles [83]. Agglomerates can be fragmented by their interaction with collapsing cavities in the liquid solution. The main cause of particle disintegration was the high pressure created by imploding cavitation bubbles in their surroundings [84]. Ultrasonication in colloidal suspensions can be used to stabilize dispersed colloids and decrease the size of agglomeration. Continuous ultrasonication can significantly reduce the size of agglomerates and re-agglomeration of particles [85]. Ordinarily, ultrasonication is applied to a solution to create both mechanisms of erosion and fracture. Input energy is transferred to oscillate the liquid and the vibration causes nucleation and implosion of solvent bubbles. Bubbles nucleating and collapsing in the solution can fracture agglomerates effectively.

In order to create stable colloidal dispersions, the fragmentation of nanoparticles is not sufficient. Stabilization of the colloidal dispersions is also vital. Electrostatic fields can be applied in this regard [86-88]. It is essential to collectively consider the properties of solvent, the temperature of the system, and other parameters to ensure the electrostatic field can forestall and limit re-agglomeration. An indicator for sufficient stability of the dispersion system is the

magnitude of the zeta (ξ) potential [89], which is the parameter function of the surface charge on the particles. When the zeta potential is close to zero, the propensity to agglomerate in dispersed system is greater. At highly positive or negative values of zeta potential (less than -30 mV or more than 30 mV) [90], particles in the dispersed system repel each other, resulting in de-agglomeration and the prevention of re-agglomeration. The reason is that electrostatic repulsive forces overcome the attractive van der Waals forces. The practical value of the zeta potential required to prevent re-agglomeration depends on the solvent properties, concentration of ions in the solution, effective pH, and properties of the nanoparticles. One study [85] also recommended that electrostatic stabilization of aqueous dispersions at $\xi = -40\, mV$ can prevent newly formed particles from re-agglomeration. Furthermore, the magnitude of zeta potential at $\xi = -29\, mV$ is able to mechanically break intermediate sized agglomerates.

Figure 2.6: Comparison between individual nanoparticles and agglomerated nanoparticles through the tip of nozzle.

2.3 DISSIPATIVE PARTICLE DYNAMICS (DPD)

DPD simulations can play important roles in understanding the dynamics of droplet formation in 3D nano-inkjet printers. Through coarse-graining, DPD reduces the degrees of freedom of particles by clustering individual atoms into larger particles by averaging their effective conservative interaction potentials between the DPD particles [91, 92]. This approach neglects atomistic details, hence it speeds up computational times and increases computational efficiency. Coarse graining is an intermediate technique of mesoscale simulation to bridge the gap between atomistic and macroscopic simulations [93] as shown in Figure 2.7.

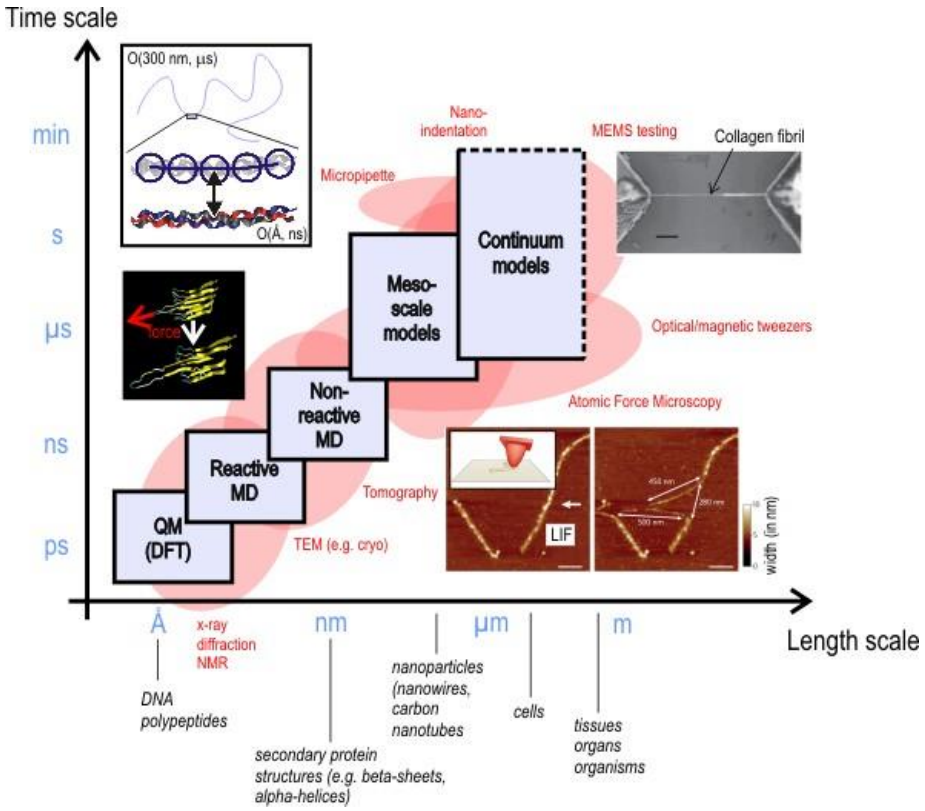

Figure 2.7: Multi scale in modeling [94].

DPD was devised and proposed by Hoogerbrugge and Koelman [95] to model microscopic hydrodynamic systems as stochastic particle simulations for isothermal fluid phenomena. By integrating features of both lattice gas automata and MD, DPD provides higher computational speed than molecular dynamics with more flexibility in simulation of microscopic hydrodynamic behavior than lattice gas automata. These properties are beneficial for the simulation of dispersed systems, especially colloidal suspensions. DPD was refined by Espanol and Warren [96] in 1995. The equations of dissipative and random forces were corrected and energy was conserved. Finally, DPD was fully developed by Groot and Warren [93] in 1997.

The DPD method involves the clustering of molecules into an individual particle as the idea is presented in Figure 2.8 [92], where the number of molecules in each DPD bead is defined as the coarse graining parameter, N_m [97-100]. The computational efficiency of the DPD simulation is increased by soft coarse-grained potentials which allows the moving of beads through between each other instead of the hard potentials such as Lennard-Jones (LJ) potentials [101]. The soft conservative force potentials, as the main advantage of the DPD technique, presents the hydrodynamic nature of mesoscale [92]. The overall simulation speed-up of DPD with respect to fully atomistic MD can be approximated by $1000N_m^{8/3}$ for a given volume [67]. For instance, if N_m equals to 5 and 9, the total speedup factor are roughly 7×10^4 and 4×10^5 respectively.

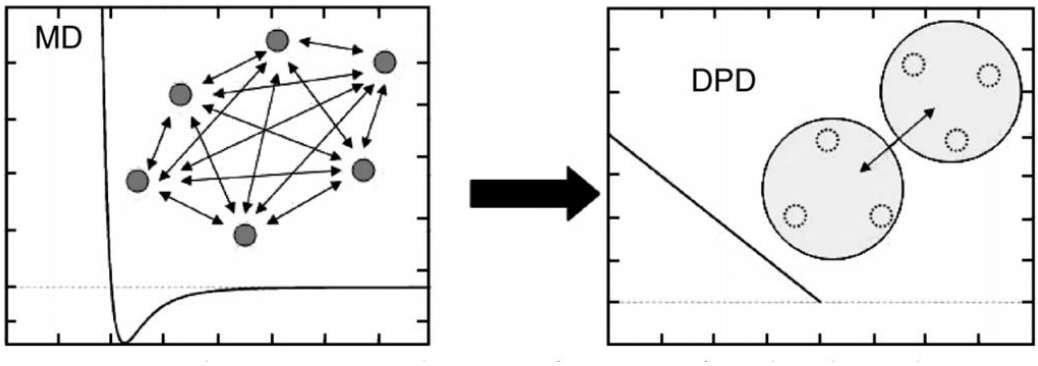

Figure 2.8: DPD particles represent clusters of atoms of molecules. They interact with each other through soft pairwise forces [92].

2.3.1 Theory of Dissipative Particle Dynamics

Similar to MD, the dynamic evolution of each DPD particle follows Newton's second law of motion [95]:

$$\sum_{j \neq i} F_{ij} = \frac{d\boldsymbol{p}_i}{dt} \qquad \textit{Equation 2.2}$$

$$v_i = \frac{d\boldsymbol{r}_i}{dt} \qquad \textit{Equation 2.3}$$

where F_{ij} is the summation of interparticle force exerted on particle i by particle j. $p_i v_i$ and r_i are momentum, velocity and position vectors of particle i respectively. As it was developed by Espanol and Warren [96] in 1995 and Groot and Warren [93] in 1997, the total force of DPD in Equation 2.4 composes of three kinds of forces exerted on each dissipative particle:

$$F_{ij} = F_{ij}^{C} + F_{ij}^{D} + F_{ij}^{R} \qquad \textit{Equation 2.4}$$

where F_{ij}^{C} is the real repulsive conservative force, F_{ij}^{D} is the dissipative force as a fictional effect that degrades velocity deviation among particles and F_{ij}^{R} which is the random force. In Equation 2.5-2.7, these three components of force can be written independently in the term of exerted force of particle i on particle j as

$$F_{ij}^{C} = \omega^{C}(r_{ij})\boldsymbol{e}_{ij} \qquad \textbf{\textit{Equation 2.5}}$$

$$F_{ij}^{D} = -\gamma\omega^{D}(r_{ij})[\boldsymbol{v}_{ij} \cdot \boldsymbol{e}_{ij}]\boldsymbol{e}_{ij} \qquad \textbf{\textit{Equation 2.6}}$$

$$F_{ij}^{R} = \sigma\omega^{R}(r_{ij})\theta_{ij}\boldsymbol{e}_{ij} \qquad \textbf{\textit{Equation 2.7}}$$

where $\boldsymbol{e}_{ij} = \boldsymbol{r}_{ij}/r_{ij}$, $\boldsymbol{r}_{ij} = \boldsymbol{r}_i - \boldsymbol{r}_j$, $r_{ij} = |\boldsymbol{r}_i - \boldsymbol{r}_j|$, and $\boldsymbol{v}_{ij} = \boldsymbol{v}_i - \boldsymbol{v}_j$. In the term of weight functions ω^{C}, ω^{D}, ω^{R} represent conservative, dissipative and stochastic position dependent weight functions respectively. θ_{ij} is a Gaussian random variable with zero mean and unit variance, they are also self-governing for different pairs of particles and at different times [95]. With the symmetry property of $\theta_{ij} = \theta_{ji}$, the total conservation of momentum can be certified with the presence of the following random properties,

$$\langle\theta_{ij}(t)\rangle = 0 \qquad \textbf{\textit{Equation 2.8}}$$

and

$$\langle\theta_{ij}(t)\theta_{kl}(t')\rangle = \left(\delta_{ik}\delta_{jl} + \delta_{il}\delta_{jk}\right)\delta(t - t') \qquad \textbf{\textit{Equation 2.9}}$$

DPD forces interact within a sphere of cut-off radius, $\boldsymbol{r}_c$, which is the range used for computation of conservative and non-conservative forces of the system. The parameters γ and σ are coefficients of the dissipative and random forces respectively. The relationship between these two coefficients is obtained by

Espanol and Warren [97] with the introducing of the Fokker-Plank equation to describe the path of particles in phase space,

$$\frac{\partial \rho}{\partial t} = L^C \rho + L^D \rho \qquad \textbf{\textit{Equation 2.10}}$$

where ρ is the distribution function which gives the probability of a system having particles in position $\boldsymbol{r}_i$, momentum $\boldsymbol{p}_i$ at a discriminative time t, in the form of $\rho(\boldsymbol{r}_i, \boldsymbol{p}_i, t)$. $L^C \rho$ is the Liouville operator of the Hamiltonian system interacting with conservative forces F^C and $L^D \rho$ is also the dissipative and random terms. If dissipative and stochastic forces are set to be zero, $L^D \rho^{eq} = 0$. The Hamiltonian term will have a solution which is the canonical ensemble of Gibbs-Boltzmann distribution,

$$\rho^{eq}(\boldsymbol{r}_i, \boldsymbol{p}_i) = exp(-\textstyle\sum_i \boldsymbol{p}_i{}^2 / 2mk_BT - U/k_BT) \qquad \textbf{\textit{Equation 2.11}}$$

as the solution of $\frac{\partial \rho^{eq}}{\partial t} = L^C \rho^{eq} = 0$.

It was found that there is a necessary condition in order to satisfy the solution of the Fokker-Plank equation and the condition of Gibbsian equilibrium which ensured the balance condition due to the equations of the system that is one of two weight functions, $\omega^D$and ω^R, can be chosen arbitrarily when another one is fixed:

$$\omega^D(r) = [\omega^R(r)]^2 \qquad \textbf{\textit{Equation 2.12}}$$

$$\sigma^2 = \frac{2\gamma k_B T}{m} \qquad \textbf{\textit{Equation 2.13}}$$

Following the Equation 2.12 and 2.13, it is the theorem of fluctuation-dissipation for the DPD simulation where T is the equilibrium temperature of the system and k_B is the Boltzman constant [96]. These equations are similar to a thermostat because they rely on relative velocities and the interactions among particles are

balanced, the hydrodynamics principle was preserved by an isotropic Galilean invariant thermostat that is mainly used to conserve momentum with good consistency to macroscopic isothermal thermodynamics as it was mentioned earlier [102].

Due to the main difference from the hard Lenard-Jones potentials, soft repulsive potential is employed in DPD with the weight function of conservative force defined as a simple function in Equation 2.14,

$$\omega^C(r_{ij}) = \begin{cases} a_{ij}\left(1 - \frac{r_{ij}}{r_c}\right), & r_{ij} \le r_c \\ 0 & , \ r_{ij} > r_c \end{cases} \qquad \textbf{\textit{Equation 2.14}}$$

where a_{ij} is the parameter of repulsive force between particle i and particle j. While the dissipative and random weight functions from the theorem of fluctuation-dissipation previously are in the form,

$$\omega^D(r_{ij}) = [\omega^R(r_{ij})]^2 = \begin{cases} \left(1 - \frac{r_{ij}}{r_c}\right)^s, & r_{ij} \le r_c \\ 0 & , \ r_{ij} > r_c \end{cases} \qquad \textbf{\textit{Equation 2.15}}$$

when the exponent $s = 2$, the expression will be the standard DPD algorithm. And other values of s can be selected to change the fluid viscosity [103, 104].

In order to obtain DPD repulsion parameter, a_{ij}, previously appeared in Equation 2.14, it can be calculated by the relation,

$$p = \rho k_B T + \alpha a \rho^2 \qquad \textbf{\textit{Equation 2.16}}$$

where p is pressure, ρ is a sufficiently high density ($\rho > 2$), and α is a constant that its value can be estimated to a value between 0.101 ± 0.001 . According to the

soft sphere of bead in DPD simulation, the fluctuations in the liquids should be determined through the isothermal compressibility of the system in Equation 2.17 [93].

$$\kappa^{-1} = \frac{1}{nk_BT\kappa_T} = \frac{1}{k_BT}\left(\frac{\partial p}{\partial n}\right)_T \qquad \textit{Equation 2.17}$$

By the definition, κ_T is the usual isothermal compressibility and n is the number density of molecules which is $n = N_m \cdot \rho$ in a unit of r_c^{-3}. According to the study in [67], then,

$$\kappa^{-1} = \frac{1}{k_BT}\left(\frac{\partial p}{\partial \rho}\right)_T \left(\frac{\partial \rho}{\partial n}\right) = \frac{1}{N_m}(1 + 2\alpha a\rho) \qquad \textit{Equation 2.18}$$

As the expression of the relation of the mesoscale simulation parameter and the compressibility of the system. When κ^{-1} is known, the proper value of the DPD conservative force coefficient or the repulsion parameter can be calculated from,

$$a_{ij} = \frac{\kappa^{-1} \cdot N_m - 1}{2\alpha\rho} \qquad \textit{Equation 2.19}$$

It is found that the repulsion parameter is dependent on the coarse-graining parameter, the amount of particles per DPD bead. Using the Flory-Huggins (χ_{ij}) parameters, the repulsion parameter or interaction parameter, a_{ij}, also can be alternatively estimated in easier way following the relationship in Equation 2.20,

$$a_{ij} \approx a_{ii} + 3.27\chi_{ij} \qquad \textit{Equation 2.20}$$

in the case that a_{ii} is the interaction between the same kind of DPD bead [105] according to

$$a_{ii} = 75k_BT/\rho \qquad \textit{Equation 2.21}$$

Here, ρ the particle density that is equal to 3. Thus, the value of a_{ii} is 25 when the cut-off radius and k_BT are reduced to 1.

For the Flory-Huggins (χ_{ij}) parameters itself, the value of each pair of beads can be defined from the solubility parameter and molar volume [106],

$$\chi_{ij} = (\delta_i - \delta_j)^2 V_{ref}/kT \qquad \textit{Equation 2.22}$$

where δ_i and δ_j are solubility parameters of an interacting pair beads ($MPa^{1/2}$)

, and V_{ref} is the mean molar volume of each pair of beads (cm^3/mol).

2.3.2 Integration Algorithms of Dissipative Particle Dynamics

There are many integration algorithms to calculate the trajectories of DPD particles. The Euler method provides new positions and velocities derived from the previous time step of calculation such that

$$\boldsymbol{r}_i(t + \Delta t) = \boldsymbol{r}_i(t) + \boldsymbol{v}_i(t) \cdot \Delta t \qquad \textit{Equation 2.23}$$

$$\boldsymbol{v}_i(t + \Delta t) = \boldsymbol{v}_i(t) + \boldsymbol{F}_i(t) \cdot \Delta t \qquad \textit{Equation 2.24}$$

$$\boldsymbol{F}_i(t + \Delta t) = \boldsymbol{F}_i\left(\boldsymbol{r}_i(t + \Delta t), \boldsymbol{v}_i\ (t + \Delta t)\right) \qquad \textit{Equation 2.25}$$

However, because of drifts in the system's energy and time-irreversible particle trajectories, this method is not ideal. The Verlet algorithm [65] was introduced to enable reversibility of time in MD simulations by updating the positions of particles as

$$\boldsymbol{r}_i(t + \Delta t) = 2\boldsymbol{r}_i(t) - \boldsymbol{r}_i(t - \Delta t) + \frac{1}{M}(\Delta t)^2 \cdot \boldsymbol{F}_i(t) \qquad \textit{Equation 2.26}$$

$$\boldsymbol{F}_i(t+\Delta t) = \boldsymbol{F}_i\big(\boldsymbol{r}_i(t+\Delta t)\big) \qquad \textit{Equation 2.27}$$

The velocity–Verlet algorithm improves the accuracy of particle velocities [107-109] where

$$\boldsymbol{r}_i(t+\Delta t) = \boldsymbol{r}_i(t) + \boldsymbol{v}_i(t)\cdot\Delta t + \tfrac{1}{2}(\Delta t)^2\tfrac{1}{M}\cdot\boldsymbol{F}_i(t) \qquad \textit{Equation 2.28}$$

$$\boldsymbol{F}_i(t+\Delta t) = \boldsymbol{F}_i\big(\boldsymbol{r}_i(t+\Delta t)\big) \qquad \textit{Equation 2.29}$$

Other complex integration schemes are applicable for DPD such as self-consistent Verlet [110], Shardlow's method [111] and the Lowe's method [112]. The accuracy and stability of the integration method in DPD can be measured by investigating the temperature of the system, radial distribution function (RDF), and other properties [68]. The temperature drift and RDF artifacts in the velocity-Verlet scheme can be decreased by adjusting the value of λ, the effect of stochastic interactions. The modified velocity–Verlet algorithm is one of the most efficient integration scheme based on the accuracy and computational cost with the minimal of temperature drift and many artifacts in other proposed methods [93], given by

$$\boldsymbol{r}_i(t+\Delta t) = \boldsymbol{r}_i(t) + v_i\cdot\Delta t(t) + \tfrac{1}{2}(\Delta t)^2\cdot\tfrac{1}{M}\boldsymbol{F}_i(t) \qquad \textit{Equation 2.30}$$

$$\boldsymbol{v}_i'(t+\Delta t) = \boldsymbol{v}_i(t) + \lambda\cdot\tfrac{1}{M}\boldsymbol{F}_i(t) \qquad \textit{Equation 2.31}$$

$$\boldsymbol{F}_i(t+\Delta t) = \boldsymbol{F}_i\big(\boldsymbol{r}_i(t+\Delta t), \boldsymbol{v}_i'(t+\Delta t)\big) \qquad \textit{Equation 2.32}$$

$$\boldsymbol{v}_i(t+\Delta t) = \boldsymbol{v}_i(t) + \tfrac{1}{2}\Delta t\cdot\tfrac{1}{M}[\boldsymbol{F}_i(t) + \boldsymbol{F}_i(t+\Delta t)] \qquad \textit{Equation 2.33}$$

where the term $v_i'(t+\Delta t)$ is predicted to calculate the value of force and then it is corrected subsequently. The parameter λ is used to represent the effect of stochastic interactions in the algorithm. A comparison of these integrators to investigate their performance in DPD [113] showed that utilizing the velocity-Verlet based integration scheme gave good overall performance at a reasonable

computational cost. The Shardlow integrator is based on separating the equations of motion and can be implemented in the framework of DPD. While Lowe's approach is better in order to explain hydrodynamic systems concerning about the period of time of momentum diffusion and mass transfer with respect to the magnitude of colloidal particle.

Polymer ink systems can be modelled as a complex fluid where the modified velocity–Verlet procedure can be utilized with a combination of soft and hard potentials [114]. A larger time step, Δt, is used with the motion of particles of solvent and a smaller time step, δt, for the polymer particles moving within the chain. The positions and velocities of polymers are revised in the following loop that the times of polymer particles $\Delta t/\delta t$ is integrated in an independent sub-cycle with varying polymeric force $\boldsymbol{F}_i^p$ update. Hence the intra-polymer forces are recalculated through the sub-cycle. This procedure is the most straightforward form of time-staggered methods which enables CPU time savings with higher efficiency and accuracy.

2.3.3 Boundary Conditions of Dissipative Particle Dynamics

Because of the soft repulsive force among DPD particles, the fluid particles can penetrate into solid boundaries. Although common implementations of boundary conditions ordinarily used in MD and LBM can also be applied to DPD, it is required to develop and implement the no-slip wall boundary condition by correcting the velocity profile through the common flow field to obtain

impenetrability that is consistent with macroscopic system properties [68]. A large classification of the three main possibilities used to establish DPD boundary conditions was introduced in [115]: avoiding direct modeling of the physical boundary by modifying the periodic boundary conditions, freezing regions of the fluid to create a rigid wall or a rigid body and combining different types of particle layers with proper reflections, bounce-back reflection or Maxwellian reflection.

2.4 POLYMERS IN DPD SIMULATION

Polymer ink systems can be modelled as colloidal systems in the form of DPD beads under the influence of DPD forces, conservative force, dissipative force, and random force. A polymer chain can be modeled as beads of DPD particles bridged by simulated springs. The additional spring force for ordinary DPD interactions creates the exchange of momentum between polymer beads in the chain. Polymer chains can interact through a variety of intra-polymer forces such as Lenard-Jones potential forces, Frenkel (stiff) springs, Hookean springs, worm-like chain forces, or nonlinear elastic (FENE) springs [115].

Previous numerical studies of polymeric system also reported rheological properties of polymers, block copolymers and meso-phase separation, and grafted polymer brush [116]. An example of a polymeric system of inkjet ink modelled through DPD is illustrated in Figure 2.9, where the polymer chains can move freely in a DPD solution [114].

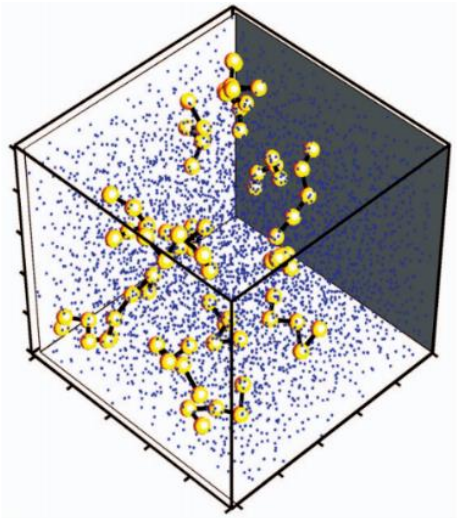

Figure 2.9: Diluted polymer solutions. A solvent contains suspended polymer chains by using dissipative particle dynamics (DPD) particles [114].

These studies also presented some examples of DPD models of surfactant and amphiphile systems as additives to gain more uniformity and prevent agglomeration in the ink system. Moreover there are some DPD work performed on systems of polymer and solvent, for e.g. in [117], where it was shown that solvents that do not possess the correct properties can cause poor polymer dispersion. Numerical techniques can solve these problems with high-throughput investigation of the properties of varying polymer ink systems. A study [118] also investigated the effect of solvent quality which was improved by changing the size of the interactions of repulsion among particles. The behavior of polymer radius of gyration in this study showed the disintegrated condition for transition that occurs when the quality of solvents varies from good quality to poor quality. Another study estimated the viscosity and coefficients of normal stress as functions of the rate of shear by modelling DPD solutions at restricted shear rates [119]. These examples showed that DPD is appropriate to be used to study polymeric system in mesoscale.

2.5 MANY-BODY DISSIPATIVE PARTICLES DYNAMICS (MDPD)

Due to limitations in DPD simulations for studying problems related to free-surface fluid dynamics in the mesoscale, such as interfaces between gases and liquids, DPD needs to be extended to enhance the hydrodynamic behavior of DPD models and modified to allow the study of vapor-liquid equilibria. To enhance the scope of DPD simulations, developments in Many-body Dissipative Particle Dynamics (MDPD) were initiated by Pagonabarraga and Frenkel in 2001 [120]. Subsequently, MDPD was studied and developed further by Troimov *et al* [121] in 2002 and Warren in 2003 [122]. MDPD improves the determination of the thermodynamic behaviors of DPD and imitates the more similar thermodynamic properties of realistic fluid. The scheme of MDPD inherits the three main forces of DPD, which are the conservative force, the dissipative force and the random force (see Equation 2.4).

The main difference between DPD and MDPD is the additional attractive force to enable the modelling of vapor-liquid coexistence. In the conservative force of MDPD, the attractive force is still a function of the weighted average of the local density while an additional repulsive force is included that accounts for density-dependent interactions as it is visualized in Figure 2.10 and Equation 2.34,

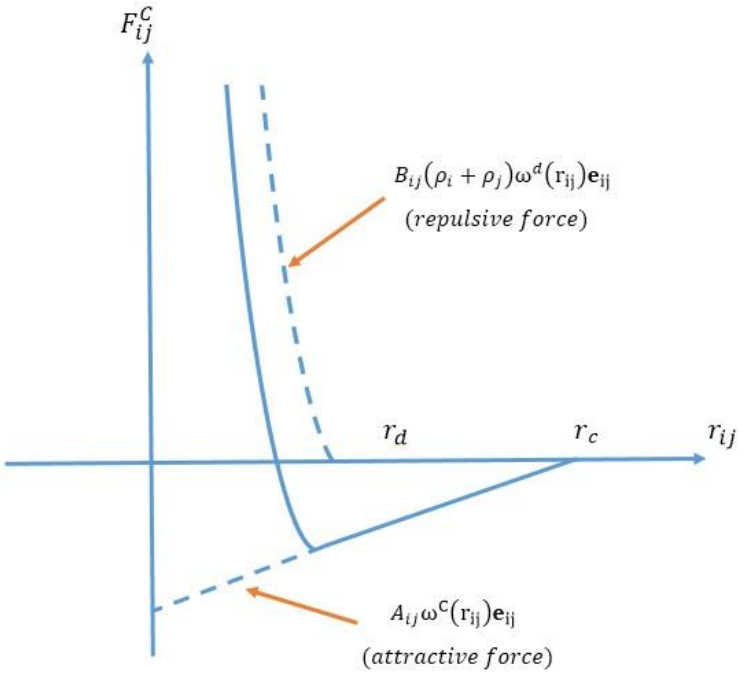

Figure 2.10: The pairwise conservative force of MDPD.

$$F_{ij}^{C} = A_{ij}\omega^{C}(r_{ij})\boldsymbol{e}_{ij} + B_{ij}(\rho_i + \rho_j)\omega^{d}(r_{ij})\boldsymbol{e}_{ij} \qquad \textbf{\textit{Equation 2.34}}$$

$$\omega^{C}(r) = \begin{cases} (1 - r_{ij}/r_c) & if\ r_{ij} < r_c \\ 0 & otherwise \end{cases} \qquad \textbf{\textit{Equation 2.35}}$$

$$\omega^{d}(r) = \begin{cases} (1 - r_{ij}/r_d) & if\ r_{ij} < r_d \\ 0 & otherwise \end{cases} \qquad \textbf{\textit{Equation 2.36}}$$

The weight functions $\omega^{C}(r)$ and $\omega^{d}(r)$ are valid in the conditions of $r < r_c$ and $r < r_d$ respectively as it is shown in Figure 2.11 for the diagram showing MDPD pairwise conservative force between two MDPD beads.

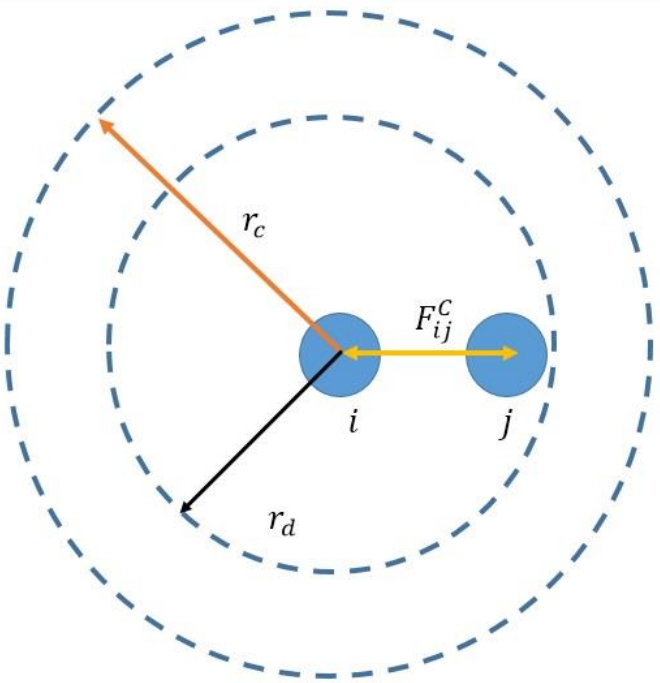

Figure 2.11: The diagram of MDPD pairwise conservative force.

The short range of r_d is less than that the cutoff radius, r_c , and the effective range of repulsive force can be tuned by varying these two values. The local density, ρ_i, can be determined by Equation 2.37.

$$\rho_i = \frac{15}{2\pi r_d^2}\sum_j(1 - r_{ij}/r_d) \qquad \textit{Equation 2.37}$$

The thermostat of MDPD is the same as thermostat of DPD that is theorem of fluctuation-dissipation of DPD simulation previously mentioned in Equation 2.12 and 2.13 which one of two weight functions, ω^D and ω^R, can be chosen arbitrarily when another one is fixed.

Because of vapor-liquid coexistence in MDPD, droplet formation can be modelled. The first form of droplet by MDPD simulation appeared as a pendent

droplet in [122]. By suitable MDPD parameters, pendent droplet of 3,000 particles could be generated in a couple of minutes by adding constant body force per particle to imitate gravitational force along z-direction. Not only the interface of vapor and liquid but the interface of solid and liquid is also needed to be considered for nano-droplet formation. The MDPD parameters' tuning in [123] give a general guideline for attraction parameters of non-wetting fluid and partial wetting fluid to a solid surface, A_{sl}, the attraction range for non-wetting fluid is about -20 while the attraction range of partial wetting fluid is between -32.5 to -25. Another MDPD simulation work which confirmed that MDPD enables vapor-liquid interface is the pinching of a droplet under high strain [124]. In this work, it was shown that a single droplet could be turned into the form of axis-symmetric dumbbell by extensional flow, followed by pinch-off separation. The ability to accommodate vapor-liquid interface makes MDPD a potential modelling method to study nano-droplet formation in 3D nano-inkjet printing.

In MDPD, the effective range of the attractive force is longer than the repulsive force and it is equal to the cutoff radius. Typical MDPD parameters for the cutoff radii r_c is 1 and r_d is 0.75. For convenience in simulation, the mass of all particles, m_i, is usually normalized to 1 and the unit of energy k_BT is also normalized to be 1 [122, 123, 125]. The parameters A_{ij} and B_{ij} are used to vary the maximum amplitudes of the attractive and repulsive forces respectively. The attractive force with $A < 0$ varies linearly with r_{ij}, while the repulsive force with $B > 0$ relies on the local densities and decreases rapidly with increasing r_{ij}. For MDPD, the approximation of the local densities is identical to the summation of

the bound particles. As a result, the condition of vapor-liquid coexistence of MDPD is set to be $A < 0$ and $B > 0$. In most MDPD simulation studies, the attraction parameters A_{ij} are commonly set to be -40.0 in both solid-solid and liquid-liquid interactions ($A_{ss} = A_{ll} = -40$) [122, 123, 125]. For solid-liquid interactions, the attraction parameter, A_{sl}, is often tuned to be in a proper range to improve the simulation results in the static wetting behavior and it is usually set at -40 as the basis value to obtain complete wetting behavior. The standard repulsion parameter, B_{ij}, is 25 [122, 123, 125]. In situations where solid-liquid interactions are considered, the absolute magnitudes of A_{sl} and B_{sl} can be adjusted accordingly to obtain two different hydrodynamic phenomena. On the one hand, if $|A_{sl}| > B_{sl}$, hydrophilic behavior can be modelled because the attractive force between the solid and the liquid is stronger than the repulsive force. On the other hand, hydrophobic behavior can be modelled if $|A_{sl}| < B_{sl}$ because the repulsive force is greater than the attractive force.

In this work, the dissipative force coefficient, γ, is set to be 50.0 instead of the value of 4.5 commonly used in DPD because of the significantly greater density-dependent repulsion of MDPD beads compared to standard DPD repulsion, which can result in high fluctuations in temperature that is similar to the results obtained from a previous study [126]. When the coefficient of the dissipative force is 50.0, the temperature fluctuation is reduced from about 33% to 4%. Thus, the thermostat can stabilize the system's temperature within an acceptable range. The paper [126] also showed that MDPD is capable of capture entanglements and liquid-vapor coexistence in polymeric systems.

2.6 SUMMARY OF LITERATURE REVIEW & RESEARCH GAPS

Presently, inkjet printing technology has already reached nanoscale resolution [127-129]. This advance technology's development can be used in various applications especially in the fabrication of nanoscale circuits by inkjet printing [130, 131]. Similar to progress in nanoscale resolution of inkjet printing, nanoscale 3D printing is also currently in its infancy, and being investigated and developed (for both polymers and metals) in many institutions [131-133]. The progress can be easily transferred unless these two technologies share the same type of ink. Owing to superior dimension in 3D inkjet printing technology, the most prevalent type of ink in 3D inkjet printing is UV curable ink which is easily solidified by UV curing process and its advantages over other kinds of inkjet inks [12, 35, 134, 135]. On the other hand, the advantages of this liquid polymeric ink come with higher opportunity of nozzle clogging due to agglomeration problem. It is well recognized to be the most important issue in additive manufacturing that needs to be resolved for the progress in very small scale [14].

As the main gap in this research field which is necessary to be investigated and resolved, agglomeration was studied in this work in the form of agglomeration morphology in order to understand agglomeration morphology in 3D inkjet printing nowadays. Not only agglomeration morphology but surfactant effect on agglomeration morphology is also a focusing point in this study because agglomeration is needed to be reduced and controlled before the breakthrough. Due to limitation of experimental approach which is impractical nowadays for

nanoscale phenomena, there is no experimental work studying on nano-droplet formation. Thus, simulation approach will be the powerful alternative to preliminarily study the future nano-droplet formation. A mesoscale particle-based simulation method, DPD, is one of the most suitable method that promises for the support of this breakthrough with strong compatibility for almost polymeric systems based on its previous work. With the approximate guidelines, further experimental research and development can be performed with cheaper resources and time.

CHAPTER 3 NUMERICAL CHARACTERIZATION OF ULTRAVIOLET INK FLUID AGGLOMERATION AND THE SURFACTANT EFFECT

This chapter details DPD simulations that examine the stability and agglomeration in an UV ink system commonly used in 3D inkjet printing nowadays, including the effects of additives in reducing agglomeration and increasing stability in the UV ink system.

3.1 INTRODUCTION

As discussed in Chapter 2, even though UV ink fluids are well-known for their outstanding performance in many 3D inkjet or general inkjet applications [136], there exists a major challenge [14] to be addressed in order to make a breakthrough of this technology into nanoscale, which is the issue of ink fluid agglomeration. The UV ink model in this study has similar composition to commercial UV ink commonly used nowadays.

The main constituents of UV ink are oligomer, monomer, photo-initiator, colorants and other additives such as stabilizers and surfactants. Among these ink components, oligomers which is the major composition have highest tendency to agglomerate and agitate the stability and quality of the printing fluid and possibly lead to nozzle clogging. For polymers, oligomers and monomers are styrene and ethylene glycol which are photopolymerizable [32-34], and these are modeled to investigate their agglomeration characteristics. As a matter of fact, understanding the nature of interaction among the constituents of the UV ink fluid is a demanding effort owing to the size of the polymers. The particle-based mesoscale DPD simulation technique offers a method to study this problem of agglomeration issues in UV ink with reasonable computational time. Based on the composition of UV inks, DPD bead is suitable to be formulated to represent a polymeric system [68] and expected to provide understanding in the agglomeration morphology of each simulation study cases.

The DPD simulation in this study was carried out via the Material Studio 8.0 software of Accelrys Inc (BIOVIA 2002-2016) [137]. The coarse-grained models

are generated by directly coarse-graining from the atomistic model. Not only agglomeration morphology but the effect of surfactant is also be investigated in order to reduce and control agglomeration.

3.2 RESEARCH METHODOLOGY

All the molecular models of the UV ink's compositions will be coarse-grained or clustered into DPD beads in order to perform DPD simulations. Each monomer of PEG and PS is coarse-grained as a single collective bead. In this case, each molecule of the photo-initiator is also modelled similarly following Figure 3.1.

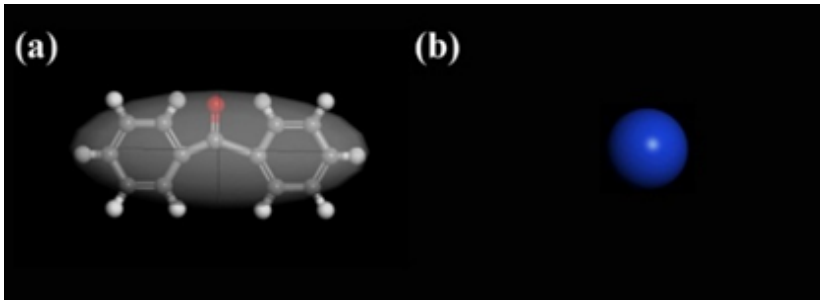

Figure 3.1 : (a) Atomistic model and **(b)** coarse-grained model of BZP as a photo-initiator in Material Studio 8.0.

While oligomers of PEG and PS are modelled as a chain of six connected beads. For the last composition, SDS is used as a surfactant in this model by coarse-graining each molecule into two connected beads labelled as SDST and SDSH in Figure 3.2 (d). It is necessary to coarse-grain the surfactant in this way because this simulation study needs the distinct behavior of both hydrophilic head and lipophilic tail molecules. This special coarse-graining method for surfactant in DPD was reasonably proved in [138] for its simulation performance.

As it is summarized in Figure 3.2, all the models are generated directly by coarse-graining the atomistic models of the corresponding molecules with Material Studio 8.0. The coarse-graining is done following the original process proposed by Hoogerbrugge and Koelman [95].

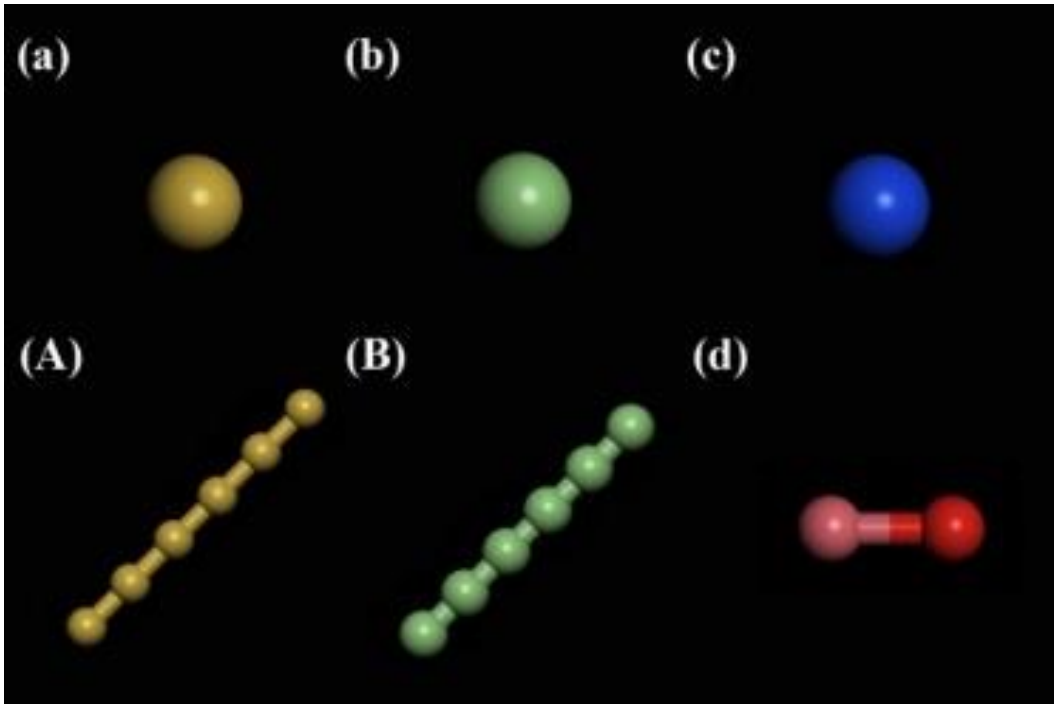

Figure 3.2: Coarse-grained models of **(a)** styrene monomer **(A)** styrene oligomer **(b)** ethylene glycol monomer **(B)** ethylene glycol oligomer **(c)** benzophenone as a photo-initiator **(d)** Sodium dodecyl sulfate as a surfactant in Material Studio 8.0.

3.2.1 DPD Simulation Setup

The size of the simulation cubic cell was set as $100\times100\times100\ \text{Å}^3$ with periodic boundary condition, such that the particle density of each cell is equal to 3 and it contains approximately 22,000 DPD beads with the standard spring constant

equal to 4.0 [139]. To ensure the static equilibrium state, geometry optimization task in Mesocite was performed by smart algorithm in Material Studio 8.0 before any simulations. Mesocite is the simulation module in Material Studio 8.0 for the study of materials at length scales between nanometers and micrometers and time scale in the range of nanoseconds to microseconds [137]. Each simulation consists of 100,000 DPD steps for a total simulation time of 10.0 ns at a constant temperature of 298K. The interaction parameters that are the core of DPD interactions in this study presented in Table 3.3 are derived from Equation 2.20-2.22 in Chapter 2 based on solubility parameters and molar volumes in Table 3.1. In this case, the actual value of molar volume to be used in calculation is the mean molar volume of each pair of beads as it is shown in Table 3.2. By solubility parameter and mean molar volume, then, each Flory-Huggins (χ_{ij}) parameter can be calculated by Equation 2.22 and finally, each interaction parameter can obtained from Equation 2.20.

Table 3.1: Solubility parameters δ and molar volume V of each DPD bead in the simulation [138, 140].

	δ(MPa$^{1/2}$)	V(cm^3/mol)
PEG	32.90	55.8
PS	18.55	106.6
BZP	22.15	164.2
SDST	19.09	160.5
SDSH	41.07	158.5

Table 3.2: V_{ref} of each DPD bead in the simulation.

	PEG	PS	BZP	SDST	SDSH
PEG	55.8				
PS	81.2	106.6			
BZP	110.0	135.4	164.2		
SDST	108.15	133.55	162.35	160.5	
SDSH	107.15	132.55	161.35	159.5	158.5

Table 3.3: Interaction parameter a_{ij} of each DPD bead in the simulation.

	PEG	PS	BZP	SDST	SDSH
PEG	25.00				
PS	47.44	25.00			
BZP	42.06	27.36	25.00		
SDST	52.69	25.05	27.04	25.00	
SDSH	34.6	115.24	102.53	128.44	25.00

3.2.2 UV Ink Compositions

Four different variations of the UV ink composition are considered here to investigate the agglomeration phenomena and effects of each composition on the agglomeration morphology.

1. As the primary composition for comparison, pure oligomers of PEG and PS are combined in three different ratios following Table 3.4 to observe the morphology of agglomeration following the PEG:PS mass ratio of 1:3, 1:1, and 3:1.

Table 3.4: Ink composition for the first simulation case.

PEG : PS	**1:1**	**3:1**	**1:3**
PEG : Oligomer	**50%**	**75%**	**25%**
PS : Oligomer	**50%**	**25%**	**75%**

2. Monomers of PEG and PS are added to the model to observe the effects of monomers on the agglomeration morphology of the system. As it can be seen in Table 3.5, the ratio of oligomers and monomers of each polymer is fixed at 3:1, while the ratios of PEG and PS remain the same as Case 1.

Table 3.5: Ink composition for the second simulation case.

PEG : PS	**1:1**	**3:1**	**1:3**
PEG	**50%**	**75%**	**25%**
- Oligomer	(37.5%)	(56.25%)	(18.75%)
- Monomer	(12.5%)	(18.75%)	(6.25%)
PS	**50%**	**25%**	**75%**
- Oligomer	(37.5%)	(18.75%)	(56.25%)
- Monomer	(12.5%)	(6.25%)	(18.75%)

3. The photo-initiator, BZP, is added to the model following Table 3.6 to better represent actual commercial UV ink and to observe the effects of photo-initiators on agglomeration morphology of the system. The different ratios of PEG and PS oligomers are the same as the previous cases, and the best ratio for minimal agglomeration is determined to perform and compare with the subsequent case of simulation when a surfactant is added to the system.

Table 3.6: Ink composition for the third simulation case.

PEG : PS	**1:1**	**3:1**	**1:3**
PEG	**48%**	**72%**	**24%**
- Oligomer	(36%)	(54%)	(18%)
- Monomer	(12%)	(18%)	(6%)
PS	**48%**	**24%**	**72%**
- Oligomer	(36%)	(18%)	(54%)
- Monomer	(12%)	(6%)	(18%)
BZP	**4%**	**4%**	**4%**

4. In table 3.7, a surfactant additive, sodium dodecyl sulfate (SDS) is added to the system to deal with the problem of nanoscale agglomerations of the polymer nanoparticles and test its effectiveness for de-agglomeration and

stabilization of the system, at the optimal ratio of PEG and PS observed from the earlier cases.

Table 3.7: Ink composition for the fourth simulation case.

PEG : PS	**1:1**	**3:1**	**1:3**
PEG	**46%**	**69%**	**23%**
- Oligomer	(34.5%)	(51.75%)	(17.25%)
- Monomer	(11.5%)	(17.25%)	(5.75%)
PS	**46%**	**23%**	**69%**
- Oligomer	(34.5%)	(17.25%)	(51.75%)
- Monomer	(11.5%)	(5.75%)	(17.25%)
BZP	**4%**	**4%**	**4%**
SDS	**4%**	**4%**	**4%**

3.3 RESULTS & DISCUSSIONS

The results obtained from the simulation cases described in Chapter 3.2 are presented in this chapter to compare and discuss changes in the morphology of agglomeration with different compositions of the UV ink model.

As mentioned in Chapter 3.2, 100,000 DPD steps for a total simulation time of 10.0 ns are enough to bring a system to an equilibrium state, such that simulations can effectively be compared at a constant temperature of 298K. This equilibrated state can be observed from the stable trend in energy and temperature according to the Figure 3.3 and 3.4 respectively as an example for all simulations. It is seen that the system starts to be stabilized around 100 ps, indicating that the equilibrium has been achieved at (or before) 10,000 ps.

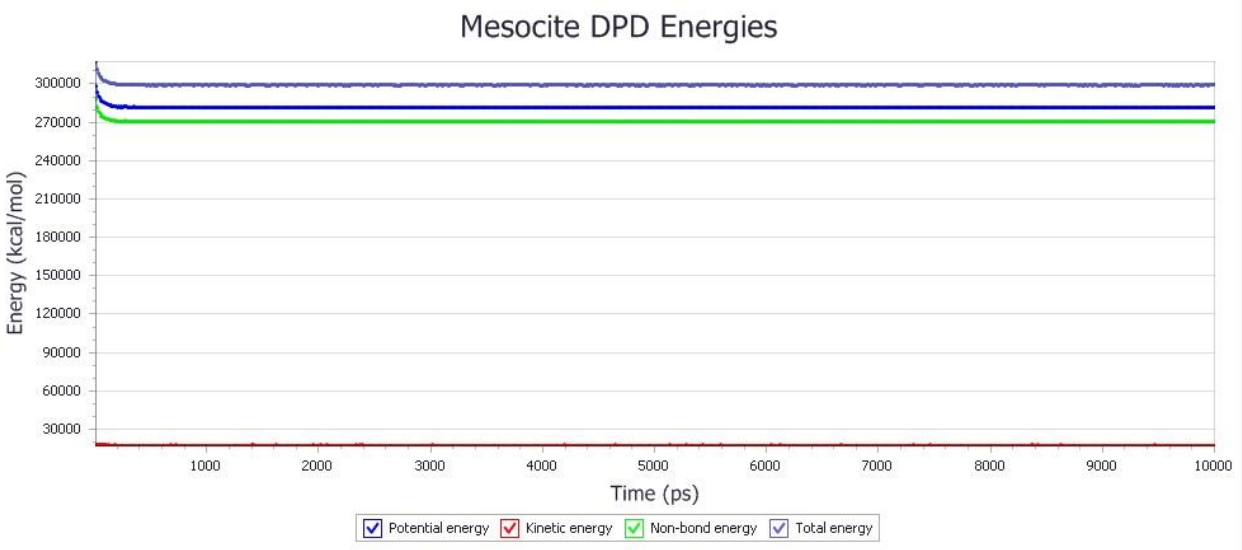

Figure 3.3: An example of energy equilibration curves of a simulation system via Material Studio 8.0 from initial state to an equilibrium state at 10,000 ps. It contains different lines of potential energy (darker blue), kinetic energy (red), non-bond energy (green) and total energy (lighter blue, upper blue).

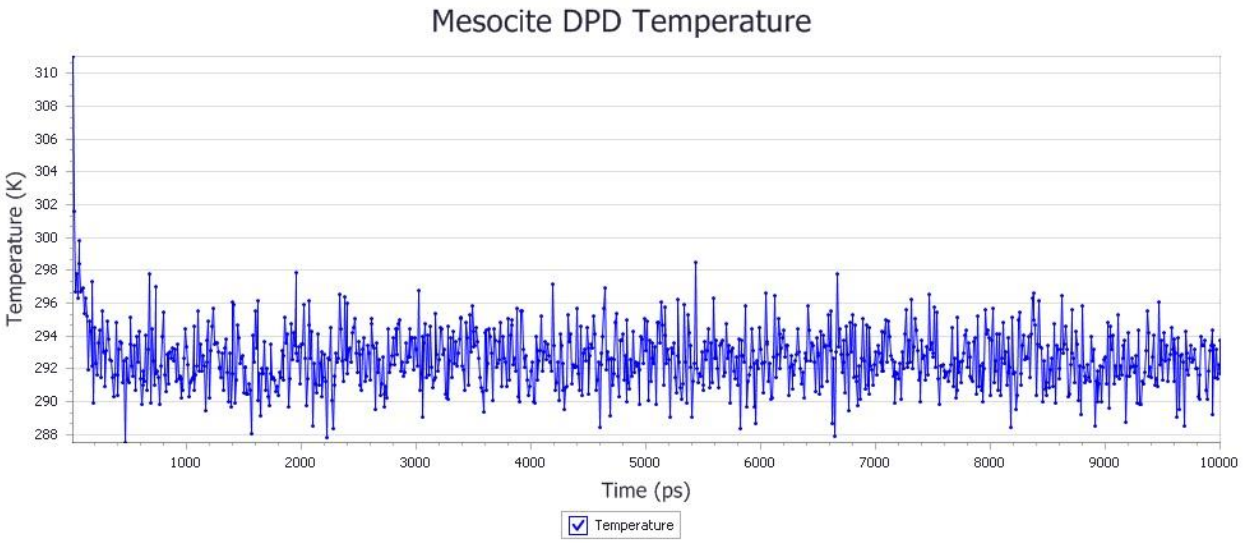

Figure 3.4: An example of temperature equilibrium curve of a simulation system via Material Studio 8.0 from initial state to an equilibrium state at 10,000 ps.

In the first case, only oligomers of PEG and PS are simulated in different ratios. When the equilibrium is reached, the agglomeration morphologies are different depending on the corresponding ratio of PEG and PS. As illustrated in Figure 3.5, the agglomeration morphology of PEG and PS oligomers is dependent on their concentration ratios.

When the concentration ratio of both oligomers is the same, PEG and PS segregate into two phases because of the driving force of the polymer blend to reduce free energy and the different polarity of the two polymers. PEG is a polar molecule while PS is a non-polar molecule, so both polymers mutually separate after forming a bilayer when the separation occurs. This bilayer can be considered to be in the form of lamellae due to the most three common morphologies of polymer blend that are spheres, cylinders, and lamellae [141]. Similar to the model system with 1:1 concentration ratio, the model system with 1:3 ratio also shows

segregation of both PEG and PS but the PEG phase is now in a cylindrical shape and surrounded by the PS phase because of the greater proportion of PS.

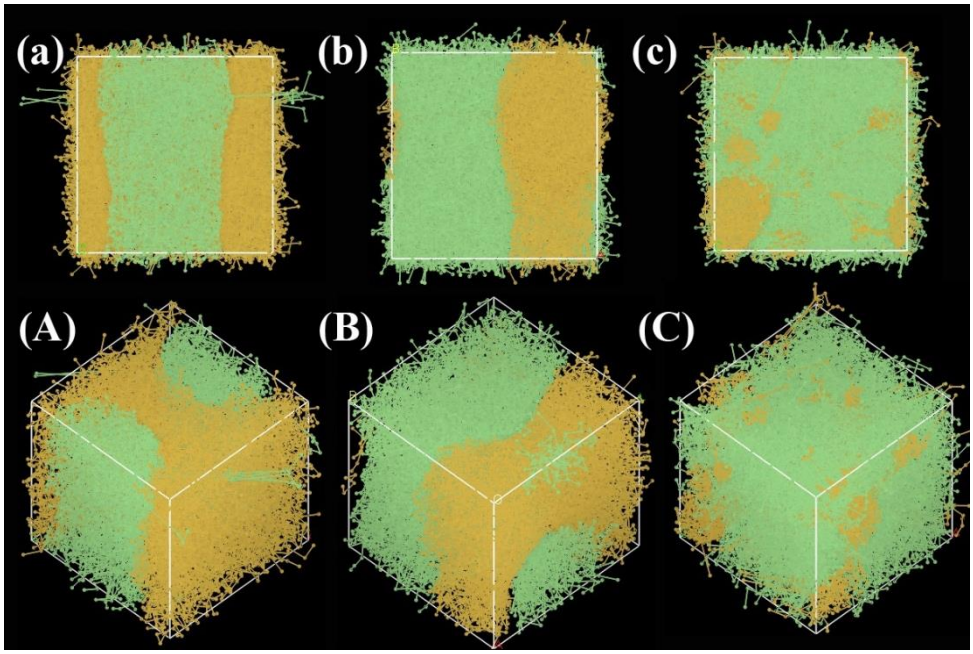

Figure 3.5: The morphology of the simulation models of oligomers of PEG (green) and PS (yellow) in Case 1. **(a)** Front view and **(A)** Isometric view of PEG:PS at ratio 1:3 **(b)** Front view and **(B)** Isometric view of PEG:PS at ratio 1:1 **(c)** Front view and **(C)** Isometric view of PEG:PS at ratio 3:1.

At the 3:1 concentration ratio of PEG and PS respectively, the agglomeration morphology is different from the two previous ratios. The PS phase appears in different sizes of spherical geometry inside the PEG because of stronger surface tension, resulting in boundary shape between liquid-liquid phase separations. In this situation, PS can be considered to be the disperse phase of the system, whereas PEG acts as the dispersion medium. Thus, these results highlight the fact that

relative concentration and polarity of polymers clearly affect the morphology of agglomeration.

In Case 2, where monomers of both PEG and PS are added to the simulation together with their oligomers, morphological changes in the agglomeration show the same trend in comparison with the Case 1 (see Figure 3.6). The 3:1 ratio of PEG and PS retains the same morphology as Case 1c, where PS is finely dispersed in PEG. It is clear that the morphology of PEG and PS agglomeration depends on the concentration ratio of polymers and their polarities. Each ratio of PEG and PS still retains the same morphology characteristics although monomers are added to the system, as shown by the similar morphologies. Thus, it can be deduced that the morphologies of PEG and PS agglomeration are not significantly affected by the presence of PEG and PS monomers.

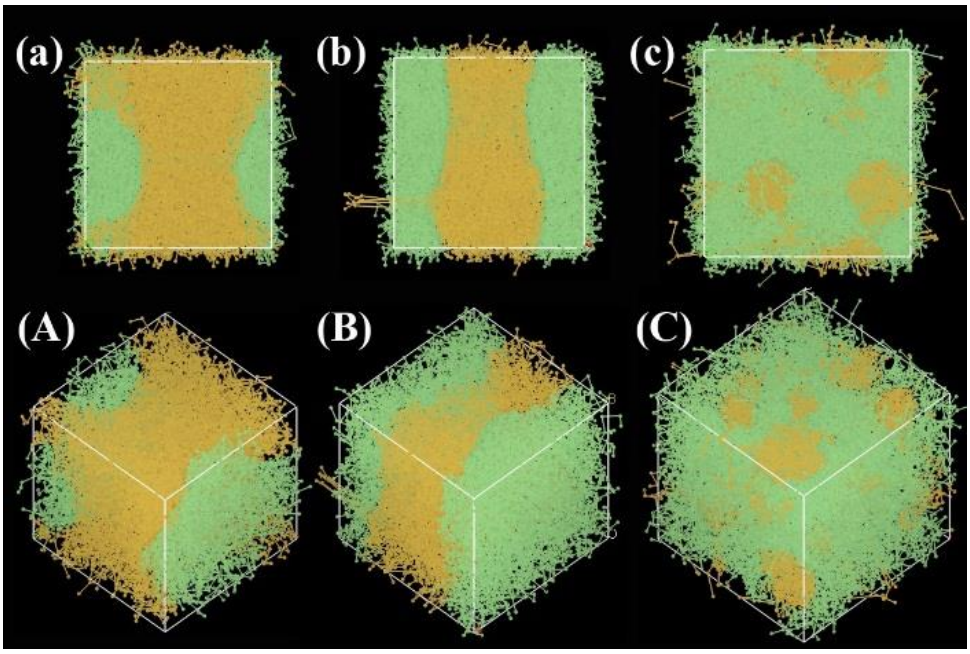

Figure 3.6: The morphology of PEG (green) and PS (yellow) oligomers in Case 2. All monomers of PEG and PS are hidden while oligomers of PEG and PS are present. **(a)** Front view and **(A)** Isometric view of PEG:PS at ratio 1:3 **(b)** Front view and **(B)** Isometric view of PEG:PS at 1:1 **(c)** Front view and **(C)** Isometric view of PEG:PS at ratio 3:1.

From Figure 3.7, the added monomers aggregate with their respective polymers since they have the same electrostatic properties. It can be observed that monomers are in the form of loose agglomerates and they disperse in the same kind of oligomer. The reason behind this phenomenon is the entanglement effect of oligomers, which acts as an effective barrier to prevent agglomeration of the monomers. As oligomers have higher molecular weight, if the length increases, the entanglement among oligomer chains also increases. Thus, monomer beads would need higher amounts of energy to overcome the barrier as a result of oligomer

entanglement [81]. This barrier effect is a by-product that can reduce and prevent monomer agglomeration.

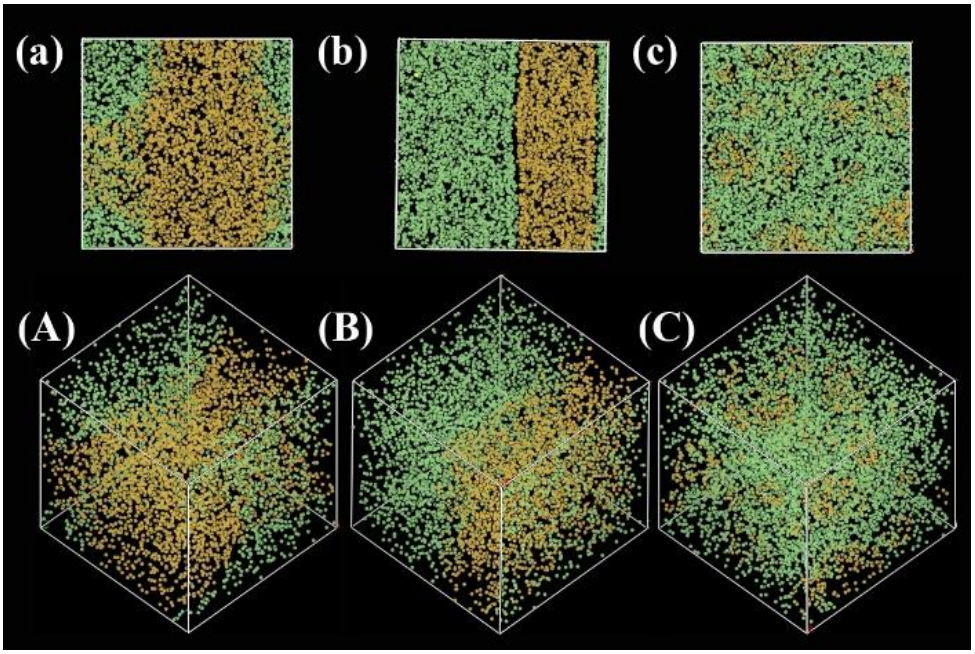

Figure 3.7: The morphology of PEG (green) and PS (yellow) monomers in Case 2. All oligomers of PEG and PS are not shown, only monomers of PEG and PS are presented. **(a)** Front view and **(A)** Isometric view of PEG:PS at ratio1:3 **(b)** Front view and **(B)** Isometric view of PEG:PS at ratio 1:1 **(c)** Front view and **(C)** Isometric view of PEG:PS at ratio 3:1.

To clearly investigate the effect of added monomers on the morphology of oligomers, further comparisons between Figures 3.5 and 3.6 can be made in addition to visual inspection. As it was previously mentioned in Chapter 2.2.2, the radius of gyration (R_g) of agglomerate can be used to investigate the morphology of these results in the aspects of size and compactness [142, 143]. Here, R_g evolution is used to describe this phenomenon by comparison between Case 1 and Case 2 at

the ratio 3:1 of PEG and PS. Added monomers do have a very small effect on the system, resulting in a slight reduction of compactness or relaxation of agglomeration. This can be inferred from Figures 3.8 and 3.9, which shows a slight increase in the average value R_g from 6.8 to 6.9 Å at 10 ns when monomers are present. This shows that the addition of monomers can slightly loosen the agglomerated morphology of oligomers which is the major composition in UV ink as it was mentioned earlier.

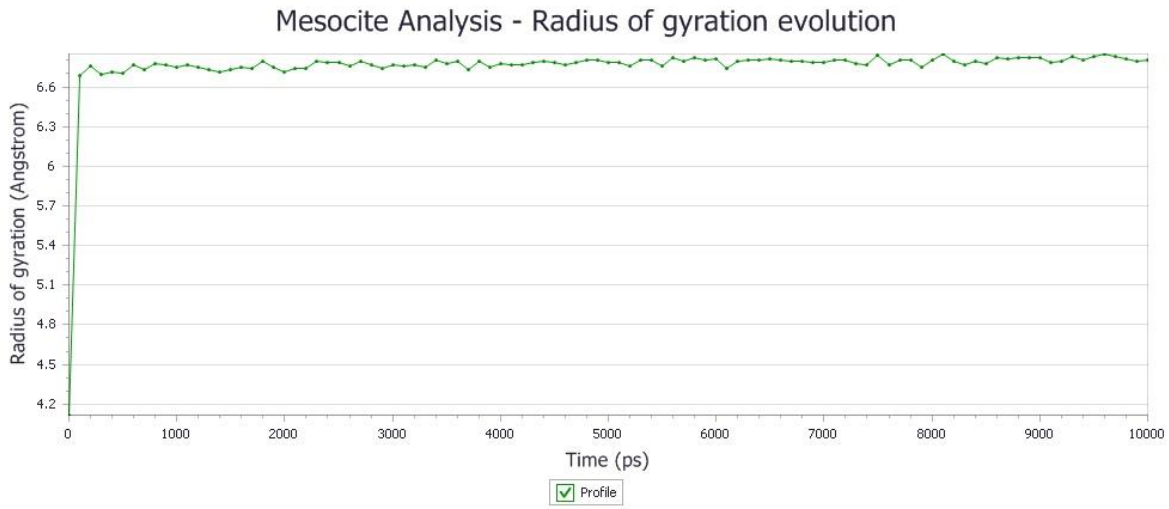

Figure 3.8: Radius of gyration evolution of the UV ink composition from Case 1 (pure oligomers) via Material Studio 8.0 at the ratio 3:1 of PEG: PS.

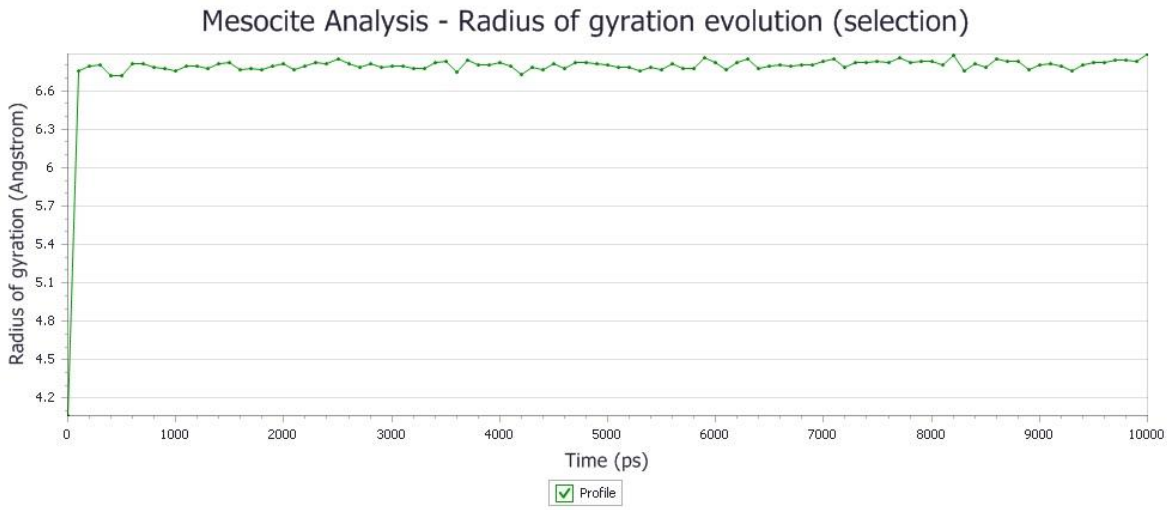

Figure 3.9: Radius of gyration evolution of the UV ink composition from Case 2 (oligomers and monomers) via Material Studio 8.0 at the ratio 3:1 of PEG: PS.

In the third case, the photo-initiator, BZP, is added to obtain a realistic UV ink system. From Figure 3.10 where only the oligomers are visualized, the results show that agglomeration of oligomers occurs in varying shapes according to the ratio of PEG and PS in nearly the same manner as the two previous cases (Figures 3.5 and 3.6). The addition of BZP does not affect the agglomeration morphology of oligomers in the system.

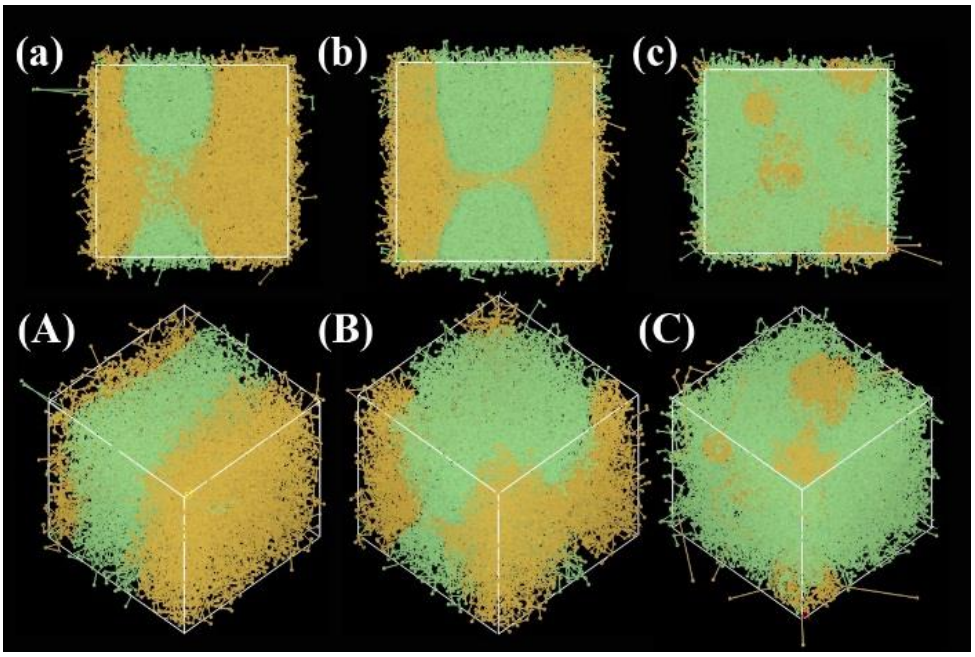

Figure 3.10: The morphology of the simulation models of PEG (green) and PS (yellow) oligomers, as described in Case 3. PEG and PS monomers and BZP are not visualized. **(a)** Front view and **(A)** Isometric view of PEG:PS at ratio 1:3 **(b)** Front view and **(B)** Isometric view of PEG:PS at ratio 1:1 **(c)** Front view and **(C)** Isometric view of PEG:PS at ratio 3:1.

The agglomeration morphology of monomers and photo-initiator is illustrated in Figure 3.11. The results show that BZP agglomerates at the interface between PEG and PS. This is because BZP has intermediate polarity compared to polar PEG and non-polar PS. To explain this phenomenon more in terms of surface tension, BZP exists at the interface of these two homogenous polymer domains because the polymer-polymer interfacial tension, γ_{ES}, is stronger than the absolute value of the different between interfacial tensions of both two particle-polymer regions, γ_{EB} and γ_{SE}, $\gamma_{ES} > |\gamma_{EB} - \gamma_{SE}|$ [144]. When the initiator is located at the

interface, PEG and PS polymerization may be initiated by the separation of BZP into two radicals at the interface.

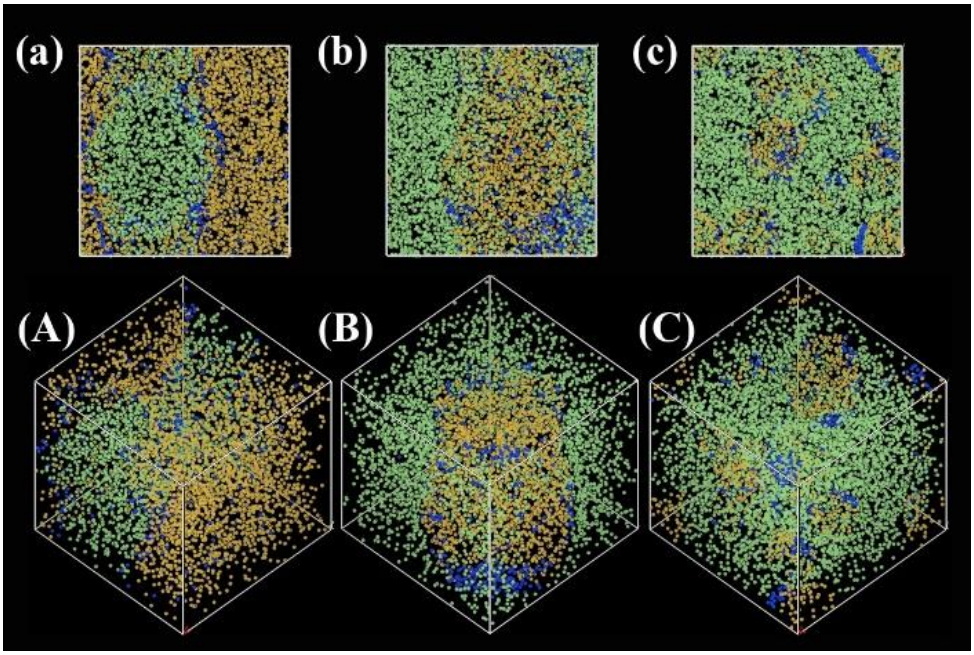

Figure 3.11: The morphology of the simulation models of PEG (green) and PS (yellow) monomers with BZP (blue), as described in Case 3. Oligomers of PEG and PS are not visualized. **(a)** Front view and **(A)** Isometric view of PEG:PS at ratio 1:3 **(b)** Front view and **(B)** Isometric view of PEG:PS at ratio 1:1 **(c)** Front view and **(C)** Isometric view of PEG:PS at ratio 3:1.

From the results of Case 3, when BZP is added as a photo-initiator to mimic commercial UV ink, the concentration ratio of PEG and PS significantly affects agglomeration morphology. At the concentration ratio of 1:3, the BZP forms layers that occur between PEG and PS with broad dispersion and different sizes of agglomerates. When the concentration ratio is 1:1, the results show BZP diffused between PEG and PS to form a shell of BZP region covering the rod of PS. For the

3:1 ratio of PEG to PS, this produced better results in terms of uniform dispersion of BZP agglomerates around the spherical geometry of PS agglomerates, which are dispersed in the PEG phase.

Here, uniformity and dispersion are used to evaluate the UV ink characteristics, and it can be concluded that the 3:1 ratio of PEG to PS can disperse spherical PS within continuous phase of PEG, while BZP appears in the interfacial phase of both polymers. With these characteristics, PS and BZP agglomerates of the 3:1 ratio inside a continuous phase are more uniformly distributed than the layer-like and shell-like shape agglomerates observed in the other ratios, which have lower dispersion uniformity. Apart from visual inspection, the total kinetic energy of the system is also used here as a physical quantitative measure to support this conclusion. It is found that higher amount of PEG results in viscosity reduction and provides higher total kinetic energy, as shown in the presently calculated data in Figure 3.12, where the average total kinetic energy values of ratios 1:3, 1:1, 3:1 of PEG and PS at 10 ns are 17,325, 19,670 and 21,970 kcal/mol, respectively. Higher kinetic energy reduces the probability of agglomeration, thus the 3:1 ratio provides the best condition for dispersion uniformity with the potential for improved rheological properties [145].

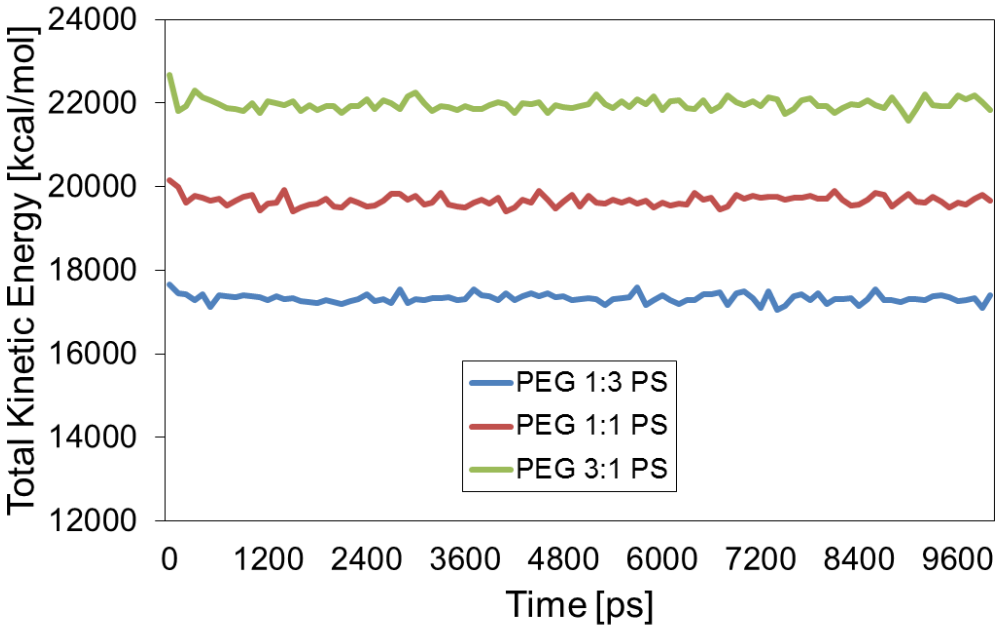

Figure 3.12: Total kinetic energy of three different ratios of polymeric UV ink from Case 3 are compared to investigate the trend of agglomeration.

Thus far, the simulation results have indicated that the aggregation morphologies of UV ink can be influenced by their composition, as well as other additives. In the next set of simulations, the surfactant SDS is added to determine its efficacy in preventing, reducing, and controlling agglomeration. The ratio of PEG to PS used is 3:1.

From Figures 3.13 and 3.14, the size of PS oligomer spherical agglomerates is observed to become slightly smaller when SDS is added. However, it is not sufficiently obvious visually to provide a comparison in terms of distribution and size of agglomerates, thus it is necessary to extract better representations and calculate physical parameters from the simulations. According to the theory of

dynamics of surfactants at interfaces [146, 147], surfactants are expected to be a chemical method of de-agglomeration to stabilize the UV ink model. Surfactants can form micelle-like aggregates where polar molecules or hydrophilic parts of surfactants associate with the medium phase, while non-polar molecules will face the interior of the aggregate. Micelle-like aggregates of SDS (Figures 3.15b, 3.15B and 3.16) can act like a shell to control the size of agglomerates by protecting each agglomerate from further agglomeration, and promote dispersion by repulsing other agglomerates.

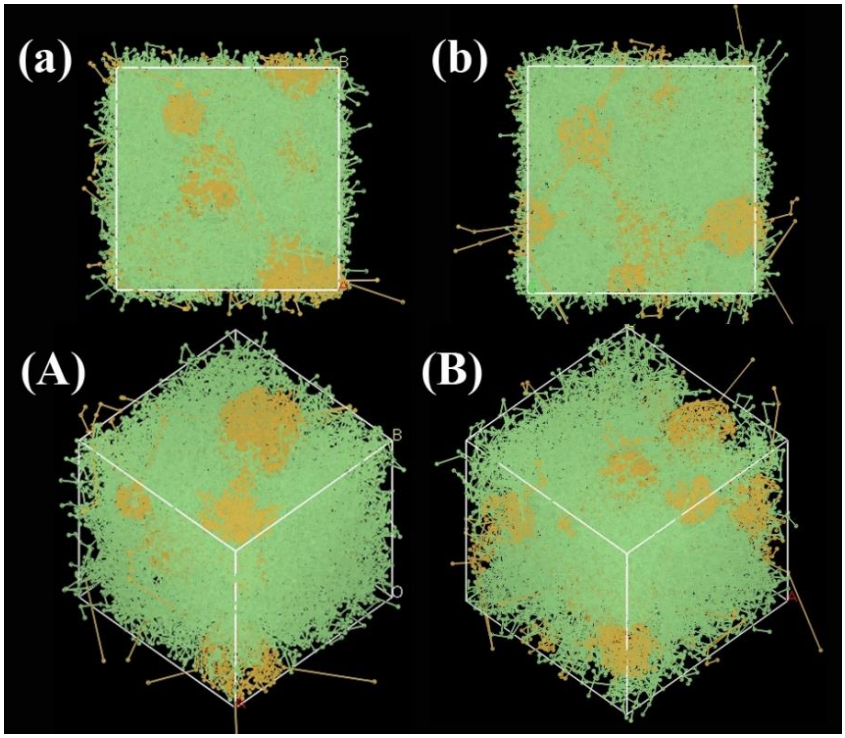

Figure 3.13: The morphology of PEG (green) and PS (yellow) oligomers at the ratio of 3:1. **(a)** Front view and **(A)** Isometric view without the inclusion of surfactants from Case 3. **(b)** Front view and **(B)** Isometric view of with the inclusion of SDS (not shown) from Case 4

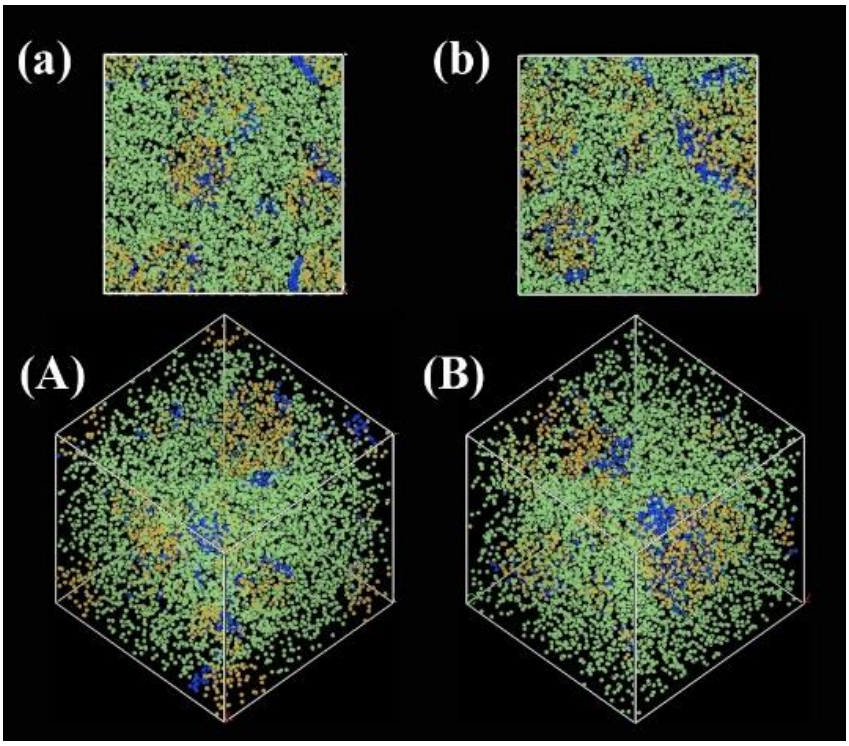

Figure 3.14: The morphology of PEG (green) and PS (yellow) monomers and BZP (blue) at the ratio of 3:1. **(a)** Front view and **(A)** Isometric view without the inclusion of surfactants from Case 3. **(b)** Front view and **(B)** Isometric view of with the inclusion of SDS (not shown) from Case 4.

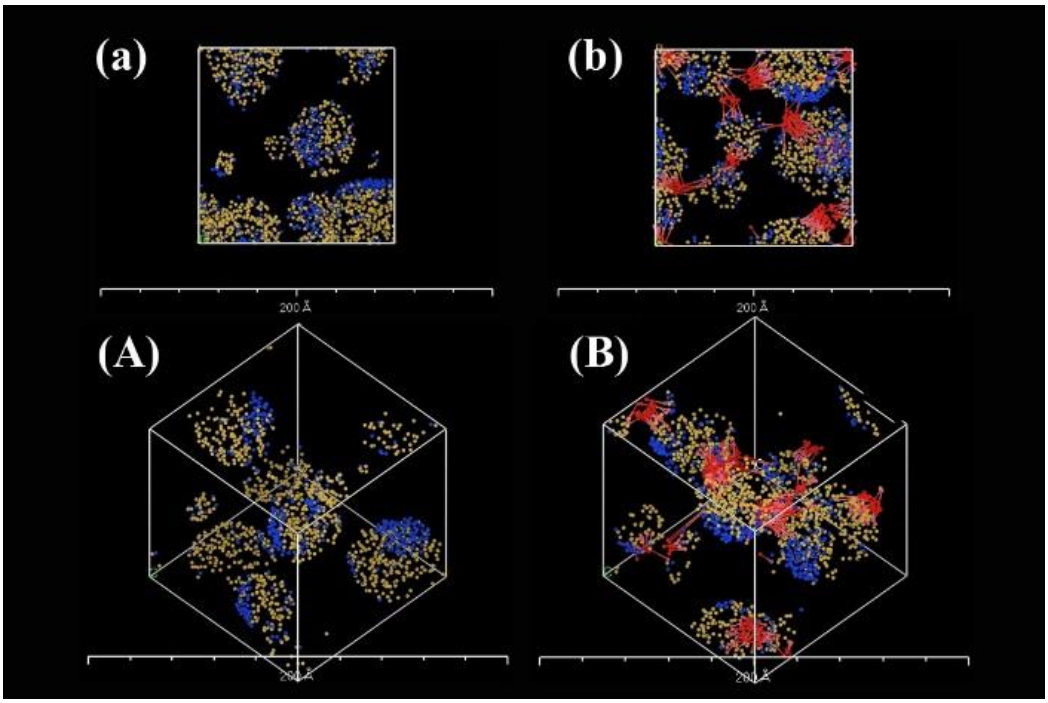

Figure 3.15: The morphology of the simulation models of PEG:PS at ratio 3:1. Here, the PS (yellow), photo-initiator (blue) and SDS (red) are visible. **(a)** Front view and **(A)** Isometric view of the case without surfactants from Case 3. **(b)** Front view and **(B)** Isometric view of the case with SDS as a surfactant from Case 4, and in the scale bar of 200Å.

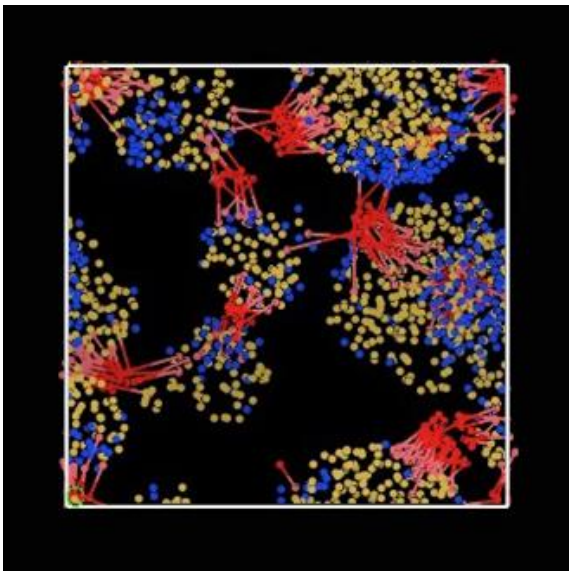

Figure 3.16: The morphology of the simulation models of PEG:PS at ratio 3:1 where PS (yellow), photo-initiator (blue) and SDS (red) are visible.

To explain the effect of SDS on the dispersion of agglomerates, more quantitative physical measurements are required to better assess its effectiveness. From both curves in Figure 3.17, we observe that the R_g evolution of agglomerates in a simulation cell of Case 4 is higher than in Case 3 for the selected ratio 3:1, with respective average values of 7.2 Å and 7.6Å at 10ns. Thus, the reduction in compactness increases the dispersion of agglomerates and reduces interaction among agglomerates. For the average size of the agglomerates, each individual agglomerate's R_g evolution is observed and used to calculate the average value. Highly uniform dispersion is found in the presence of SDS because it is found that the average size of the agglomerates is reduced from 520 Å to 440 Å and the number of clusters is doubled, from 7 to 14, by the introduction of SDS (see Figure 3.18). Due to the improvement in the dispersion, the number of smaller

agglomerates in the distribution naturally becomes higher, resulting in better dispersion uniformity.

Moreover, agglomerates in Case 4 are denser because the SDS between each agglomerate tend to take on micelle-like formations, and these act like a fender between each agglomerate. Although they are not in the form of complete micelles due to the low quantity, they can still form barriers to prevent further agglomeration. To fully investigate the effects of the SDS surfactant in a nano-inkjet printing scenario, it would be necessary to perform the dynamic simulation of the nano-droplet evolution and formation through a nano-nozzle. This is carried out in the next phase of the project, with the aim of optimizing process parameters, and devising de-agglomeration methods through physical and chemical means, to achieve the best print quality.

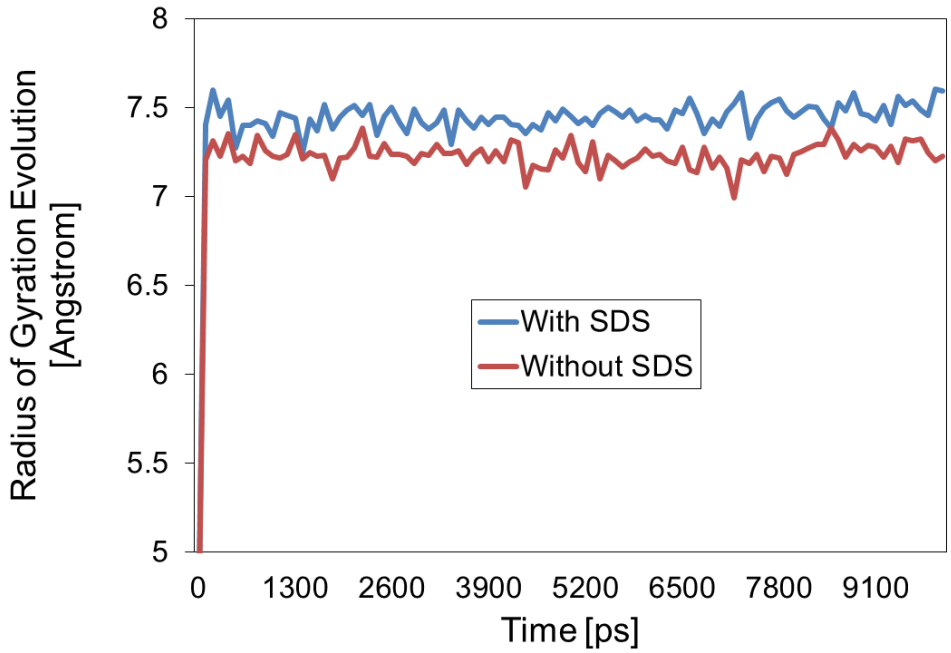

Figure 3.17: Radius of gyration evolution of Case 3 (without SDS) and Case 4 (with SDS) at the PEG:PS ratio 3:1.

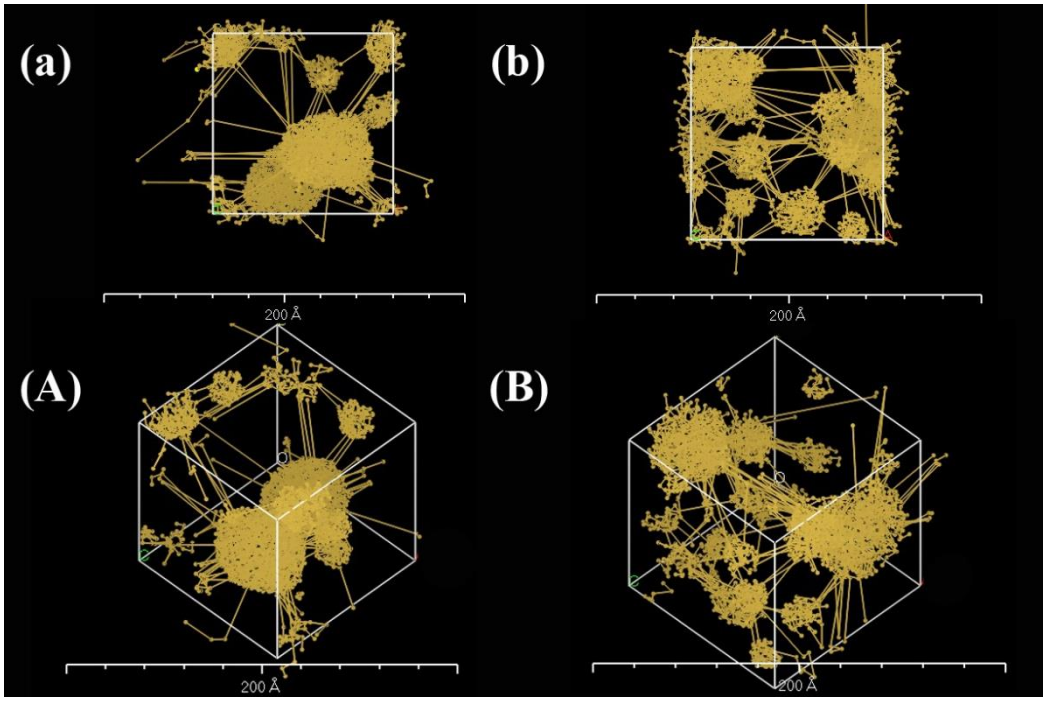

Figure 3.18: The morphology of PS (yellow) oligomer at the ratio of 3:1. **(a)** Front view and **(A)** Isometric view without the inclusion of surfactants from Case 3. **(b)** Front view and **(B)** Isometric view of with the inclusion of SDS (not shown) from Case 4.

3.4 CONCLUSIONS

The present simulation results provide a better understanding of the characteristics of an UV ink fluid composing of PEG and PS as the main polymeric components. These oligomers dominate the agglomeration morphology. Added monomers of PEG and PS appear in the same phase with their respective oligomers because they possess the same polarity, but they are loosely agglomerated. This is due to the entanglement effect of oligomers which acts like a barrier to prevent agglomeration. The addition of monomers can slightly reduce the agglomeration of the oligomers. From three different ratios of PEG to PS, it is found that the ratio of 3:1 provides the best result in terms of uniformity, size of agglomeration, and dispersion. PS agglomerates spherically as the disperse phase within the medium phase of PEG. Agglomerates in other ratios segregates into two distinct phases with lower uniformity and dispersion. Addition of the photo-initiator, BZP, results in BZP aggregating at the interface of both polymers. BZP is slightly polar so they tend to bind to the interfaces between polar PEG and non-polar PS. With the 3:1 ratio of PEG to PS, BZP agglomerates disperse around the spherical PS agglomerate. Insights into the underlying chemistry have also been gained in this study when BZP as a photo-initiator, and SDS as an additive, were added to the ink composition. In particular, we established that SDS as a surfactant, played an important role in reducing agglomeration.

Higher amounts of PEG can promote the quality of UV ink in terms of the ink's viscosity. This is advantageous for nano-droplet formation in 3D nano-inkjet printing as the nozzle is very small and the printing fluid needs to maintain low

viscosity to flow properly. The ink can be enhanced further by mixing SDS. Our results show that SDS can better disperse agglomerates and reduce the average size of agglomerates with better distributions of the higher number of agglomerates. But it is denser and the size can be controlled because the SDS around the surface of each agglomerate tends to form micelles. This micelle formation can create a barrier for further agglomeration. To obviously investigate effects of the surfactant, it can be done again in the optimization of all physical conditions of de-agglomeration in part of the dynamic simulation of nano-droplet formation.

This is the first study to simulate and investigate the agglomeration characteristics in the context of UV ink fluid compositions and we believe this study provides the impetus for further research into the use of other additives to prevent, reduce and control various forms of agglomeration. Progress in these endeavors is essential for very small-scale high-resolution 3D inkjet printing, as good stability of the printing fluid is necessary to avoid the clogging in the nano-nozzle head, and to achieve good print quality. This study also validates the efficacy of the mesoscale DPD methodology for the modeling and analysis of nanoscale UV ink agglomeration. The major challenges of agglomeration of printing fluids at these small scales are currently far from being well understood, and much more theoretical and experimental studies remains to be done.

CHAPTER 4 MANY-BODY DISSIPATIVE PARTICLE DYNAMICS SIMULATIONS OF NANO-DROPLET FORMATION IN 3D NANO-INKJET PRINTING

In this chapter, nano-droplet formation in polymeric ink systems for 3D inkjet printing is characterized with many-body dissipative particle dynamics (MDPD) simulation technique. Compared to conventional DPD, MDPD is a simulation method developed recently in 2001 that is focused on vapor-liquid coexistence instead of specific liquid-liquid interactions. This allows nano-droplet formation to be numerically studied. In this thesis work, the ink-nozzle system and their interaction behavior are modelled in MDPD in order to determine the conditions that are necessary and optimal for nano-droplet formation using commercial 3D inkjet ink.

4.1 INTRODUCTION

As seen in Chapter 3, DPD can be effectively used to study interesting phenomenon, like agglomeration, within the polymeric ink. However, the limitation in DPD simulation is that it includes only purely repulsive forces, making it ineffective for problems related to free-surface fluid dynamics. The gas-liquid interface present in nano-droplet formation process is one such problem. Thus, DPD needs to be extended to allow the study of nano-droplet formation. One such extension, named as MDPD, was introduced in Chapter 2.5, and is used here to study the process of nano-droplet formation in 3D nano-inkjet printing.

The MDPD simulations in this study were carried out via LAMMPS [148]. The coarse-grained models are generated by directly coarse-graining from the atomistic model, similar to the DPD simulations discussed in Chapter 3. The difference is that in MDPD, there is an additional tunable solid-liquid attraction parameter, A_{sl}, which can be adjusted to capture the hydrodynamics behavior of droplet formation. The MDPD simulation set-up, coarse-graining and parameters tuning process are further elaborated in Section 4.2.

To validate the MDPD model constructed for this study, a comparison is made with a reference study, which reported experimental and theoretical results of droplet formation with 10 and 30 microns diameter nozzle [139]. This microscale study was chosen due to the lack of experimental data for nanoscale droplet formation. In this case, water, instead of ink, is used as the printing fluid to match the reference and validate the MDPD simulation model. Due to the need to scale up our simulation results to micron level for comparison with experimental results, the

coarse graining factor is inevitably large. The large coarse graining factor results in unrealistically low physical quantities like pressure and velocity from our simulation results. To work-around this, we came up with a conversion methodology to adjust the size of physical quantities from our simulations to be comparable with realistic experimental data. This artificial procedure can be utilized to relate DPD and MDPD simulation model to macro-scale scenarios at very low computational cost. Finally, the validated MDPD model is used to investigate trends of important physical quantities in nano-droplet formation in 3D nano-inkjet printing. The validation of our MDPD model, conversion methodology and final characterization of the nano-droplet formation process are collectively detailed in Section 4.3.

4.2 RESEARCH METHODOLOGY

With reference to the MDPD theory described in Chapter 2.5, this section will explain the simulation methods and procedures for studying nano-droplet formation in 3D nano-inkjet printing. The MDPD simulation setup is first presented, which includes the construction of the nozzle-ink model and the determination and validation of all required physical and interaction parameters for MDPD. Next, the method used to determine the coarse-graining level and bond equilibrium distance for the UV ink beads are discussed. The detailed parameterization of suitable solid-liquid attraction parameter, A_{sl}, for the MDPD simulations of nano-droplet formation is then further elaborated. Finally, the procedures of the MDPD simulations run is detailed.

4.2.1 Simulation Setup

The MDPD simulations in this study was carried out via LAMMPS [148]. The size of the simulation box is set as 60×60×300 r_c with non-periodic boundary conditions, such that number density is equal to 6 following the standard particle density of MDPD beads [122, 123, 125]. The model composed of two main parts: the nozzle and the polymeric ink. The nozzle has a cylindrical body and a conical tip, where the inner and outer radius are $7r_c$ and $10r_c$ respectively. The cone of the nozzle has a slope of 30° and the orifice size is r_c in radius. The angle, 30°, is chosen because of the consideration based on an optimization of nano-droplet formation. This cone angle is equivalent to 120° of lead angle which gives lower

discharge coefficient with better opportunity of nano-droplet formation [149]. Although the angle needs larger size of driving pressure in order to generate the droplet formation, it can reduce droplet breakup time and increase nano-droplet velocity that is an important to consider in very small scale printing [150]. The ink contains 16,000 MDPD beads of 1,000 MDPD monomers and 2,500 oligomers [126]. The ratio of monomers to oligomers is arbitrarily set such that oligomer made up the majority of ink composition (as mentioned in Chapter 2.1), in a 2.5 to 1 ratio. The geometry of the nozzle in this simulation is shown in Table 4.1 and illustrated in Figure 4.1. The actual simulation setup in LAMMPS is presented in Figure 4.2. In the equilibration phase, the ink beads are equilibrized in the cylindrical part of the nozzle, as shown in Figure 4.2A. The orifice is then cut after equilibration to allow the ink to flow out of the nozzle, forming nano-droplets, as depicted in Figure 4.2B. PACKMOL [151] was first used to generate initial point for the ink system in this study with the guarantee of no short range repulsive interactions' disruption, and then the rest of setup was done by LAMMPS, as described later in Section 4.2.5.

Table 4.1: A summary of the nozzle's geometry.

length	$27r_c$
outer radius	$10r_c$
inner radius	$7r_c$
angle of cone	30 °
orifice radius	r_c

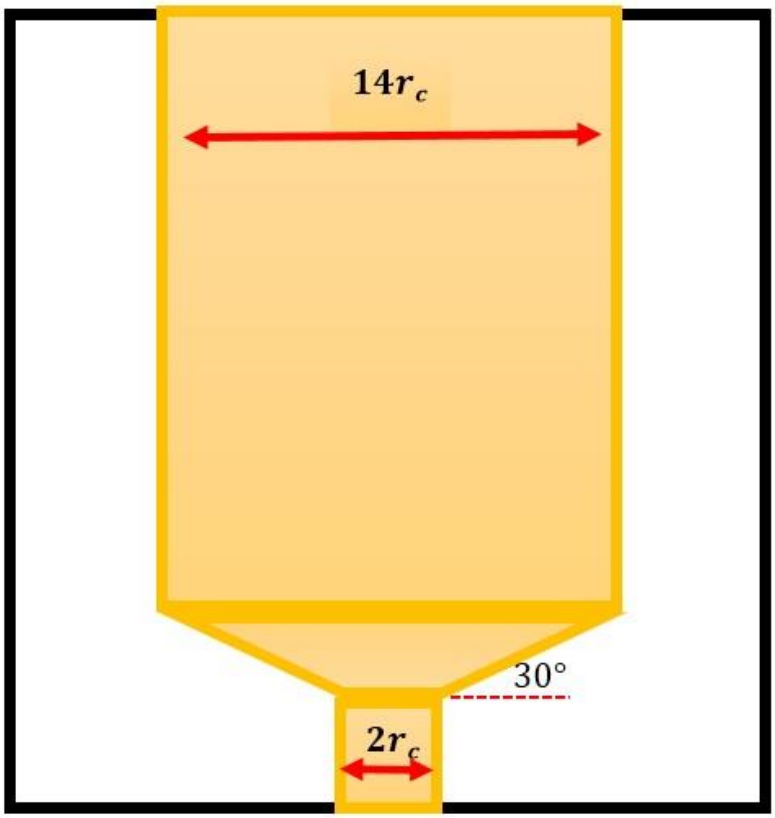

Figure 4.1: The geometry of the nozzle.

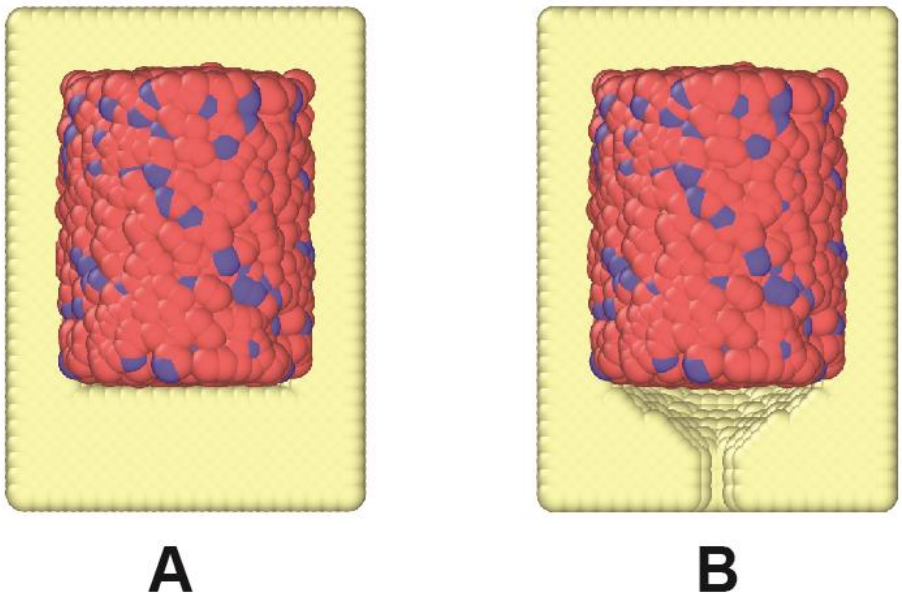

Figure 4.2: Actual simulation setup in LAMMPS. **(A)** The equilibration step when the nozzle is not cut **(B)** The simulation run when the nozzle is cut.

As described in Chapter 2, the typical values for MDPD parameters r_c (1), $r_d(0.75)$, $A_{ll}(-40), B_{ij}(25), \gamma(50)$ and $\sigma(10)$ are adopted in this simulation study [122]. For convenience and to make the simulations generally applicable, the reduced (dimensionless) units system is adopted. In the reduced units system, four fundamental quantities (r_c, N_m, T, and ε) are set to 1 so that all quantities are unitless. To convert quantities to real units, distances, masses and energy are multiples of the fundamental quantities specified, and the other quantities of interest have to be multiplied by the conversion relationship as shown in Table 4.2. All MDPD simulation parameters in this study is summarized in Table 4.3.

Table 4.2: The fundamental representations of physical quantities in the term reduced units [65].

Physical Quantity	Unit
Length	r_C
Energy	$\varepsilon = k_b T$
Mass	$m = N_m M_w$
Time	$r_C(m/\varepsilon)^{1/2}$
Velocity	$(\varepsilon/m)^{1/2}$
Force	ε/r_C
Pressure	$\varepsilon/{r_C}^3$
Temperature	ε/k_B

Table 4.3: A summary of MDPD simulation parameters in reduced units.

liquid density	ρ	6.0
repulsive force range	r_d	0.75
cut-off radius	r_c	1.0
liquid-liquid attraction	A_{ll}	-40
liquid-liquid repulsion	B_{ll}	25
solid-liquid attraction	A_{sl}	To be tuned (See section 4.2.4)
solid-liquid repulsion	B_{sl}	25
solid-solid attraction	A_{ss}	-40
solid-solid repulsion	B_{ss}	25
coefficient for dissipative force	γ	50.0
coefficient for random force	σ	10.0
time step	Δt	0.01

4.2.2 Determination of Coarse-graining Level

Although there are no well-defined parameters to model specific types of polymers in MDPD, the molar volume of propylene and water can be used to determine the coarse-graining level in this MDPD simulation [67]. In order to attain the relevant length scale of the phenomenon to be examined, which is given by r_c in physical units, the coarse-graining level N_m is the first important parameter to consider for generating each size of nozzles in this MDPD simulation. This

coarse-graining level can be determined in a manner similar to a work of Groot and Rabone [67],

$$r_c = \sqrt[3]{\rho V_m N_m} \qquad \textit{Equation 4.38}$$

where r_c is the cut-off radius due to the coarse-graining level; N_m the number of molecules per bead or coarse graining level; ρ the number density; and V_m the molar volume.

Thus, by Equation 4.38, the coarse-graining level or the number of molecules per bead N_m for each simulation can be determined from the physical radius of the nozzle orifice, which was set to be equal to r_c (see Section 4.2.1). As an illustration, the coarse-graining level N_m of polymeric ink for nano-nozzles of different orifice diameter is listed in Table 4.4. In particular, to validate against the reference experimental results for orifice diameter of 10 and 30 microns, the coarse-graining level is shown in Table 4.5. As can be observed, the coarse graining level is extremely large in this case. This will lead to unphysical low values for quantities like pressure and velocity, and is further elaborated in Section 4.3.1.

Table 4.4: The coarse-graining level of polymeric ink scales according to the size of the orifices in terms of real units.

Diameter of orifice (nm)	Coarse-graining level (N_m)
10	264.69
50	33,085.22
100	264,686.90
500	33,085,925.00
1,000	264,686,898.10

Table 4.5: The coarse-graining level of water scales according to the size of the orifices, 10 and 30 microns, in order to compare with the reference [139].

Diameter of orifice (nm)	Coarse-graining level (N_m)
10,000	418,204,958,592.00
30,000	11,291,514,296,488.90

4.2.3 Bond Equilibrium Distance

Because the oligomers are modeled as a chain of connected beads of monomers as mentioned since Chapter 2, it is necessary to add a bond potential to model bond interactions of oligomers. In this case, the type of bond potential

normally used in DPD and MDPD simulation methods is harmonic bond [123, 126, 152] (see Equation 4.39) with the harmonic bond force constant set to 64 [126],

$$U_H = \frac{1}{2} k_h (r - r_0)^2 \qquad \textbf{\textit{Equation 4.39}}$$

where U_H is bond potential; k_h the harmonic bond force constant; and r_0 the bond equilibrium distance.

LAMMPS is used to investigate the bond equilibrium distance. In this study, the range of the repulsive force and the attractive force limit are set to be 0.75 and 1.0 of r_c , respectively. The bond equilibrium distance is determined from the radial distribution function. Because the position of the first peak can be used to estimate the mean distance between the central atom. In this case, the mean distance of nearest neighbour is distance between connected beads so the mean distance is the equilibrium bond distance [153]. From Figure 4.3, it is found that the first peak of the function occurs at 0.685 of r_c that is exactly the same value as it was studied in a MDPD's previous work [154]. Thus, bond equilibrium distance of oligomer in this study is 0.685 of r_c.

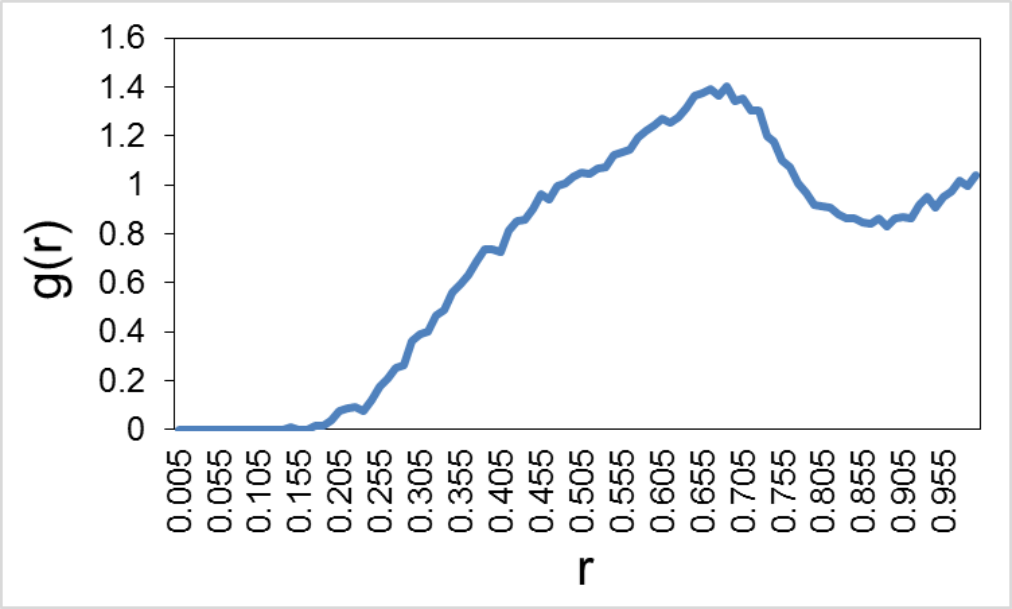

Figure 4.3: The peak of radial distribution function of MDPD oligomer following to the standard MDPD parameters.

4.2.4 MDPD Parameterization

As listed in Table 4.2, all the repulsions in this study (liquid-liquid (B_{ll}), solid-liquid (B_{sl}) and solid-solid (B_{ss}) repulsions) are set to be 25 and the liquid-liquid (A_{ll}) and solid-solid (A_{ss}) attraction is -40. The solid-liquid attraction, A_{sl}, which is the interaction between the liquid ink and wall of the nozzle, is varied and tuned in this study for reasonable results. It has been shown in previous studies that A_{sl} can be tuned to achieve the desired behavior between the ink and the nozzle's wall [123, 155]. In this study, the optimization of A_{sl} is considered based on three different physical parameters of the ink system: kinetic energy, potential energy and radius of gyration.

A_{sl} is varied from 0 to -40 to examine the trends of kinetic energy, potential energy and radius of gyration during droplet formation in 10 and 30 micron

nozzles. In Figure 4.4, the trend of kinetic energy with time in reduced units for a range of A_{sl} from 0 to -40 is presented. It can be seen that at $A_{sl} = -30$, the kinetic energy is relatively low and stable on average. Since kinetic energy can be used to measure probability of agglomeration [145], this implies good stability in agglomeration characteristics and relatively low amount of agglomeration at this value of A_{sl}. The stabilization of the kinetic energy after equilibration (after timestep 4000) also confirms the stability of the system.

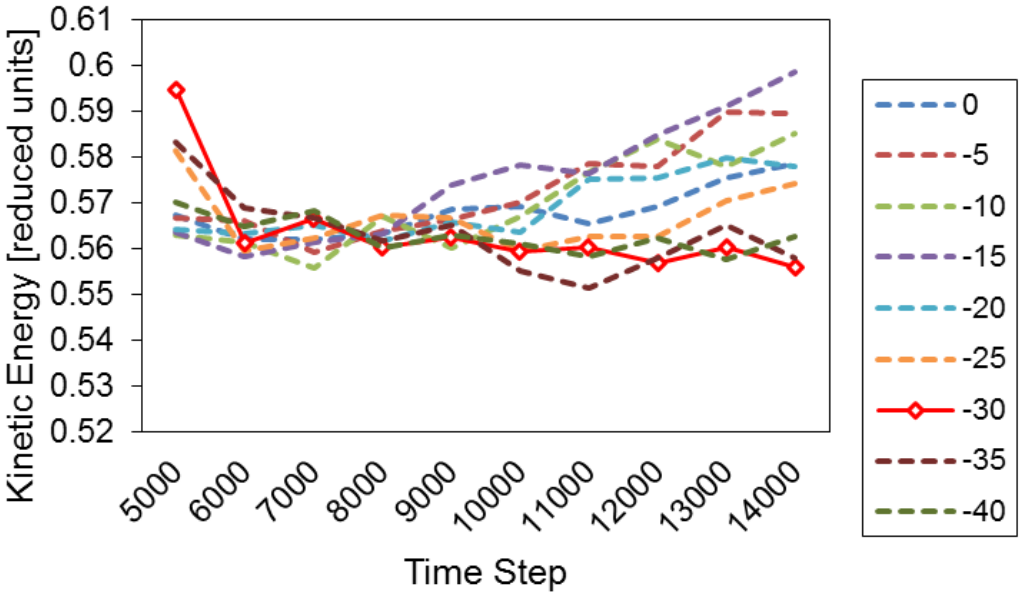

Figure 4.4: The kinetic energy of polymeric ink from different values of solid-liquid attraction.

Next, Figure 4.5 shows the trend of potential energy with time for the range of values considered. It can be seen that at A_{sl} = -30, the potential energy of the system is intermediate when compared with other values of A_{sl}. Potential energy represents non-bonded potential and bonded potential between beads in the ink

system [156]. Thus, this intermediate value represents a balance point of bonded and non-bonded interactions within the ink itself. Thus, this potential energy investigation guides that this intermediate value of system's potential energy is desirable.

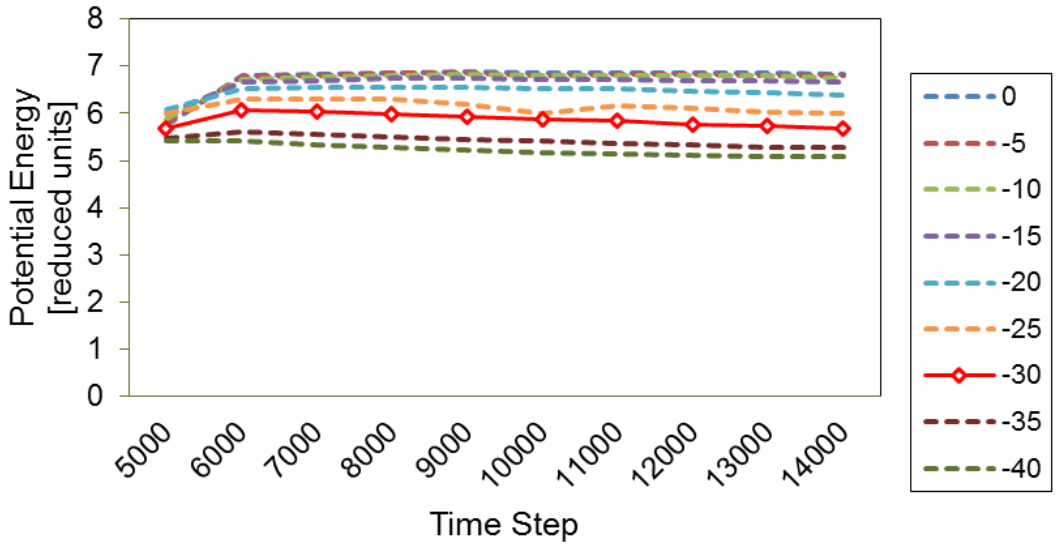

Figure 4.5: The potential energy of polymeric ink from different values of solid-liquid attraction.

Finally, it can be seen from the trends of radius of gyration that at $A_{sl} = -30$, there is a good distribution of the polymeric ink molecules when compared with other values of A_{sl} (see Figure 4.6). Larger values of A_{sl} closer to 0 leads to unstable values of radius of gyration, which indicates that the interaction between polymeric ink is not strong enough to balance interaction amongst them and hold the ink at stable densities, resulting in increasing values of the radius of gyration. For A_{sl} value lower than -30, the resulting radius of gyration is too close to the

standard attraction (A_{ss}, A_{ll}) between the same phase, i.e. -40. This is not reasonable, since we expect the radius of gyration between two phases (solid-liquid) to be different than liquid-liquid or solid-solid interactions. As can be observed, there is also a good agreement between the A_{sl} value of -30 and the common range of partly wetting fluid in MDPD previously mentioned in Chapter 2.5 that is -32.5 to -25 [123].

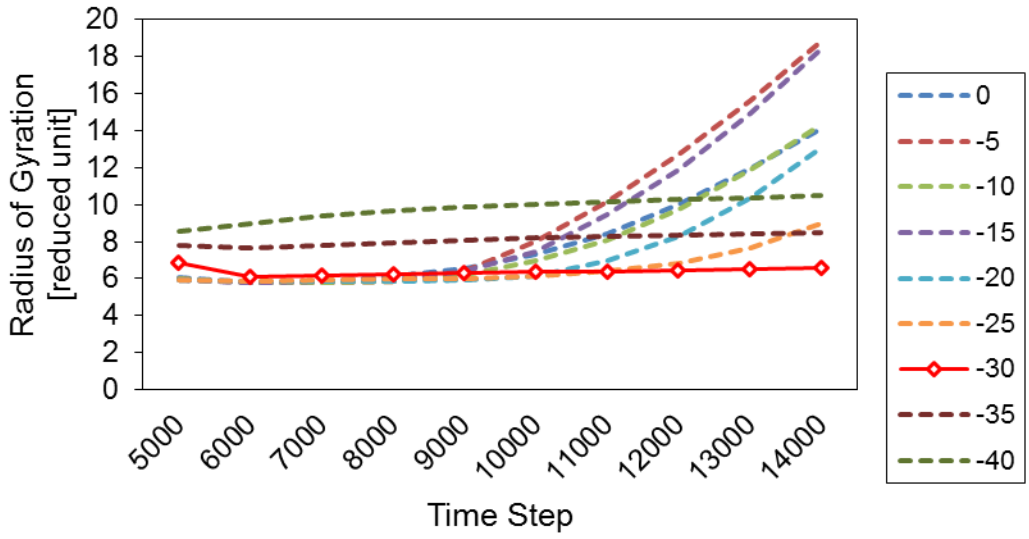

Figure 4.6: The radius of gyration of polymeric ink from different values of solid-liquid attraction.

In addition to the 3 studies conducted, a comparison to physical experimental result from the reference study [139] based on micro-droplet formation in 10 and 30 micron nozzles also gives the same agreement. In Figure 4.7, MDPD simulation results 3 points of attraction values which provide precisely prediction in the experiment. According to theoretical consideration that the suitable attraction must be between -40 (maximum attraction) to -25 (minimum attraction), the solid-liquid attraction value, A_{sl}, of -30 between nozzle and ink gives an acceptable consistency for both 10 and 30 micron nozzles. Thus, these studies strongly support $A_{sl} = -30$ as the optimal value of solid-liquid attraction chosen to be used in this study.

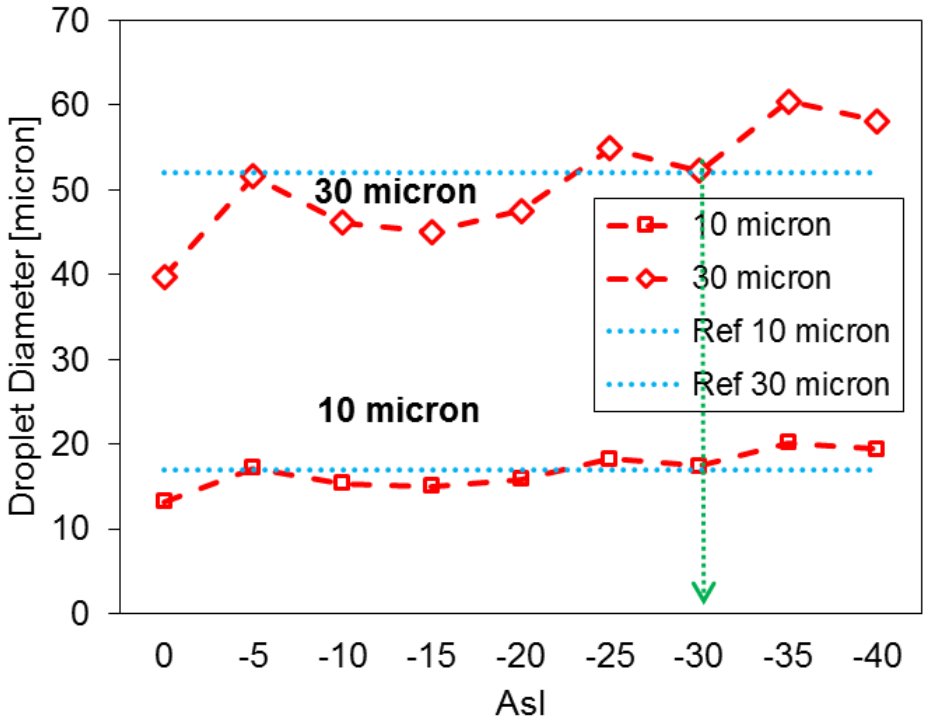

Figure 4.7: Changes in the water droplet diameter with different values of solid-liquid attraction in both the 10 and 30 microns nozzles and comparison to the average value from the reference.

4.2.5 MDPD Simulation Run

After the simulation setup was done in accordance to Figure 4.2 and all the necessary parameters are assigned, the system was equilibrated for 4,000 timesteps. Next, the internal part of nozzle was cut following Figure 4.2 (B). Every ink bead was then subjected to a gravitational body force so that it will be move downwards through the nozzle. This approach is similar to the MDPD study on pendent droplet by Warren in 2003 [122]. The difference here is that the body force in this study was set to work in more realistic way such that the effect of force is cut off after the pinching of the droplet.

In this study, two key parameters were identified thorough investigation on their effects on nano-droplet formation: effective pressure and temperature. In this case, effective pressure is the pressure at the nozzle's end and it can be calculated by the result of the total body force exerted on each individual bead in the whole ink system divided by the surface area of the nozzle's end. The body force is applied under the condition that each bead is still included the ink system in order to imitate what happens in reality that there is no force exerted on it after droplet formation. To investigate the effects of effective pressure, in this case, temperature is set at 300 K or 30 ℃ and the values of the gravitational body force in reduced units are varied from 0.5, 1.0 and 1.5 in order to study the effect of effective pressure. For the effect of temperature, the temperature range 30, 40, 50, 60 and 70 ℃ is used to investigate the effect of temperature on the nano-droplet formation at the fixed reduced units force equal to 1.0.

4.3 RESULTS & DISCUSSIONS

This section presents the results obtained using the simulation model detailed in the previous section. This section can be separated into two portions. The first part is a validation step, where simulations of water droplet formation with nozzles of diameters of 10 and 30 microns are performed and compared to the reference [139] in order to validate the performance and accuracy of our MDPD model. The second portion will then use this MDPD model to investigate nano-droplet formation of polymeric ink with different effective pressure and temperature on different orifice diameters of 10, 50, 100, 500, and 1000 nm.

4.3.1 Validation of the Constructed MDPD Model

To compare our results to the reference study [139], there is a need to perform a unit conversion of the results in reduced units obtained from our MDPD simulations to real units. We show in this section that due to the large coarse graining level, N_m, the converted results in real units are unphysical. Hence, we came up with a conversion methodology to overcome this problem. This conversion methodology is presented, and the final comparison is depicted in the following subsections.

4.3.1.1 Problem due to Large Coarse-graining Level N_m

To illustrate the problem encountered due to the large coarse-graining level, N_m, the detailed conversion from reduced units to real units for the case of the 30 micron nozzle ($r_c = 15,000nm$) is presented here. Following the conversion table presented in Table 4.2, and the computed coarse-graining level presented in Table 4.5, we can arrive at the following fundamental quantities.

$$m_p = N_m M_w = 1.129 \cdot 10^{13} \times 18 \text{ amu} = 3.375 \cdot 10^{-13} \text{kg}$$

$$T = 300\ K$$

$$r_c = \ 1.50 \times 10^{-5} \text{ m}$$

$$E = k_B T = 4.142 \cdot 10^{-21}\ J$$

$$t = \sqrt{\frac{m r_c^2}{E}} = 0.135\ s$$

$$F = \frac{m r_c}{t^2} = \frac{E}{r_c} = 2.761 \cdot 10^{-16}\ N$$

$$P = \frac{F}{A} = \ 1.276 \cdot 10^{-4}\ Pa$$

$$V = \sqrt{\frac{E}{m}} = 1.108 \cdot 10^{-4}\ m/s$$

The MDPD simulated physical parameters in reduced units is than multiplied by these fundamental quantities to obtain the results in real units. Taking velocity as an example, let the reduced units result be $V^* = 2.20$, and the velocity in real

units be V_{real}. Then $V_{real} = V^* \times V$. The simulated results in reduced and real units are presented in Table 4.6 for both the 10 and 30 micron diameter nozzle.

Table 4.6: The simulation result of water droplet formation from 10 and 30 micron nozzle in reduced and real units.

Nozzle Size	10 micron		30 micron	
Unit	Reduced	Real	Reduced	Real
r_C (nm)	1	5,000	1	15,000
m (kg)	1	1.250E-14	1	3.375E-13
ε (J)	1	4.142e-21	1	4.142e-21
Time (s)	0.01	8.686e-05	0.01	0.0014
Velocity (m/s)	2.20	1.300E-03	2.20	2.437e-04
Force (N)	1	1.325E-11	1	4.418E-12
Pressure (Pa)	1	3.400E-03	1	1.276E-04
T (K)	1	300	1	300

From Table 4.6, we can see that the physical quantities in real units are too low to be physically meaningful, and this is a direct result of the large coarse graining factor necessary to accommodate the small simulation domain. The same problem is also noted in references [157-159]. In order to obtain physical quantities in meaningful orders of magnitude, the domain size has to be increased to a point where the computational cost will be impractically expensive. Thus, we came up

with a conversion strategy to adjust these physical quantities to a physically meaningful magnitude without having to increase the domain size.

4.3.1.2 Conversion Methodology

Although DPD is a truly scale-free method, which means that it is possible to scale DPD simulations into any desired length scale [160], the detailed computation above shows that the calculated results when we convert from reduced to real units may not be physically meaningful. By careful evaluation of the conversion process, we found that the crux of the problem lies with the small simulation domain and high level of coarse-graining. The large coarse graining factor results in a large intrinsic length scale, r_c, while the intrinsic energy ε still remains small. The intrinsic energy ε can be increased only if the simulation domain size is allowed to increase, but this will lead to undesirably large simulation domain and increased computational cost. This is the reason why the value of these physical quantities in real units are unrealistically low. This problem is significantly obvious for 3D inkjet printing because the simulated droplet velocity is far too low (at 10^{-3}-10^{-4}m/s – see Table 4.6) while the typical droplet velocity in 3D inkjet printing is between 1-10 m/s [161].

The idea behind this conversion strategy is to artificially increase the energy, ε, of the system without increasing the domain size. This is not the same as normal scaling laws in DPD where levels of coarse-graining are changed according to changes in the sizes of the domains [160, 162]. The increase in ε can be achieved

in the MDPD simulation by artificially adding polymeric ink in the constructed nozzle, while still keeping the other parameters and dimensions constant. This is illustrated in Figure 4.8. The energy measured during the simulation will increase in tandem with an increase in number of beads, since energy is directly proportional to the number of beads in the system. In this conversion strategy, instead of actually simulating the increase in number of beads, the energy of the system is artificially adjusted by modifying the conversion equation of energy ε (as shown in Table 4.2) from $\varepsilon = k_B T$ to $\varepsilon = C k_B T$. C is the factor that accounts for the artificial increase in number of beads as it is illustrated in Figure 4.8, that is, should the number of MDPD beads simulated be N_{beads}, the number of beads is artificially increased to CN_{beads} in this conversion. By adjusting ε in this way, the magnitude of time, pressure and velocity can be adjusted to a compatible order of magnitude for comparison with the reference study. By this conversion methodology, thus, DPD simulation in reduced units is possible to be converted into any desired length scale in real units, regardless of simulation domain size and level of coarse-graining.

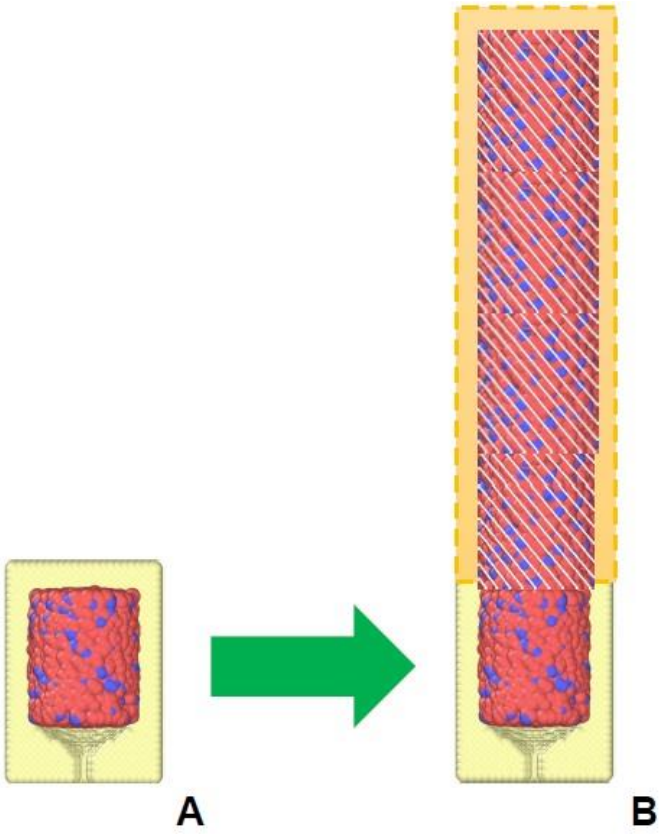

Figure 4.8: The illustration of the conversion methodology's concept.
(A) the simulation system **(B)** the system with artificial increasing of number of beads in order to adjust energy ε .

4.3.1.3 Validation of the Conversion Methodology

In order to validate this method of conversion, additional simulations are conducted with 32,000 and 64,000 beads, i.e. the values of $C = 2$ and 4 respectively when compared to the base case of 16,000 beads. We found that the results obtained through this conversion strategy from the base case is in good agreement with the actual run of simulation cases with 32,000 and 64,000 beads. This is shown in Figure 4.9, and we can see that the two results agree within 10%

range of error. With this, we conclude that the conversion strategy discussed herein is relatively accurate and can be considered as a useful alternative to increase the energy level to realistic values without extremely expensive computational cost.

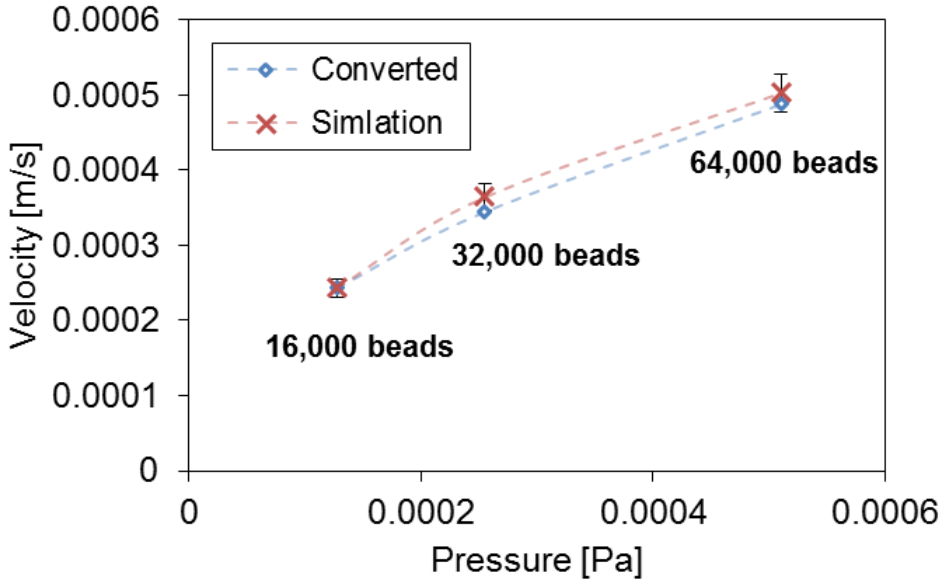

Figure 4.9: The validation to verify the compatibility between the converting method and actual MDPD simulation of 32,000 and 64,000 beads.

4.3.1.4 Comparison to a Physical Microscale Study

With the conversion strategy validated, it is then used to convert the simulated results, presented in Table 4.6, to a physically meaningful regime in real units. The converted results are presented in Figure 4.9, together with the experimental results from the reference study. It is to be noted that the pressure considered in reference study [139] is the applied pressure at the inlet of the inkjet chamber, whereas the pressure measured in MDPD is the effective pressure at the nozzle's end. For comparison, the effective pressure from MDPD's simulation

results can be converted to applied pressure using the efficiency of energy conversion data presented in reference [139] figure 4.10 (b) and (c). This efficiency of energy conversion measures the energy loss along the pathway of ink from the pressure inlet to nozzle's end.

As can be seen from Figure 4.10, there is good agreement between the results from MDPD simulation and those gathered from reference study. The simulation results exhibit the same trend as the experimental results, such that the smaller the nozzle, the higher the pressure needed to attain the same inkjet droplet velocity. The performance of MDPD simulations in the microscale is consistent with the reference within 10% range of error for both size of the nozzles. The reason behind this amount of 10% error is potentially caused by the different setup, since MDPD only simulates the end part of the nozzle. Furthermore, error can also occur because the observed pressure from both cases is related by a scaling constant according to the different methods of measurement: the applied pressure from experimental reference and the effective pressure from MDPD simulation that has been mentioned earlier.

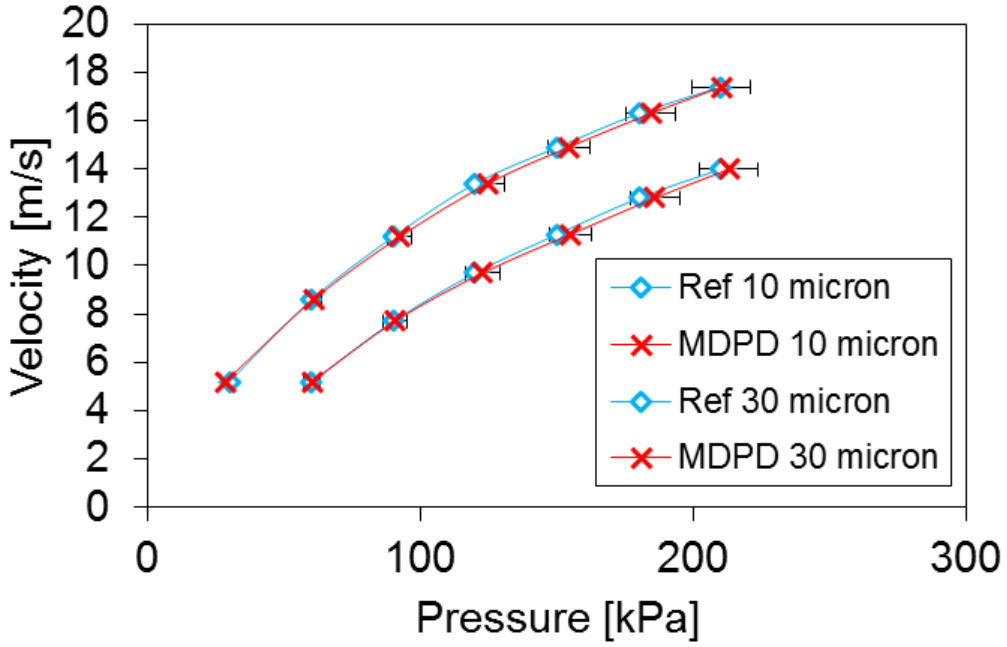

Figure 4.10: The comparison between reference study and simulation of 10 and 30 micron nozzles.

With these rigorous comparison, the MDPD model is considered validated. It will now be used to numerically characterized nano-droplet formation.

4.3.2 Numerical Study of Nano-droplet Formation

In this section, the nano-droplet formation of polymeric ink by MDPD (see Figure 4.11) is investigated numerically based on five coarse-graining levels determined by the corresponding diameters of the nozzle's end as listed in Table 4.4 (10, 50, 100, 500 and 1000nm nozzle). The aim is to examine the effect of effective pressure and temperature on nano-droplet formation that are important physical conditions and necessary to be considered in the actual working conditions of 3D nano-inkjet printing. To determine the conversion factor C to be

used in this section, velocity was used as a gauge. V_{real} was set to 5 m/s, since the typical droplet velocity in 3D inkjet printing is between $1 - 10$ m/s [161], and the conversion factor C was determined from this.

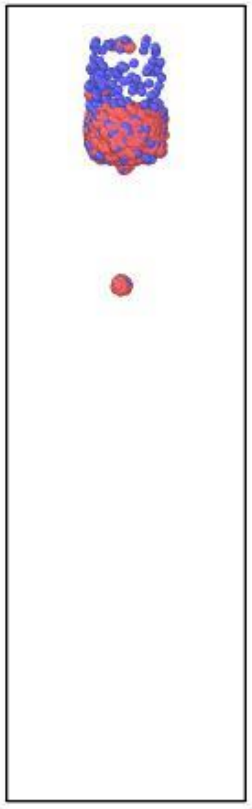

Figure 4.11: Nano-droplet formation of polymeric ink composing of oligomer (red) and monomer (blue) by using MDPD simulation (the nozzle is visualized).

4.3.2.1 The Effect of Temperature on Nano-droplet Formation

The results in Figure 4.12 show that the droplet diameter increases slightly with increasing temperature for all nozzle sizes. It is because the increasing

temperature lowers surface tension which allows the size of droplet becoming larger [163]. As temperature increases, the effective pressure at the nozzle's end to generate the droplet formation must also be increased correspondingly due to higher kinetic energy at higher temperature as it is shown in the column chart depicted in Figure 4.13. Figures 4.14 and 4.15 shows that the higher kinetic energy at higher temperature resulted in faster rate of droplet formation with lower droplet break-up time, and higher droplet initial velocity. It is necessary to consider these physical quantities in order to adjust the droplet diameter and proper droplet velocity in practical 3D inkjet printing as it is shown in this study that these are affected by the operation temperature.

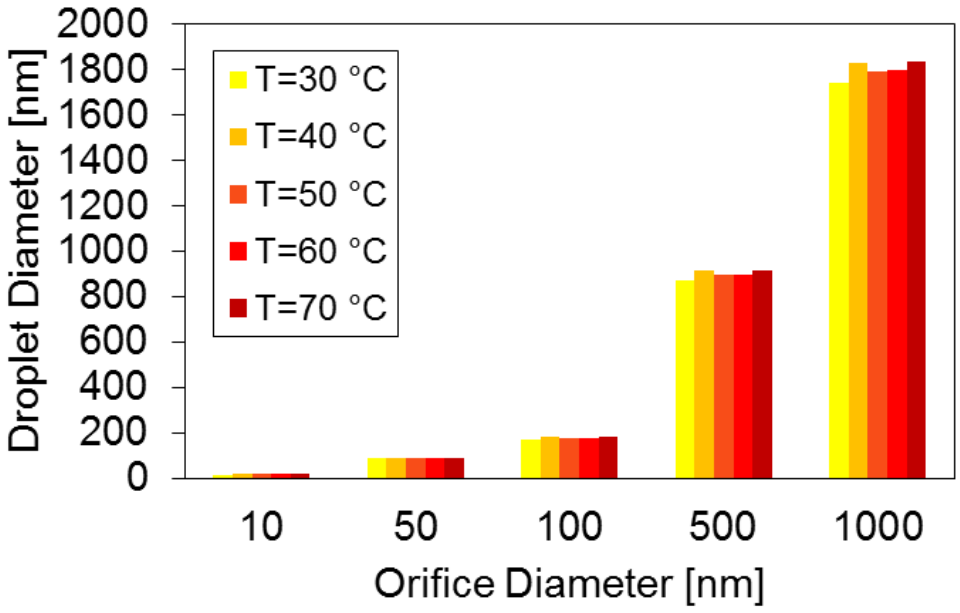

Figure 4.12: The effect of temperature on droplet diameter of various sizes of nozzle's diameter.

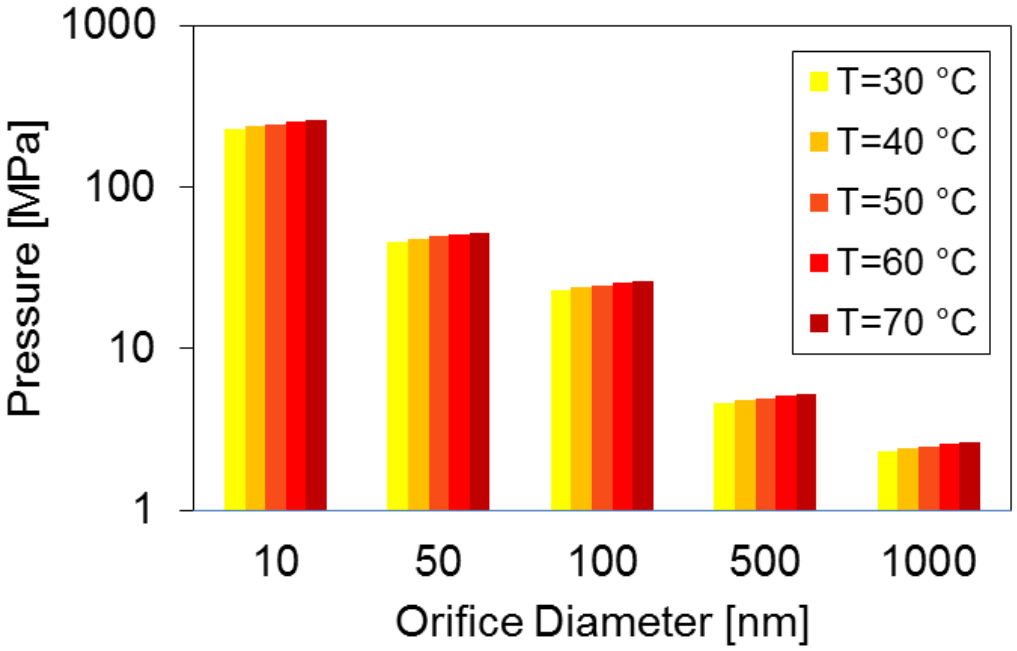

Figure 4.13: The effect of temperature on effective pressure of various sizes of nozzle's diameter.

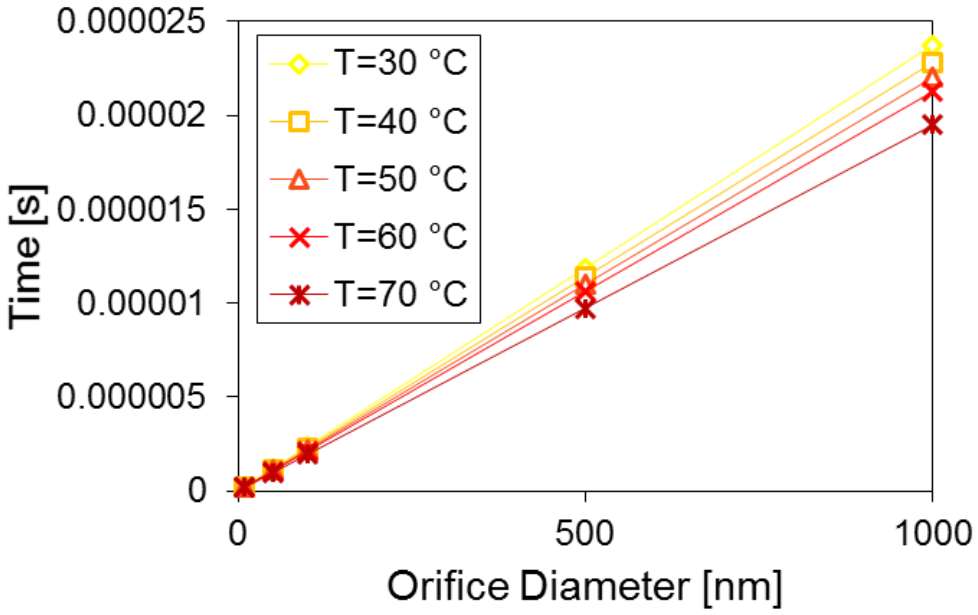

Figure 4.14: The effect of temperature on first droplet formation break-up time of various sizes of nozzle's diameter.

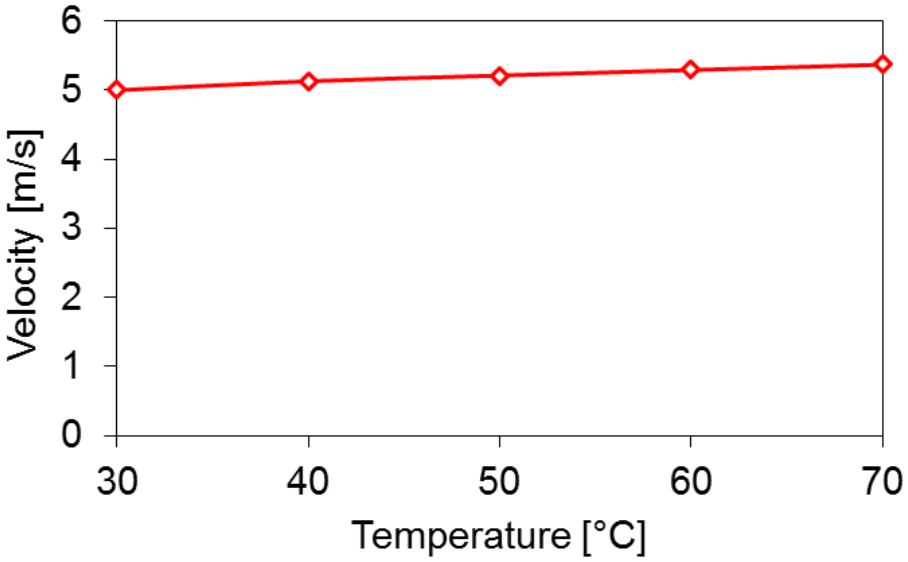

Figure 4.15: The effect of temperature on initial droplet velocity.

4.3.2.2 The Effect of Effective Pressure

As shown in Figure 4.16, the magnitude of effective pressure is directly proportional to the size of applied force and it is found that smaller sizes of nozzle require higher effective pressures in order to form nano-droplets. Due to small size of droplet, size of surface tension becomes larger resulting in higher disjointing pressure for droplet formation which is extremely high for nanoscale [164]. As an estimation for the size of effective pressure from the same figure, for example, the order of magnitude of effective pressure for 10 nm nozzle needs to be around 300 MPa in order to generate nano-droplet formation with a velocity of 5 m/s. Thus, it is obvious that effective pressures in smaller sizes of nozzle also have to be significantly large in order to generate the nano-droplets. The increasing trend of effective pressure reduces both the size of droplet diameter and break-up as can be seen from Figures 4.17, 4.18 and 4.19. Figure 4.17 illustrates the graphs shown in

Figure 4.18 and 4.19, and gave a pictorial description that the higher effective pressure results in a higher rate of droplet formation, and smaller droplet diameters in all sizes of the nozzle. In addition, by the comparison between Figures 4.15 and 4.20, we can conclude that increasing the driving force or effective pressure is more effective than the increasing of temperature in order to raise the nano-droplet velocity. Since the nano-droplet velocity affects the printing resolution (lower velocity, higher resolution), the ability to control nano-droplet velocity is one important factors to be considered in practical printing [165-167].

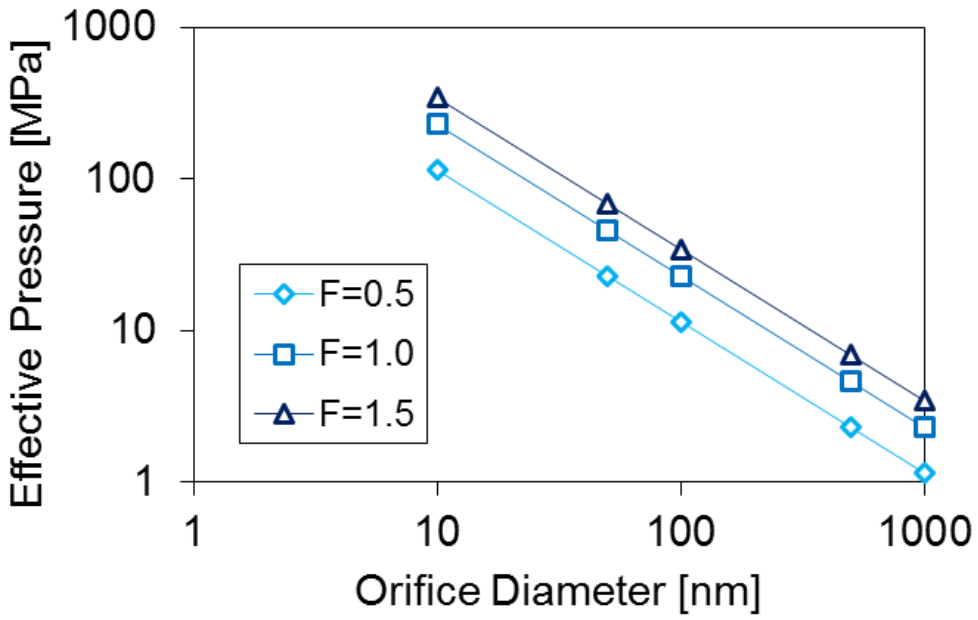

Figure 4.16: The effect of effective pressure (implemented by different sizes of force in reduced unit) of various sizes of nozzle's diameter.

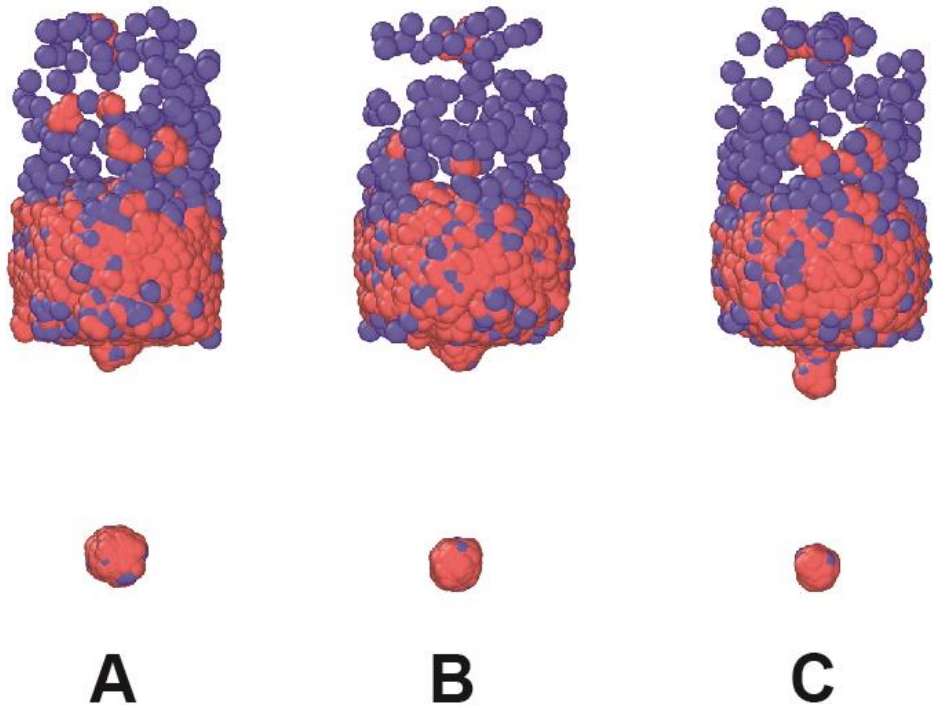

Figure 4.17: Nano-droplet formation at the same distance by magnitudes of effective pressure in reduced unit. (A) F=0.5, the droplet occurs at 38,500th steps (B) F=1.0, the droplet occurs at 15,100th steps (C) F=1.5, the droplet occurs at 10,200th steps.

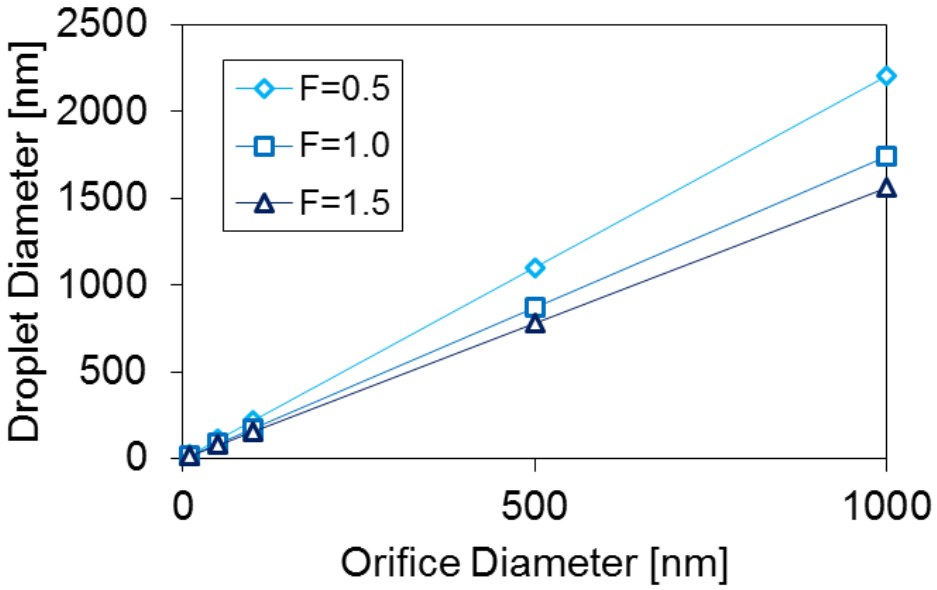

Figure 4.18: The effect of effective pressure (implemented by different sizes of force in reduced unit) on droplet diameter of various sizes of nozzle's diameter.

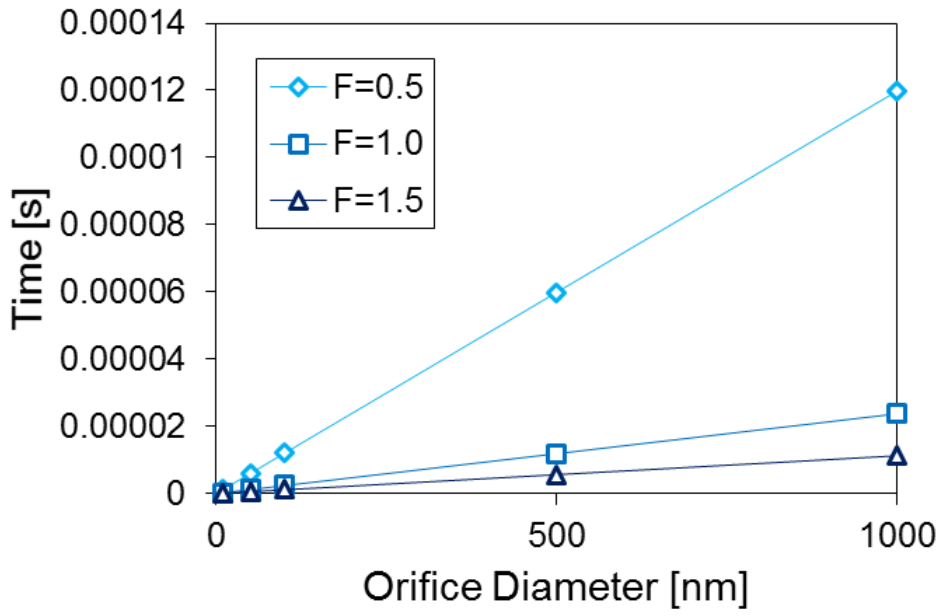

Figure 4.19: The effect of effective pressure on first droplet break-up time of various sizes of nozzle's diameter.

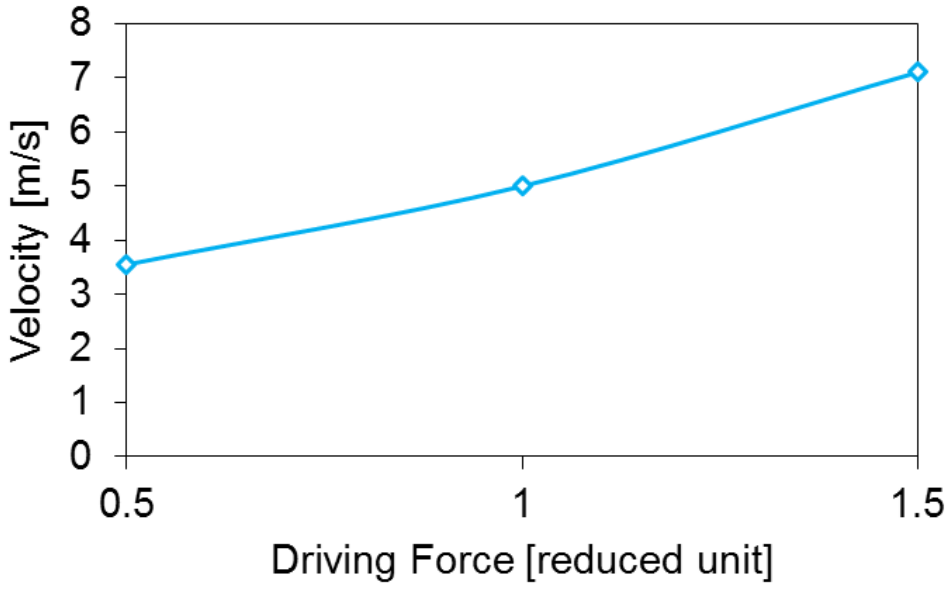

Figure 4.20: The effect of effective pressure on initial droplet velocity.

4.4 CONCLUSIONS

In this study, MDPD was effectively used to model the process of droplet formation in both micro and nano scale. The problem of large coarse-graining level when scaling up to microscale was also addressed in this study using a novel conversion methodology. In the numerical characterization of nano-droplet formation, it was found that the effective pressure needs to be higher in smaller nozzle diameters. Higher effective pressures can be used to reduce droplet diameter and droplet break-up time while higher temperatures will increase the size of droplet diameter with a decrease in break-up time.

Apart from these, it was found that MDPD can effectively capture agglomeration as a form of ink deposition on the nozzle's wall during droplet formation as observed in Figure 4.13. It will be interesting to investigate this finding further because ink deposition on the nozzle's wall can lead to nozzle clogging. This would be addressed in the next chapter.

CHAPTER 5 NUMERICAL STUDY OF SURFACE AGGLOMERATION IN 3D NANO-INKJET PRINTING BY MANY-BODY DISSIPATIVE PARTICLE DYNAMICS

In the previous chapter, ink deposition on the nozzle's wall was found to be a form of surface agglomeration that can potentially result in nozzle clogging. In this chapter, a surfactant is introduced into the MDPD simulation model to investigate the effectiveness of surfactant in controlling ink deposition on wall. The surfactant is modelled both implicitly and explicitly in this work. In an implicit model, a general surfactant is assumed, and the attraction parameter is tuned for optimal performance. On the other hand, the explicit model assumes a specific commercial UV ink composition with SDS surfactant, identical to that described in Chapter 3, and the interaction parameters are specifically computed. Apart from addition of surfactants, other possible solutions to reduce ink deposition on wall are proposed and discussed.

5.1 INTRODUCTION

To achieve continuous nanoscale flow and good working conditions of the 3D-inkjet nozzle, a major challenge to be addressed and overcome is the agglomeration of ink fluid, especially as there is a significantly higher chance of nozzle clogging in nanoscale flow [14]. Ink fluid agglomeration can occur within the ink fluid itself, or it can occur on the nozzle's wall. While the agglomeration process within the ink has been discussed extensively in Chapter 3, this chapter will focus on the agglomeration of ink on the nozzle's wall. Prior experimental research found that clogging is a result of the competition between particle–fluid, particle–surface and particle–particle interactions [168]. As MDPD includes attractive forces, not only can nano-droplet formation of UV ink be modelled, but agglomeration in the form of ink deposition on the nozzle's wall can also be simulated, as detailed in Chapter 4.

To investigate the possibility of using surfactants to control and reduce ink deposition on the inner surface of nozzle, a surfactant model must be added to the MDPD simulation. This necessitates the definition of surfactant specific interaction parameters. Here, the MDPD surfactant will be implemented with two different methods. The first method is an implicit method where no specific surfactant is assumed and the interaction parameters are varied in order to study the trend. This follows typical MDPD simulation process [122]. The second method is an explicit method, where the interaction parameters are calculated based on its molar volume and solubility parameter, in a manner similar to the calculation of repulsion

parameters in DPD simulations. In this explicit method, the UV ink composition commonly used in 3D inkjet printing, detailed in Chapter 3 [169], will be used.

In the next section, the research methodology in this study is detailed, with a focus on the modeling of surfactant implicitly and explicitly. Following this, the results of this study is discussed. In the implicit model, we discuss first the tuning of parameters to obtain a high quality surfactant that can potentially control ink-surface agglomeration. After that, we vary the percentage mass of surfactant to check the performance of surfactant in terms of quantity. In the explicit model, we discuss the performance of a specific surfactant, SDS, in controlling surface agglomeration in terms of both quality and quantity. Finally, we consolidate all the MDPD simulation results to understand the performance of surfactant and its effect on nano-droplet formation.

5.2 RESEARCH METHODOLOGY

The MDPD simulations are carried out similar to that described in Chapter 4 via LAMMPS. The major difference in this study is the addition of surfactants to the polymeric UV ink mix. Surfactants are implemented in MDPD as a molecule composing of a single hydrophilic bead (H) and a single hydrophobic bead (T). The standard value of -40 is used for the attractive interactions between the same type (A_{ss}, A_{ll}) and -25 for all repulsive interactions (B). These parameters are typical of MDPD simulations, as described in the simulation setup of the previous chapter, summarized in Table 4.3. The necessary attraction parameters to be defined are the attractions between the surfactants and ink, the H and T beads, and the surfactants and the nozzle's wall (as summarized in Table 5.1).

In the implicit method, in order to study the effects of surfactants in general, the trends of these attraction parameters are investigated. The effect of surfactants in this case will be examined in terms of their quality and quantity. In terms of quality, the optimal attraction parameters between surfactant and nozzle's wall will be explored. For quantity, the most suitable amount of surfactants in the ink composition and possible effects of addition of surfactants in nano-droplet formation will be determined. On the other hand, in the explicit method, these parameters are computed based on commercial UV ink composition. These are further elaborated in the subsections below.

5.2.1 Implicit Method

In the implicit method, the simplest form of UV ink, composing of only oligomers and monomers, are considered, as with that implemented in Chapter 4. This is to simplify the simulation and isolate the effects of surfactants. The new attraction parameters to model the surfactants are summarized in Table 5.1, and are derived based on the following considerations.

- The attraction between the surfactants and the nozzle's wall (A_{SW}) attraction is varied between -30 and -5. To prevent an overestimation of the surfactant's performance, this attraction parameter will be determined as the minimum needed for preventing the surfactant from depositing on the wall based on visual inspection.

- The attraction parameter between the H and T beads (A_{HT}) is varied between -30 and -5. To find the most suitable value, kinetic energy is used in this investigation because higher kinetic energy results in lower possibility in agglomeration [145, 170]. Thus, here we are looking for a value of A_{HT} that can provide the maximum kinetic energy for the ink system.

- The attraction parameters between the surfactants and the ink ($A_{HO}, A_{TO}, A_{HM}, A_{TM}$) is varied from -20 to -40 in four different cases to fully determine their effects. The four cases are summarized in Table 5.1. For example, the attraction parameter between the H beads and the ink is -40 while that of the T beads and the ink is -35 in case I. Here, kinetic

energy is also used as the gauge to decide on the optimal attraction parameters.

Subsequently, the parameters which demonstrated the highest quality is tested further with different mass percentages of surfactants in the ink's compositions, namely 0.2%, 0.6%, 1.0%, 3.0%, 5.0%, 7.0% and 10.0%. These are compared with results obtained without the addition of surfactants as a control. The ink deposition will be characterized by counting the beads of the ink that remain on the nozzle's wall after reaching an equilibrium. This will be compared with the results from the control.

Table 5.1: The summary of attraction parameters in implicit method.

Surfactant		I	II	III	IV
H-Oligomer attraction	A_{HO}	-40	-40	-40	-40
H-Monomer attraction	A_{HM}	-40	-40	-40	-40
T-Oligomer attraction	A_{TO}	-35	-30	-25	-20
T-Monomer attraction	A_{TM}	-35	-30	-25	-20
H-T attraction	A_{HT}	-30 to -5			
H,T-Wall attraction	A_{SW}	-30 to -5			

5.2.2 Explicit Method

The commercial UV ink detailed in Chapter 3 is modelled here. To recap, the ink composes of oligomers and monomers of polyethylene glycol (PEG) and polystyrene (PS) with benzophenone (BZP) as the photo-initiator, in the ratio 2.5:1:0.4. The surfactant used is SDS. The attraction (A_{ij}) between different types of MDPD beads will be calculated based on its molar volume and solubility parameter [171]. This is done by first computing the Flory-Huggins (χ_{ij}) parameters for each pair of beads using Equation 2.22 [106] by inputting the solubility parameters (δ_i and δ_j) of the interacting pair of beads, and the mean molar volume of that pair of beads (V_{ref}). Then, the attraction interaction parameter, A_{ij}, specific to MDPD implementation, can be estimated via Equation 5.40 [171], in a similar manner as the calculation of the repulsion parameter for DPD simulations in Chapter 3 by Equation 2.20.

$$A_{ij} \approx A_{ii} + 0.606\chi_{ij} \qquad \textbf{\textit{Equation 5.40}}$$

Note that A_{ii} is the attraction between the same kind of MDPD bead and this is equal to -40 as in typical MDPD simulation setup. The calculated parameters are summarized in Table 5.2.

Table 5.2: The summary of attraction parameters in explicit method.

	PEG	PS	BZP	SDST	SDSH
PEG	-40				
PS	-35.84	-40			
BZP	-36.84	-39.56	-40		
SDST	-34.87	-39.99	-39.62	-40	
SDSH	-38.22	-23.28	-25.63	-20.83	-40

Since no assumption is made on the nozzle wall, the attraction parameters between the surfactant and the nozzle's wall (A_{SW}) remains at -20, and that between the ink and nozzle's wall (A_{sl}) remains at -30, as determined in the implicit method.

5.3 RESULTS & DISCUSSIONS

5.3.1 Implicit Method

As described in Section 5.2.1, several attraction parameters, summarized in Table 5.1, has to be tuned for the addition of surfactants to our MDPD simulation model. The performance of the added surfactants in reducing agglomeration within the ink can be investigated by quantifying the system's kinetic energy because kinetic energy is a good measure of the probability of agglomeration: higher kinetic energy is correlated with reduced agglomeration [72]. Also, the performance of the surfactant in reducing ink deposition on nozzle's wall can be determined by visual inspection of ink deposition, or by quantifying the percentage of ink deposited on the wall. In this section, the set of parameters that defines the surfactant with the highest quality through these performance indicators would be determined.

5.3.1.1 Tuning of Parameters – Quality Study

The first parameter considered here is the attraction parameter between surfactant and wall, A_{SW}. It was found that reducing the attraction parameter between the ink and wall can prevent deposition of the ink on the nozzle's wall [172-174]. A suitable surfactant is one that does not deposit itself onto the wall. Compared to -25 of A_{SW}, the value of -20 for A_{SW} was determined to be the minimum required to prevent the surfactant from depositing on the wall by visual

inspection. In Figure 5.1, there is no surfactant as deposit on the nozzle's wall after the majority of has already moved down for A_{SW} at -20 while there is a few of surfactants left on the wall at -25.

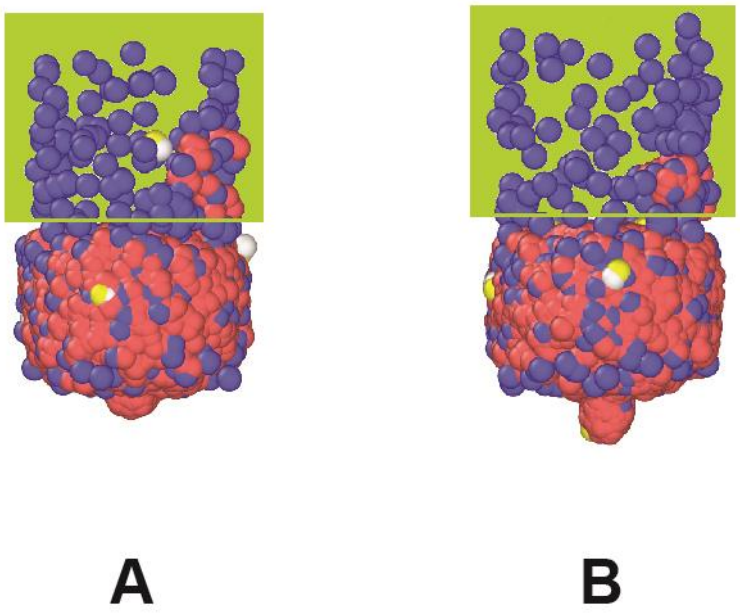

Figure 5.1: Investigation for the suitable A_{SW} based on ink deposition on the nozzle's wall (highlighted part), in this case, the ink compositions compose of oligomer (red), monomer (blue) and surfactant (white-H, yellow-T) by implicit method. The nozzle is hidden. **(A)** value of -25 for A_{SW} **(B)** value of -20 for A_{SW}.

With A_{SW} decided, A_{HT}, the attraction parameter between surfactant head and tail, is tuned next. An optimal surfactant is one that would reduce agglomeration, and hence, the A_{HT} which allows the entire system to have the highest kinetic energy would be chosen. The dependence on kinetic energy on A_{HT} is shown in Figure 5.2. It can be seen that the peak of total kinetic energy occurs at a A_{HT} value of -20 for all different cases. Thus, this value is the optimal attraction parameter to imitate the proper interaction between head and tail beads of the

surfactant model in general by the implicit method. In addition, at A_{HT}=-20, this magnitude of the attractive component is lower than that of the standard repulsion value (B_{ij}=25), resulting in non-wetting fluid behavior [123].

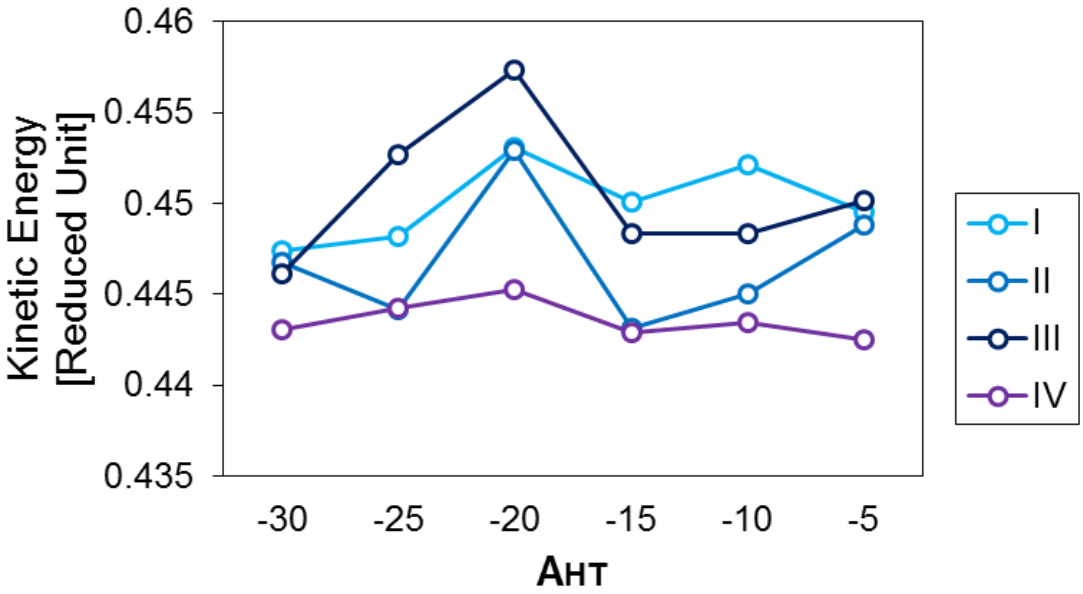

Figure 5.2: H-T attraction verification based on -20 of H,T-Wall attraction.

To tune the attraction parameters between the surfactant and ink ($A_{HO}, A_{HM}, A_{TO}, A_{TM}$), the four cases according to Table 5.1 are implemented. The resulting total kinetic energy for cases I, II, III and IV in reduced units are 0.453086, 0.452949, 0.457324 and 0.445218 respectively. Thus, the parameters used in case III is the most suitable because it resulted in the highest value of kinetic energy. From these simulation results, the values of -20 for both A_{SW} and A_{HT}, as well as the attraction parameters defined in case III will be used in all

subsequent simulations. The final attraction parameters optimized for surfactant's de-agglomeration performance are summarized in Table 5.3.

Table 5.3: The summary of final attraction parameters in implicit method.

H-Oligomer attraction	-40
H-Monomer attraction	-40
T-Oligomer attraction	-25
T-Monomer attraction	-25
H-T attraction	-20
H,T-Wall attraction	-20

5.3.1.2 Optimal Mass Percentage of Surfactant – Quantity Study

To investigate the effect of MDPD surfactant's loading amount on its performance, ink deposition on nozzle's wall can be easily measured in MDPD by visually looking at the amount of ink attached to the nozzle's wall throughout the simulation. Pictorial representation of the MDPD simulation with different amount surfactant composition is provided in Figure 5.3. It can be observed that the main source for this type of agglomeration is mostly due to monomer deposition. Also, visual inspections show that increasing the concentration of surfactants is concomitant with a reduction in ink deposition on the nozzle's wall. The quantitative result depicting the percentage of ink deposition on nozzle's wall at

different surfactant loading is presented in Figure 5.4. Here, it is clearly seen that there is a sharp reduction on ink deposition as surfactant mass increases from 0 to about 1%. As surfactant mass increases beyond 1%, the reduction tapers off with ink deposition staying constant at about 10%. These results demonstrate that surfactants can effectively reduce ink deposition on the nozzle's wall, by up to 87%, and only small amounts (about 1 wt%) are needed to improve the ink's hydrodynamic quality. This is in line with the current surfactant mass percentage used in commercial UV ink. From previous studies, it was found that the amount of surfactants inside UV ink compositions is normally less than 10 wt% [175, 176], with varying amounts for each specific kind of UV ink. For example, in UV curable acrylate-based ink, the percentage of surfactants added is 0.05 to 1.5 wt% [177]. Furthermore, some commercial UV curable inks usually has between 0.2-3.0 wt% [178-180] of surfactants. Thus, the simulation results here is relatively close to the actual amount in commercial applications.

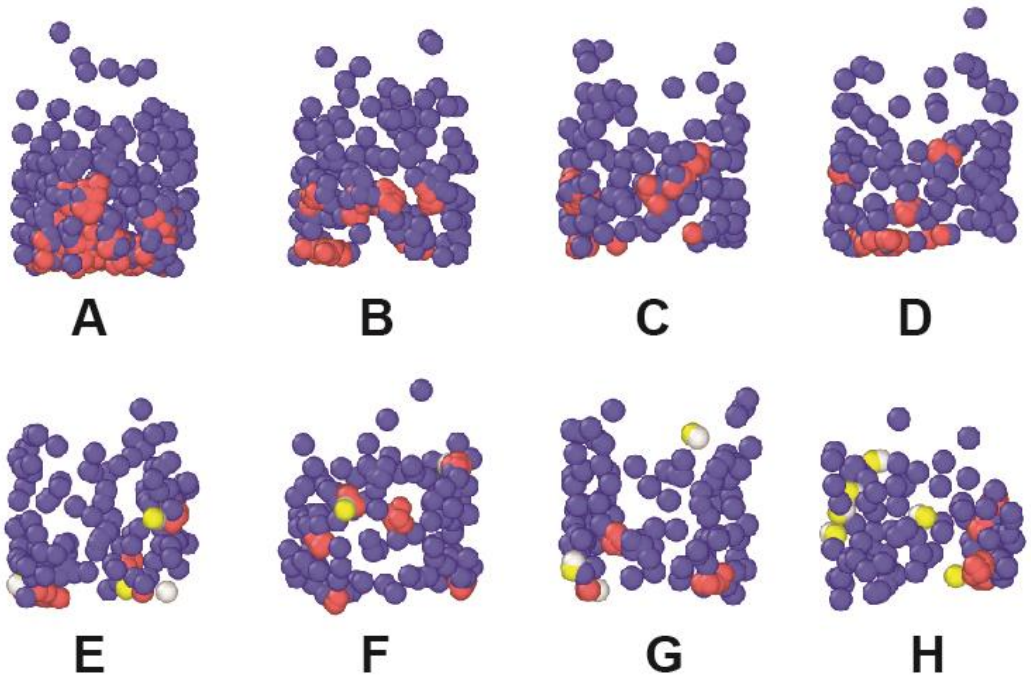

Figure 5.3: The ink deposition of oligomer (red), monomer (blue) and surfactant (white-H, yellow-T) by implicit method. The nozzle is hidden. **(A)** The UV ink without surfactant. **(B)** The UV ink with 0.2% of surfactant. **(C)** The UV ink with 0.6% of surfactant. **(D)** The UV ink with 1.0% of surfactant. **(E)** The UV ink with 3.0% of surfactant. **(F)** The UV ink with 5.0% of surfactant. **(G)** The UV ink with 7.0% of surfactant and **(H)** The UV ink with 10.0% of surfactant.

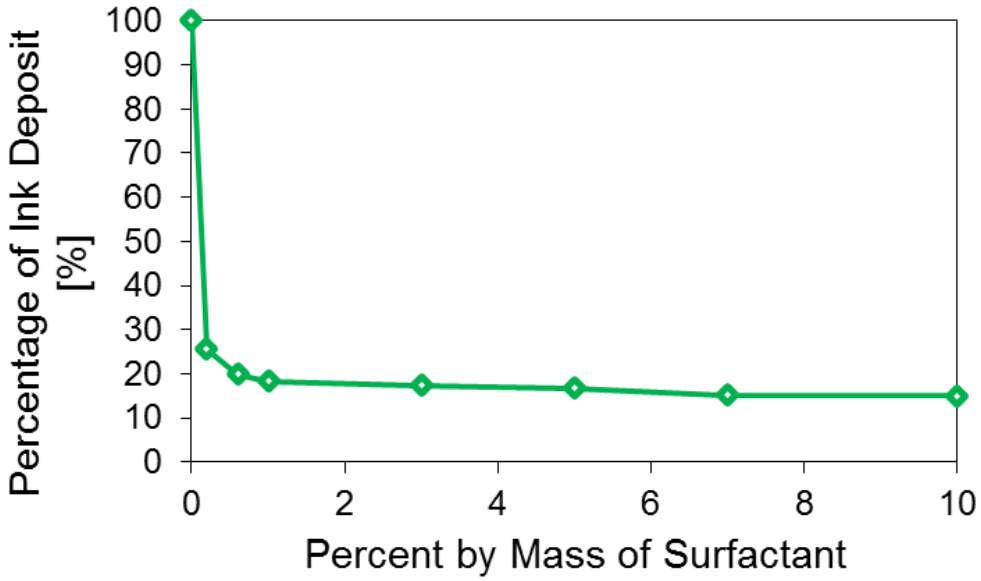

Figure 5.4: Surfactant performance by implicit method based on percentage of ink deposit on nozzle's wall.

If quantitative analysis is applied to the amount of monomer and oligomer in the deposit on the nozzle's wall, the deposit ratio of monomer is slightly higher than oligomer without surfactant (see Figure 5.5). The deposit ratio is significantly increased since small amount of surfactant starts the appearance. After that, the deposit ratio of monomer to oligomer is continuously increased due to the higher the percent by mass of surfactant. In this case, it is obvious that monomer is the main source of surface agglomeration especially when the amount of surfactant is increased.

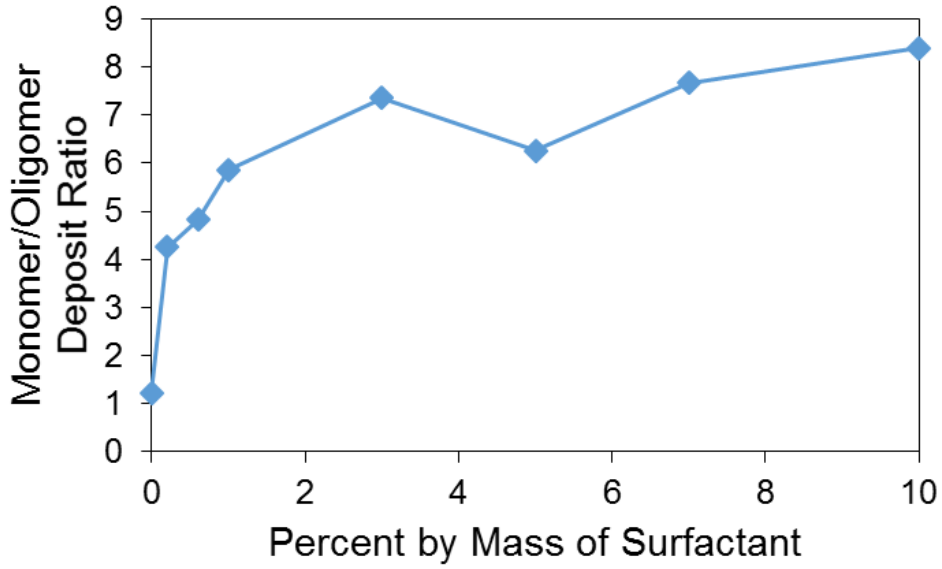

Figure 5.5: The deposit ratio of monomer to oligomer based on percent by mass of surfactant.

5.3.2 Explicit Method

Whilst the implicit method seeks to optimize surfactant's properties for effective de-agglomeration, modeling the surfactants explicitly is a more practical approach since a specific surfactant and ink composition is assumed. Instead of varying the attraction parameters and optimizing them, in this method, attraction parameters between MDPD beads of different types (A_{ij}) are instead calculated based on the molar volume and the solubility parameters of the ink's compositions, as computed in Section 5.2.2. The results from this explicit study is pictorially represented in Figure 5.6, and quantitatively in Figure 5.7. It can be seen that the explicit method gives similar results as the implicit method. The same trend where the addition of surfactants, in this case, specifically SDS, reduces surface

agglomeration can be visually observed, but by comparison with Figure 5.3 and Figure 5.4, the reduction is much less pronounced. Instead of reducing the agglomeration by 87%, the maximum reduction observed here is 60%, as shown in Figure 5.7. This is expected, though, since the surfactant derived using the implicit method is optimized for de-agglomeration (as described in Section 5.3.1.1), while the surfactant assumed in this case is a common surfactant available commercially, SDS. However, attraction values computed for SDS are actually relatively close to the values obtained in the implicit method via optimization (compare Table 5.3 and Table 5.2) especially A_{HT}.

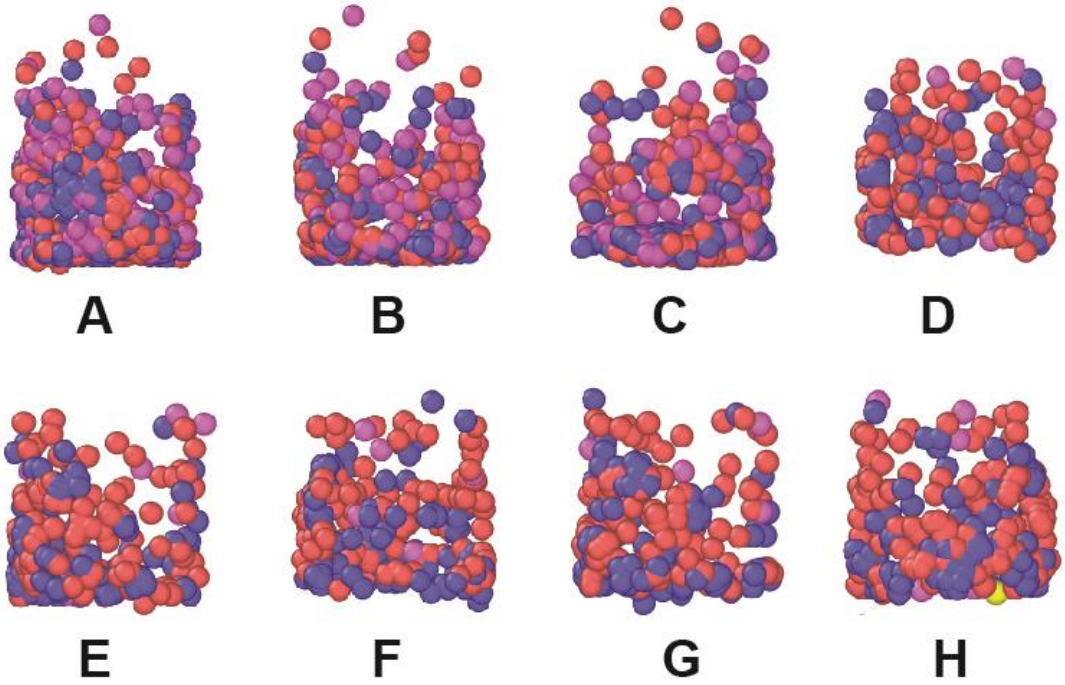

Figure 5.6: The ink deposition of PEG (red-monomer, oligomer), PS (blue-monomer, oligomer), surfactant (white-H, yellow-T) and photo-initiator (pink) by explicit method. The nozzle is hidden. **(A)** The UV ink without SDS. **(B)** The UV ink with 0.2% of SDS. **(C)** The UV ink with 0.6% of SDS. **(D)** The UV ink with 1.0% of SDS. **(E)** The UV ink with 3.0% of SDS. **(F)** The UV ink with 5.0% of SDS. **(G)** The UV ink with 7.0% of SDS and **(H)** The UV ink with 10.0% of SDS.

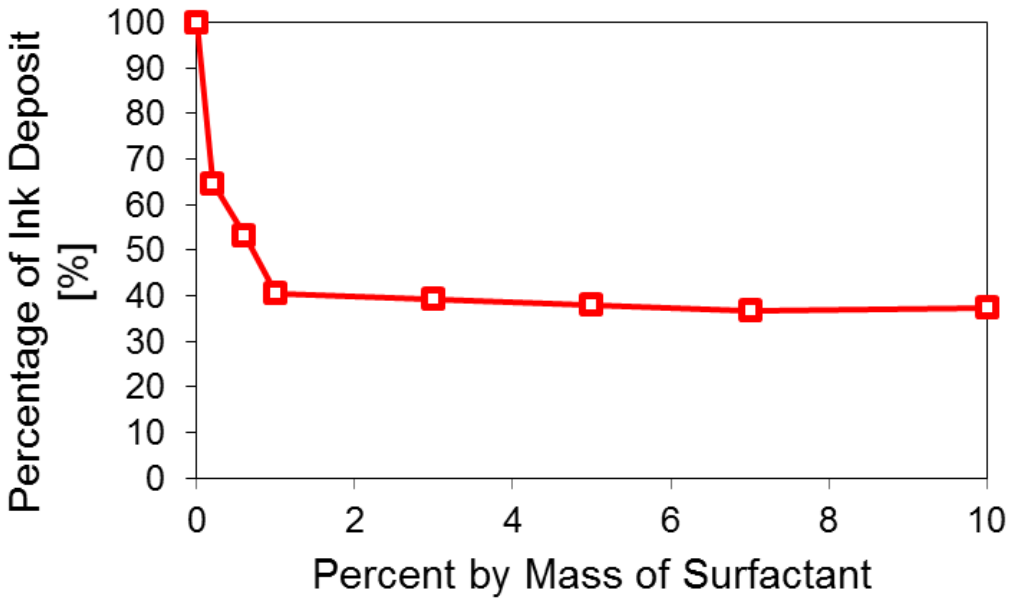

Figure 5.7: Surfactant performance by explicit method based on percentage of ink deposit on nozzle's wall.

Moreover, the significance of chemical effect of surfactant on deposit reduction is clearly investigated comparing with the effect of driving pressure. It is found that the driving pressure is needed to be increased to around 3.5 times in order to reach just nearly 20%. Normally, high velocity and high driving pressure can be used to prevent nozzle clogging [172] but it is not effective in this case because wetting behavior at nanoscale [181, 182]. Thus, the chemical effect of surfactant is superior to the mechanical effect on deposit reduction because only 1% of surfactant can reach 60% as previously discussed in Figure 5.8.

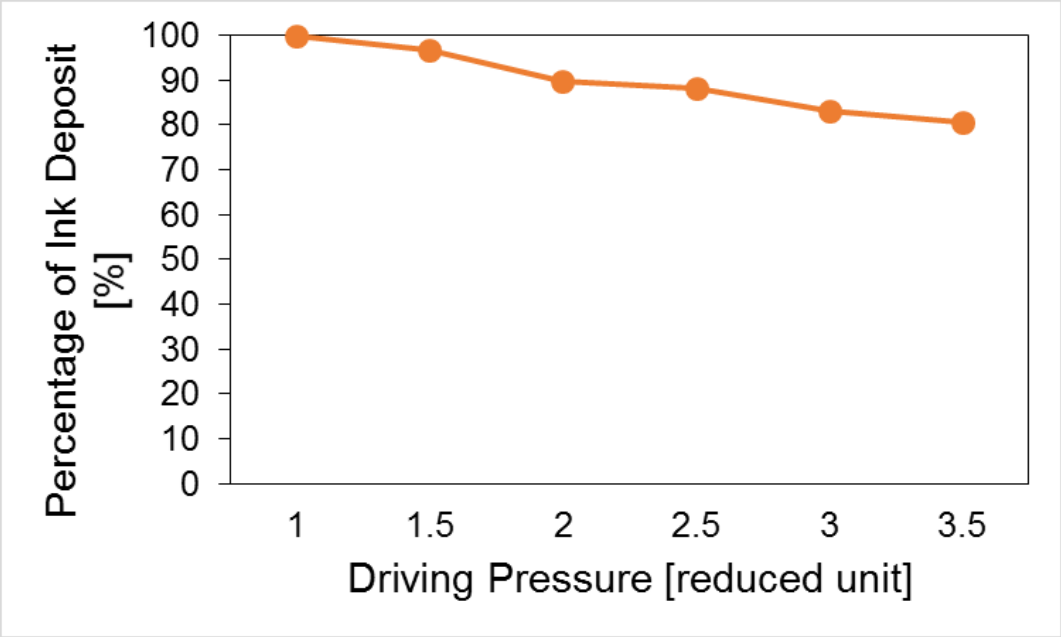

Figure 5.8: The effect of driving pressure's magnitude by explicit method based on percentage of ink deposit on nozzle's wall.

From the explicit method, it can also be concluded that the addition of commercially available surfactants may not be sufficient in controlling ink deposition on wall, since the maximum reduction in ink deposition is observed to be 60% even at high concentration of surfactants. In the event that no surfactants with the optimal parameters described in the implicit method can be found, further de-agglomeration techniques must be considered. This is especially important in the nanoscale, since the issue of nozzle clogging due to agglomeration is much more significant as compared to larger scales.

5.3.3 Additional De-agglomeration Techniques

From the results in previous section, the addition of commercially available surfactant SDS to complex UV ink compositions cannot effectively control ink deposition. More physical or chemical techniques are needed to prevent potential sources of nozzle clogging, since it is unknown at this point whether the optimal surfactant described in the implicit study can be found. Potential de-agglomeration methods include the use of electric fields and non-wetting coat on the nozzle's wall. In this case, electric field or electric charge is more popular in both experiment and simulation implementation [172, 183-185]. The use of such surface treatments effectively alters the interaction between ink and nozzle's wall, and this can be captured in our MDPD simulation model by adjusting the attraction between the ink and the nozzle's wall (A_{sl}). In this study, we vary the A_{sl} parameter from -30 to -25 to determine the effects of reduced attraction between the ink and the nozzle's wall. The results are presented in Figure 5.9 graphically and 5.10 pictorially. A surfactant concentration of 1 wt% is used here. It can be observed that the ink deposition is significantly reduced by 92% in this case, which is much better than the 60% achieved with the addition of SDS alone.

The effect of reduction in surface attraction alone is also observed in the same Figure. At the starting point that A_{sl} is equal to -30, 1% of surfactant can reduce 60% of surface agglomeration. When the attraction is continuously reduced by the increasing of A_{sl}, there is the convergence of both trend lines and the effect of surfactant is insignificantly higher than the effect of reduction in surface attraction alone at -25. Hence, it can be concluded that additional physical and

chemical de-agglomeration techniques can be considered for nanoscale printing in order to effectively eliminate ink deposition and create a sustainable printing condition without nozzle clogging.

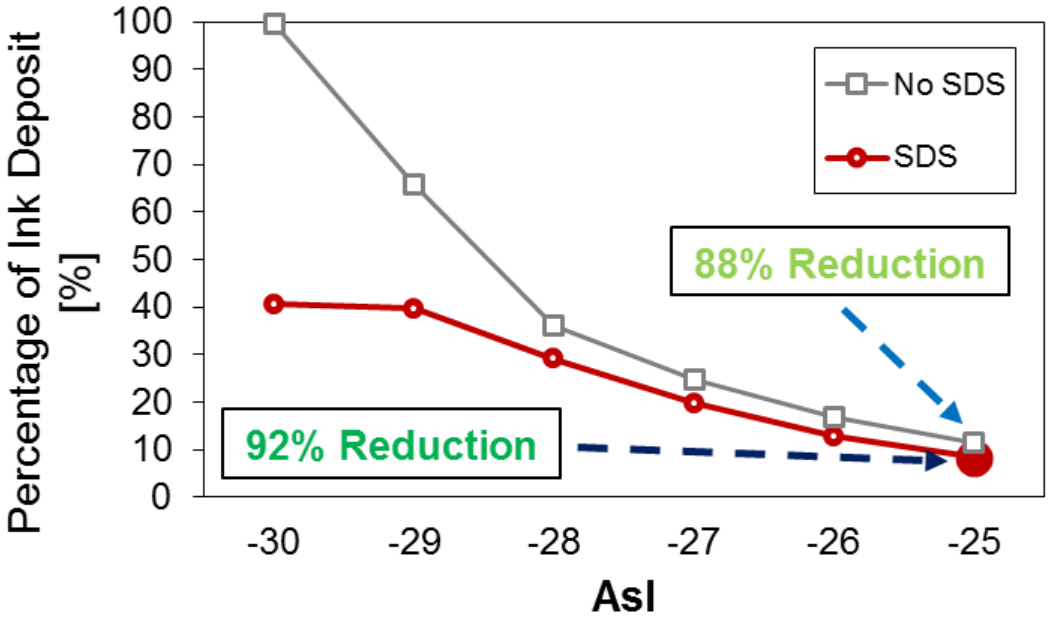

Figure 5.9: The effect of Ink-Nozzle's wall attraction on the percentage remainder of ink deposit.

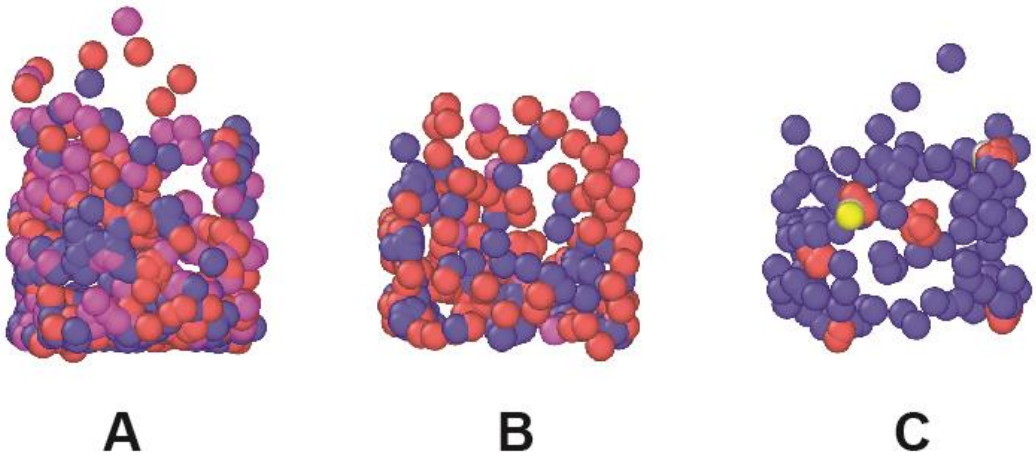

Figure 5.10: The ink deposition of PEG (red-monomer, oligomer), PS (blue-monomer, oligomer), surfactant (white-H, yellow-T) and photo-initiator (pink). The nozzle is hidden. **(A)** The UV ink without SDS **(B)** The UV ink with .01% of SDS (attraction between ink and nozzle's wall to be -30) and **(C)** The UV ink with 1.0% of SDS and the adjusted attraction between ink and nozzle's wall to be -25.

5.3.4 The Effect on Nano-droplet Formation

Normally, the driving pressure is the main controlling effect on nano-droplet size, velocity and break-up time that is the spending time after driving pressure is applied until the droplet is fully developed. In Figure 5.11, it is obvious that the higher driving pressure results in smaller nano-droplet size, faster velocity and lower break-up time.

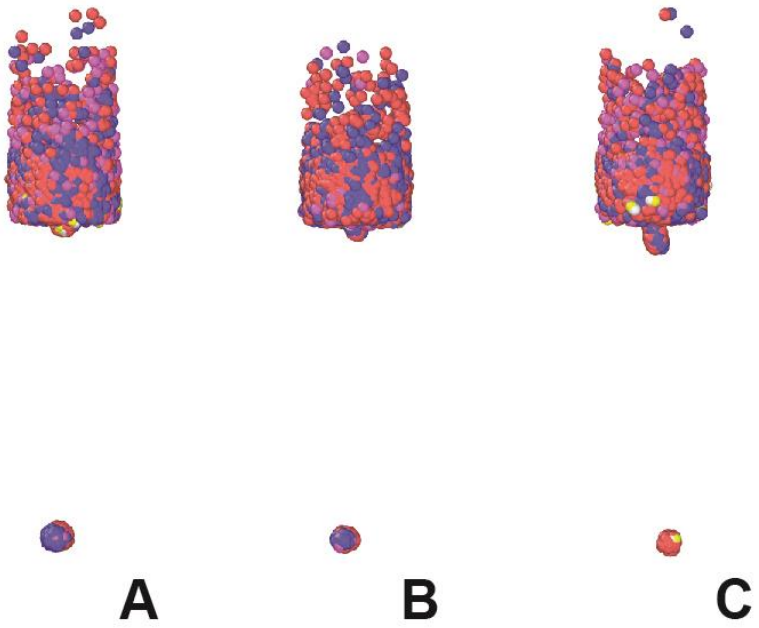

Figure 5.11: Nano-droplet formation at the same distance by magnitudes of effective pressure in reduced unit. **(A)** F=0.5, 329 MDPD beads appear as a droplet at 39,000th steps **(B)** F=1.0, 194 MDPD beads appear as a droplet at 15,600th steps **(C)** F=1.5, 112 MDPD beads appear as a droplet at 8,900th steps.

However, there are several observable effects of the addition of surfactants on nano-droplet formation of the ink. The results from both implicit and explicit simulations (see Figure 5.12) show that the total kinetic energy of the system

increases significantly with the addition of surfactants. This is positive, since increase in kinetic energy implies a lower probability of agglomeration. It can also be seen from Figure 5.12 that the increase in KE is sharp when the mass percentage of surfactant is increased from 0 to 1%, but tapers off with further increase in surfactant mass percentage above 1%. This trend is in agreement with that observed in Section 5.3.1 and 5.3.2, where further addition of surfactant beyond 1 mass percent shows little reduction in surface agglomeration.

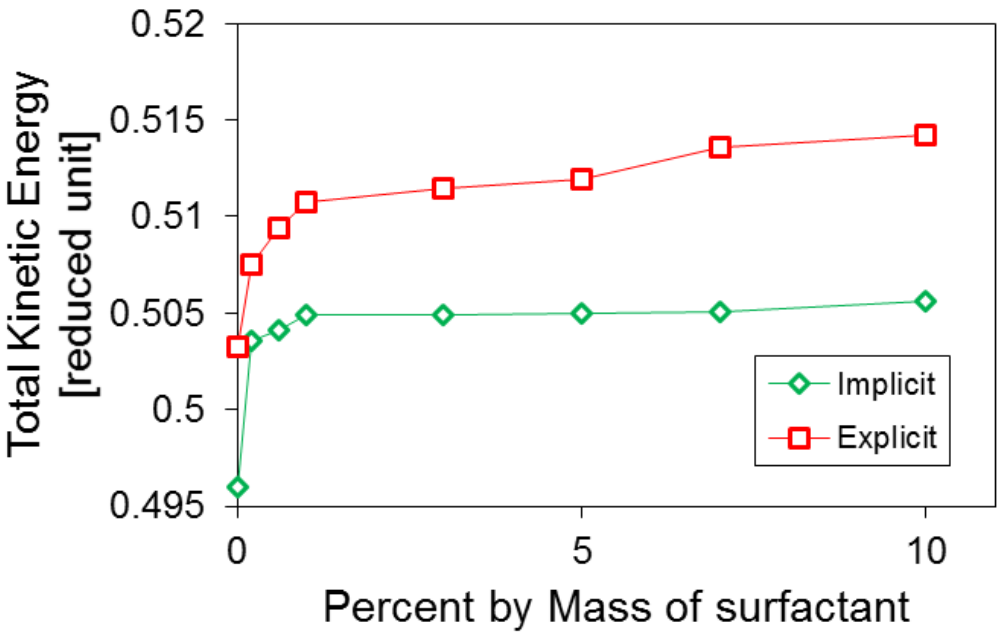

Figure 5.12: Total kinetic energy of ink system by implicit and explicit method at different percent by mass of surfactant.

During the formation of nano-droplets, their velocity and breakup time are also significantly affected by the amount of surfactants added. This is shown in Figure 5.13 and 5.14. From Figure 5.13, nano-droplet velocity increases slightly with the increase in mass of surfactants added, in both implicit and explicit cases.

On the other hand, Figure 5.14 shows that increasing the amount of surfactants reduces the nano-droplet breakup time. The same effects were observed in Chapter 4 when temperature was increased. This increase in nano-droplet velocity and reduction of nano-droplet breakup time can be significantly advantageous to speed up printing process, especially when the printing process of very small scale 3D printing is known to be slow [186, 187].

Thus, from these results, it can be concluded that the effect of surfactants is relatively similar to the effect of increasing temperature in terms of velocity and breakup time, but the addition of surfactants is more energy efficient as compared to using thermal means. Therefore, the addition of surfactants is not only a good choice to improve the ink quality in reducing agglomeration but also improving printing efficiency via the increase of nano-droplet velocity and reduction of breakup time.

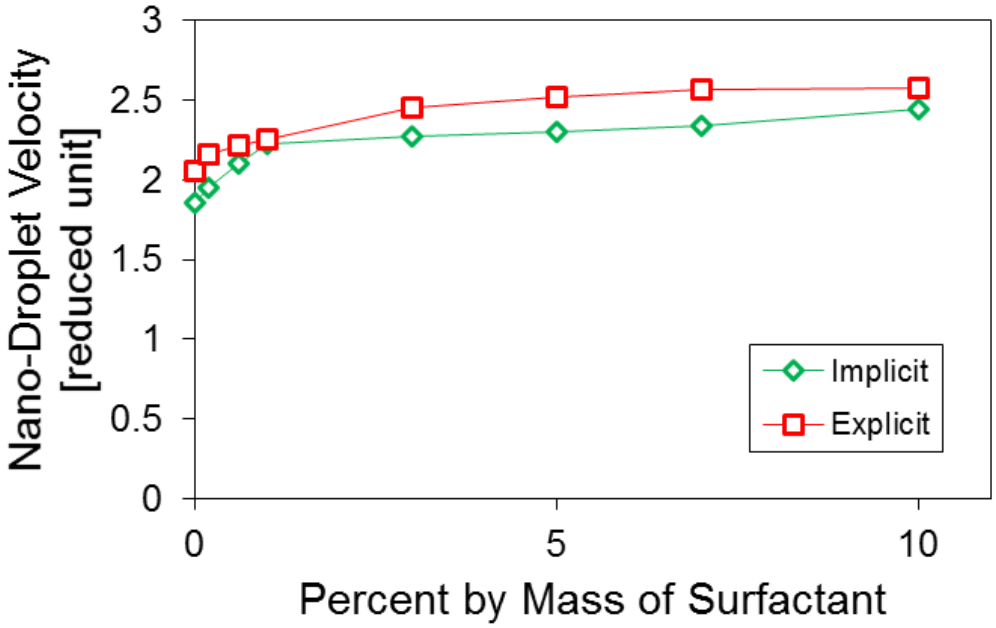

Figure 5.13: Nano-droplet velocity by implicit and explicit method at different percent by mass of surfactant.

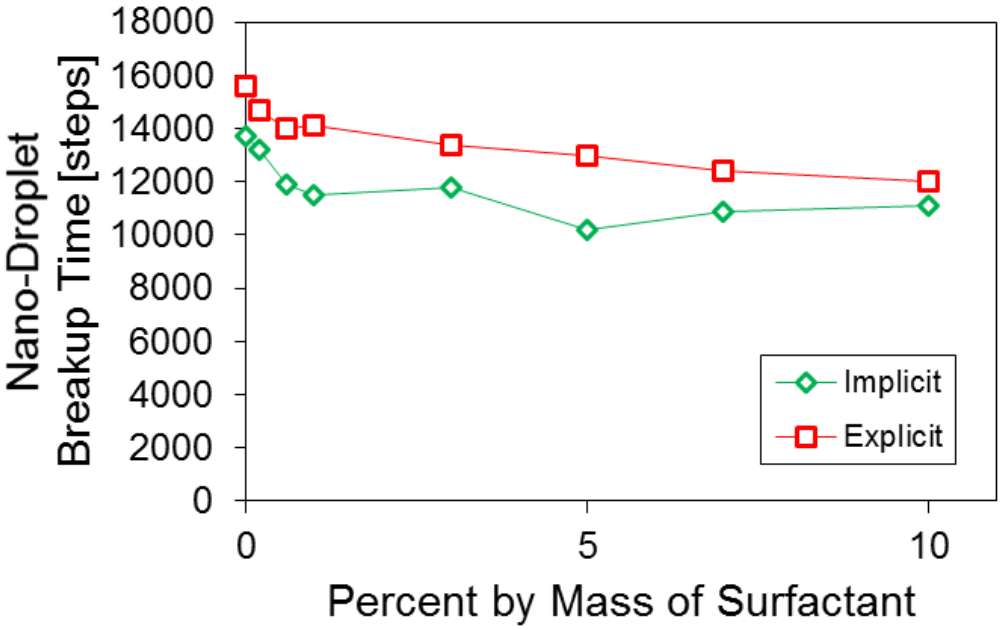

Figure 5.14: Nano-droplet break-up time by implicit and explicit method at different percent by mass of surfactant.

In addition, only small amounts of surfactants are recommended to improve the hydrodynamic quality of the ink, since it is clear from this study that additional amount of surfactants will not provide significant improvements. If ink agglomeration is not improved satisfactorily with the addition of small amount of surfactants, additional de-agglomeration techniques can be applied to control ink agglomeration by reducing A_{sl}. The results based on Figure 5.15-5.17 show better improvement of the total kinetic energy compared to the performance of surfactant alone and it also can significantly increase the nano-droplet's velocity and reduce breakup time.

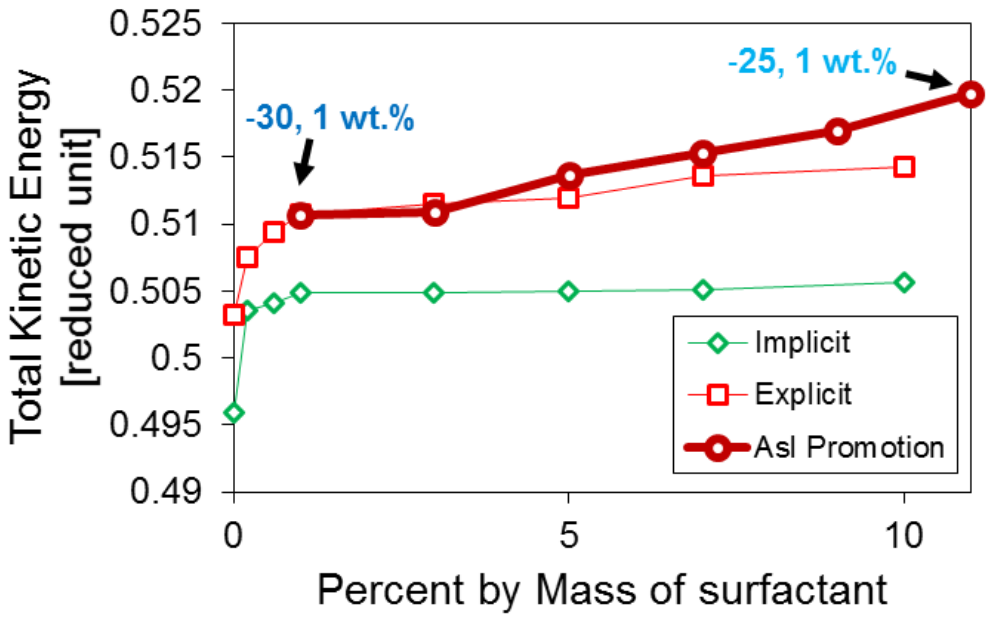

Figure 5.15: Total kinetic energy of ink system by additional de-agglomerations method at different values of A_{sl}, from -30 to -25 at 1% of surfactant.

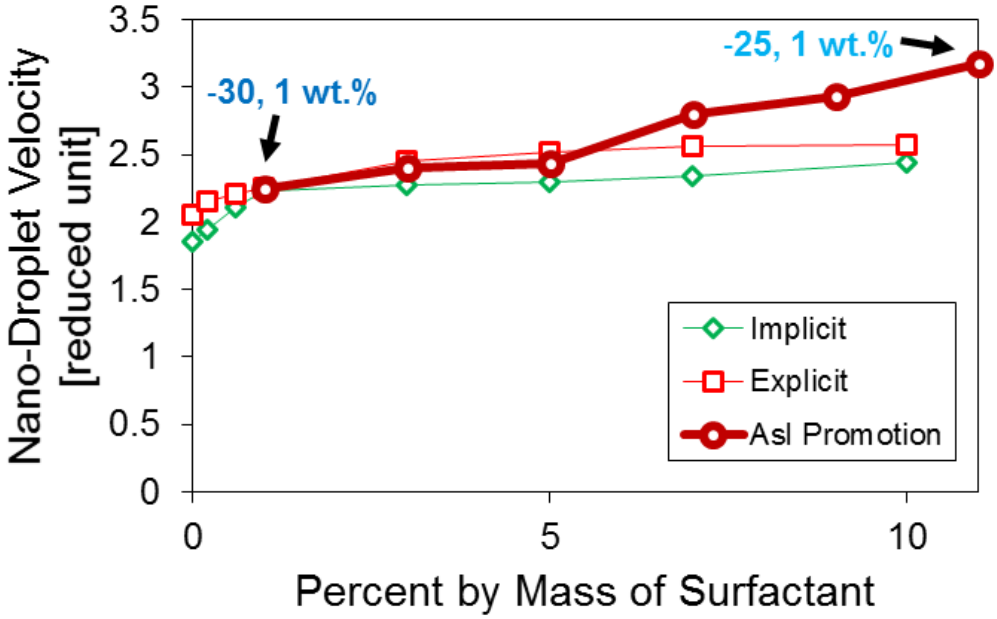

Figure 5.16: Nano-droplet velocity by additional de-agglomerations at different value of A_{sl}, from -30 to -25 at 1% of surfactant.

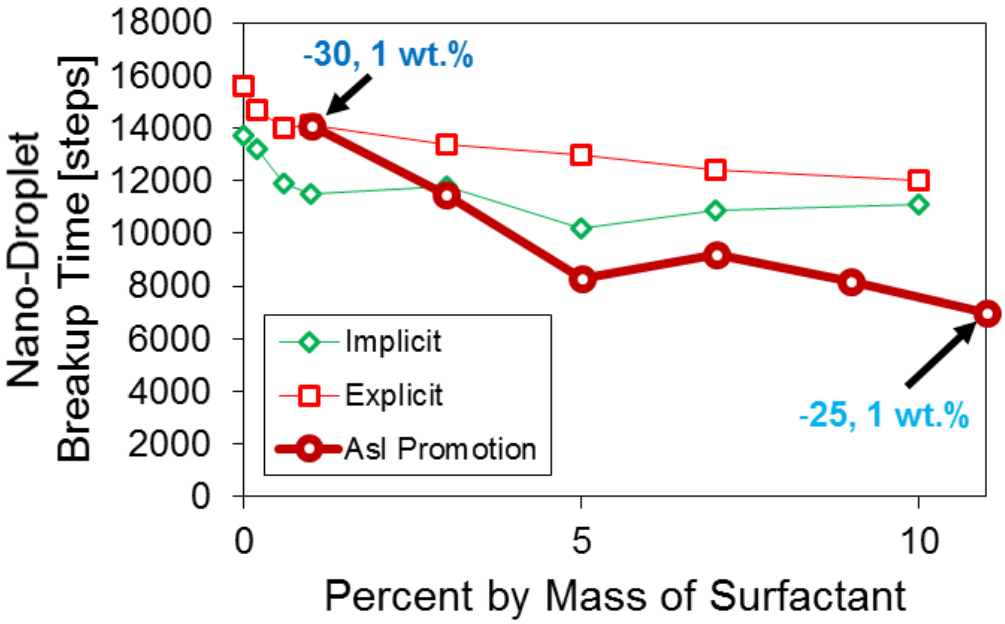

Figure 5.17: Nano-droplet breakup time by additional de-agglomerations at different values of A_{sl}, from -30 to -25 at 1% of surfactant.

5.4 CONCLUSIONS

In this section, surfactants were effectively simulated using MDPD to characterize its effects on nano-droplet formation in 3D inkjet printing. Modelling surfactants in MDPD simulations requires additional attraction parameters to be considered: namely those between the surfactant and the nozzle's wall; the H and T beads; and the surfactant and ink. These attraction parameters must be suitably defined in order to accurately predict the ability of a surfactant to control and reduce all potential sources of agglomeration. Both implicit and explicit methods are used to define these attraction parameters. The surfactant derived from implicit method is optimized for de-agglomeration, achieving a 87% reduction in ink-nozzle agglomeration. However, it is unknown whether such a surfactant indeed exist. On the other hand, a commercially available surfactant, SDS, is used in the explicit method, which achieves only 60% reduction in ink-nozzle agglomeration. In addition, the surfactant's attraction values computed both methods are relatively close to each other especially A_{HT}.

In terms of quantity, both the implicit and explicit method showed that small amounts of about 1 wt% of surfactants is sufficient for reducing ink deposition. Increasing the amount of surfactants beyond 1 wt% did not provide further improvements. The presence of small amounts of surfactants can also slightly affect important parameters during nano-droplet formation, as it increases the total kinetic energy of the ink compositions and nano-droplet velocity, while the breakup time is reduced.

Results from this study also demonstrated that the addition of surfactants alone may not satisfactorily control ink deposition in commercial UV inks, since it was shown using SDS that the ink deposition can reduce by only 60%. Should an optimal surfactant as derived using the implicit method be found to be non-existent, further physical or chemical de-agglomeration techniques are needed. Examples of such de-agglomeration techniques include the application of an electric field or a non-wetting coat. These are modelled in MDPD by adjusting the attraction parameters between the ink and the nozzle's wall in order to better control ink deposition. By combining these de-agglomeration techniques with addition of SDS surfactant, it is shown that ink deposition can be reduced by nearly 92%.

Thus, our MDPD simulations demonstrate that the use of surfactant additives with physical and chemical de-agglomeration methods can significantly reduce and control ink deposition in order to maintain stability during nano-droplet formation in 3D nano-inkjet printing.

CHAPTER 6 CONCLUSIONS & FUTURE WORK

6.1 CONCLUSIONS

Several challenges faced in recent efforts to advance nanoscale 3D inkjet printing can now be analyzed numerically due to advances in the computational simulation techniques of DPD and MDPD. In this thesis, agglomeration, one of the main challenge in nanoscale 3D inkjet printing that causes nozzle clogging, is thoroughly addressed using a combination of DPD and MDPD simulations. DPD simulations were performed to investigate the aggregation morphology of commonly used UV ink, mainly composed of oligomers or monomers of PEG and PS, and a photo-initiator (BZP). From the simulations conducted, it was found that the PEG to PS ratio of 3:1 gave the best agglomeration morphology in terms of the particle uniformity, agglomerate size, and particulate dispersion. To promote more desirable agglomeration morphology, a suitable surfactant, SDS, was introduced into the ink composition. Simulation results showed that the addition of SDS effectively broke down large agglomerates, from 520Å to 440Å, with an improved distribution, from 7 clusters to 14 smaller clusters. Thus, it can be concluded that the addition of SDS can effectively reduce the risk of nozzle clogging and form better dispersion uniformity.

In order to examine nano-droplet formation in a nano-sized nozzle, the MDPD method was used instead of the DPD method, since MPDP accounts for attractive forces between the DPD beads, thereby allowing vapor-liquid coexistence. To validate the MDPD model, efforts were made to compare the results from our MDPD model to a microscale experiment published previously. Good agreement was found, where the MDPD model was consistent to within an error of 10%. Through the validation process, we also found that the unrealistic low numerical values of physical parameters (like pressure or velocity) from MDPD simulations were caused by the small simulation domain. To overcome this problem, a new conversion methodology was proposed. The new conversion methodology works by artificially adjusting the energy of the simulated system to increase the numerical values of various physical quantities to realistically achievable range. This allows us to use the MDPD simulation results to provide further insights into possible trends of various physical quantities in nano-droplet formation. One of the conclusions drawn from this study is that a substantially higher driving force was needed to initiate nano-droplet formation as nozzle sizes decrease. The estimated effective pressure at the end of a 10 nm nozzle was on the order of 300 MPa for generating nano-droplet formation at a velocity of 5 m/s. It was further found that all of the physical quantities related to nano-droplet formation investigated in this study (droplet's diameter, droplet velocity, and droplet break-up time) were influenced by temperature and pressure. It was found that higher temperatures and applied pressures promoted faster nano-droplet

formation by reducing droplet break-up time and increasing droplet velocity. In addition, higher temperatures increased the droplets' diameter while higher effective pressures reduced it.

Another potential source of agglomeration is the attraction between the ink and the nozzle's wall, resulting in the formation of ink deposits. The same composition of UV ink in prior DPD simulations was used again with the same surfactant in MDPD to investigate its performance in controlling ink deposition on the nozzle's wall. 0.2-3.0 wt% of surfactant was found to be sufficient for enhanced performance. The addition of SDS was found to reduce the amount of ink deposition on the wall by 60%. However, as the leftover amount of ink deposit (40%) was considerably high even with the addition of SDS, other de-agglomeration technique was considered to improve the performance further. By applying physical or chemical techniques such as an electric field or a non-wetting coat, the attraction between ink and nozzle's wall could be reduced to control the ink deposition. Through this combination, the reduction in ink deposition increased from 60% to nearly 92%. Furthermore, this series of simulations also revealed that the presence of small amount of surfactants slightly affected the physical quantities during nano-droplet formation: the total kinetic energy of the ink compositions and nano-droplet velocity were increased while nano-droplet breakup time was reduced.

In this thesis project, DPD and MDPD simulations were effectively used to study the different forms of agglomeration that could occur in nanoscale 3D inkjet printing, and the results can help to solve the associated challenges faced in its

future development. The reduction and control of agglomeration can be investigated in a high-throughput manner by varying the composition of the ink, the inclusion of surfactants, while implementing other physical or chemical de-agglomeration techniques. The resulting nano-droplet formation can also be investigated and general trend of important physical quantities can be provided to guide the actual implementation of nanoscale inkjet-based additive manufacturing technology.

6.2 SUMMARY OF NOVELTIES & CONTRIBUTIONS

The main novelty in this thesis project is that it is the first numerical work using Dissipative Particle Dynamics (DPD) and Many-body Dissipative Particle Dynamics (MDPD) simulation techniques in the field of additive manufacturing (3D inkjet printing). DPD and MDPD is found in this thesis to be a powerful tool to model this phenomenon due to their appropriate length scale and cost effectiveness.

Thus, this thesis can potentially inspire more work in the use of such mesoscale techniques to study nano-droplet formation. The thesis consists of 3 main parts:

1. The first focuses on the use of DPD to study agglomeration problem, which is one of the main challenges impeding the breakthrough of 3D nano-inkjet printing.
2. Thereafter, MDPD was used to perform a numerical study on nano-droplet formation and characterize the effect of important physical parameters.
3. The third study involved the study of surface agglomeration, which is also envisaged to be a leading challenge in nanoscale 3D nano-inkjet printing.

The MDPD model built for this study is the first of its kind and can be used in the future for more extensive studies in the field of 3D nano-inkjet printing. In the sections below, the novelty and contributions of each part of the thesis will be further elaborated.

Part I: Numerical Characterization of Ultraviolet Ink Fluid Agglomeration and the Surfactant Effect

- This is the first study done on the numerical analysis of UV ink commonly used in 3D printing nowadays using DPD to understand the agglomeration morphology and surfactant effect
- This work studied different ratios of the ink composition that can result in different agglomeration morphologies and level of dispersion uniformity. From this study, an optimal ratio is found which can reduce agglomeration and increase dispersion, which can potentially contribute to future experimental work and physical implementation.
- The contribution of additives is studied in detailed here to investigate its effects on agglomeration, and how they can be used to alleviate the problem. From this research, it was found that the surfactant (SDS) can reduce the average size of agglomerates and increase dispersion uniformity resulting in improvement of UV ink's quality. This can again potentially contribute to future experimental work and physical implementation.

Part II: MDPD Simulations of Nano-droplet Formation in 3D Nano-Inkjet Printing

- A detailed optimization study was done in this part of the thesis to come up with a suitable attraction value for solid-liquid interaction (A_{sl}=-30) which is required to model the nano-droplet formation phenomenon in MDPD.

This value was optimized in this study based on theoretical and experimental considerations, and otherwise cannot be found in existing literature.

- A novel unit conversion methodology is introduced in this thesis to artificially gain physically meaningful results in real units. This conversion method is required as the small simulation domain and large coarse graining level leads to physically unmeaningful results (for instance, unphysically low velocity and applied pressure). This is a common problem in DPD and MDPD simulations, and typically, the simulation domain has to be enlarged to solve this issue. This leads to unrealistically large computational time. By artificially adding MDPD beads of ink inside the system, it can scale up the simulation model via increasing of force and energy without interfering with the relationships between physical parameters. Actual simulations (32,000 and 64,000 beads of MDPD ink) were additionally performed to validate the unit conversion methodology. This conversion methodology can potentially be employed in DPD and MDPD simulations where the coarse graining level is large to save on computational resources.
- The MDPD model together with the unit conversion methodology (scaling analysis) is found to be able to replicate experimental results within the range of 10% error. This is a strong validation of the MDPD model, which can then be used to study in detail the various parameters that affect nano-droplet formation.

- This is the first numerical study in nano-droplet formation in 3D nano-inkjet printing, performed via MDPD.
- Using the MDPD model, studies were conducted to determine the effects of temperature and pressure on nano-droplet formation. From this study, it was found that suitable temperature and pressure is important to generate and control the size and other physical parameters of the nano-droplets. The results in this study can be used as a possible guideline for experimental approach.

Part III: Numerical Study of Surface Agglomeration in 3D Nano-Inkjet Printing by MDPD

- For this next part of the thesis, it was observed that there is significant surface agglomeration (ink deposition on the nozzle's wall), which is identified to be a potential source of nozzle clogging. This observation means that MDPD can capture and further investigate surface agglomeration effects. This is the first time such type of surface agglomeration effects is numerically studied.
- This is also the first MDPD work that compares the simulation results from implicit (all MDPD parameters from pure optimization) and more realistic explicit (MDPD parameters from optimization and calculation) methods. In

previous MDPD studies, either implicit or explicit methods are usually used, but this work discusses the strengths and limitations of both methods.

- Surfactants were added to our MDPD model, and the resulting system can capture the suitable range of surfactant amount in commercial applications. Both explicit and implicit methods show that there is a saturation point and there is no further improvement of its performance beyond this point. Thus, only small amount of surfactants is sufficient to reach the maximum performance of surfactant in reducing ink deposition. This can potentially be useful information in actual experimental testing or applications.
- From this study, it was also found that combination of surfactants and further physical or chemical de-agglomeration techniques is necessary to reduce and control surface agglomeration at this very small scale. Again, this is new information that could potentially be applied to future development of 3D nano-inkjet printing.
- Finally, the study was extended to investigate the effects of adding surfactants to the nano-droplet formation phenomenon. It was found that the amount of surfactants can slightly affect total kinetic energy of ink compositions, nano-droplet velocity and nano-droplet breakup time during nano-droplet formation. This can be used as a guide for future experimental work.

In summary, this thesis proves that DPD and MDPD are potential mesoscale simulation techniques that can be used to successfully study and investigate on further phenomena related to 3D nano-inkjet printing. As an example, they can be used to model nano-droplet wetting on a substrate that is shown in the section on possible future work.

6.3 LIMITATIONS OF DPD & MDPD METHODS

DPD simulation method has two main limitations on its performance. The first limitation is that DPD works well with periodic boundary conditions because DPD has only repulsive force. If it works without periodic boundary conditions, then, the simulation system will keep expanding with meaningless trajectory. For the second limitation, DPD is suitable for only liquid-liquid phase simulation in the reason that there is pure repulsive force as the same as the first limitation and the repulsion of DPD can only be obtained by the calculation of solubility parameter and molar volume.

As the upgrade version of DPD, the intention of MDPD is to overcome DPD's limitations in simulation of different phases other than liquid-liquid phase simulation, solid-liquid interphase and vapor-liquid coexistence. The attractive force is added to MDPD and all interaction parameters of standard MDPD simulation can be achieved by optimization under its standard range of values. Apart from optimization, there is an alternative to estimate liquid-liquid attraction in MDPD. This is by modifying the DPD's repulsion parameter calculation in order to compute the liquid-liquid attraction parameter instead while other MDPD interaction parameters are still obtainable via optimization and standard MDPD values. However, MDPD still needs more development in order to have proper calculation for all interaction parameters of different phases. With acceptable standard of its interaction parameters, MDPD will be one of the most powerful simulation methods in mesoscale.

6.4 POSSIBLE FUTURE WORK

MDPD simulation techniques are found to be very suitable for studying nano-droplet formation in 3D nano-inkjet printing and problems associated with nozzle clogging. Apart from what has been studied in this thesis, other important phenomena such as nano-droplet wetting on a substrate can also pose significant technological challenges in 3D nano-inkjet printing. Although the printing technology and solidification process of 3D printing and expected 3D nano-printing technologies may be the same by using UV curable ink and UV light as the ink and source of solidification respectively, but nanoscale phenomena and its physical parameters are necessary to be considered and investigated because of the significant change in length and time scale. Important physical parameters in nano-droplet wetting on a substrate, such as contact angle, impact velocity, and jetting distance can be rapidly characterized using MDPD simulations. It is relatively obvious that DPD and MDPD simulation methods can reduce the difficulty and cost of experimental approaches while establishing possible guidelines for further research and development of 3D nano-inkjet printing.

6.4.1 Nano-Droplet Wetting on a Substrate

In order to complete the printing process, nano-droplet wetting on a substrate is an interesting topic to be studied as the next phenomenon after nano-droplet formation. Similar to nano-droplet formation, MDPD can simulate the solid-liquid interphase between nano-droplet and nozzle's wall. The simulation can be started

from nano-droplet formation until it reaches on a substrate and the wetting is fully developed. Two interesting investigations are done as preliminary part of this study. First, MDPD presents the relationship between contact angle and solid-liquid attraction parameter in Figure 6.1. When the attraction is increased in Figure 6.2, the contact angle becomes bigger. In Figure 6.3, another investigation reveals that higher solid-liquid attraction parameter reduces nano-droplet impact velocity and time in equilibration of the nano-droplet's dynamics on the substrate.

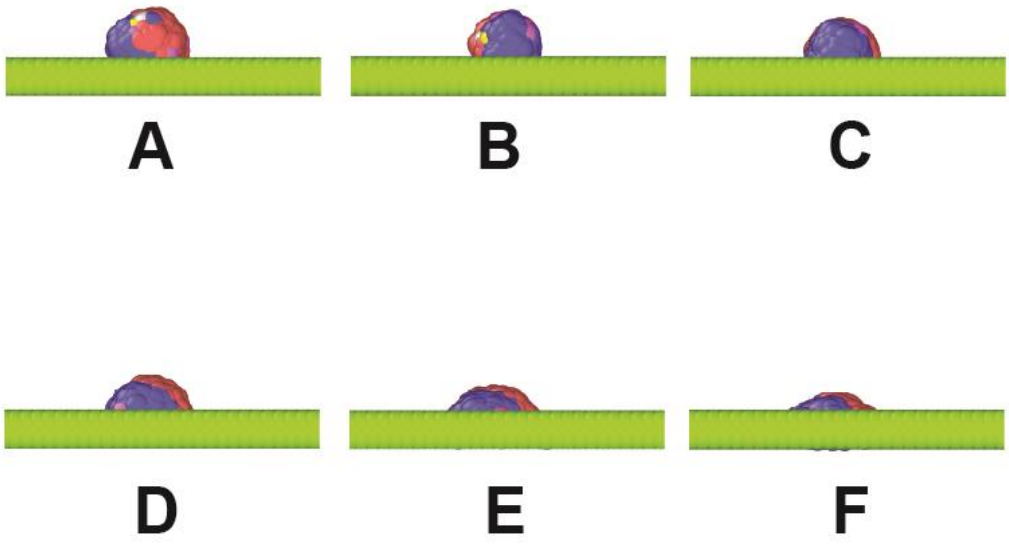

Figure 6.1: Effect of solid-liquid attraction on contact angle in nano-droplet wetting on a substrate, PEG (red-monomer, oligomer), PS (blue-monomer, oligomer), surfactant (white-H, yellow-T) and photo-initiator (pink). **(A)** Asl = -10 **(B)** Asl = -15 **(C)** Asl = -20 **(D)** Asl = -25 **(E)** Asl = -30 **(F)** Asl = -35.

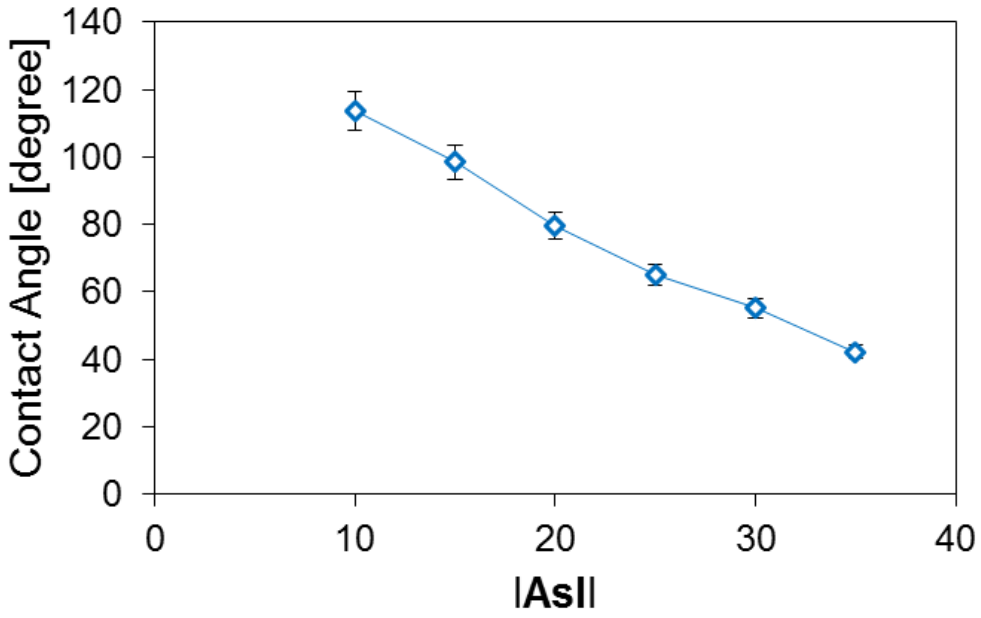

Figure 6.2: Effect of solid-liquid attraction on contact angle in nano-droplet wetting on a substrate.

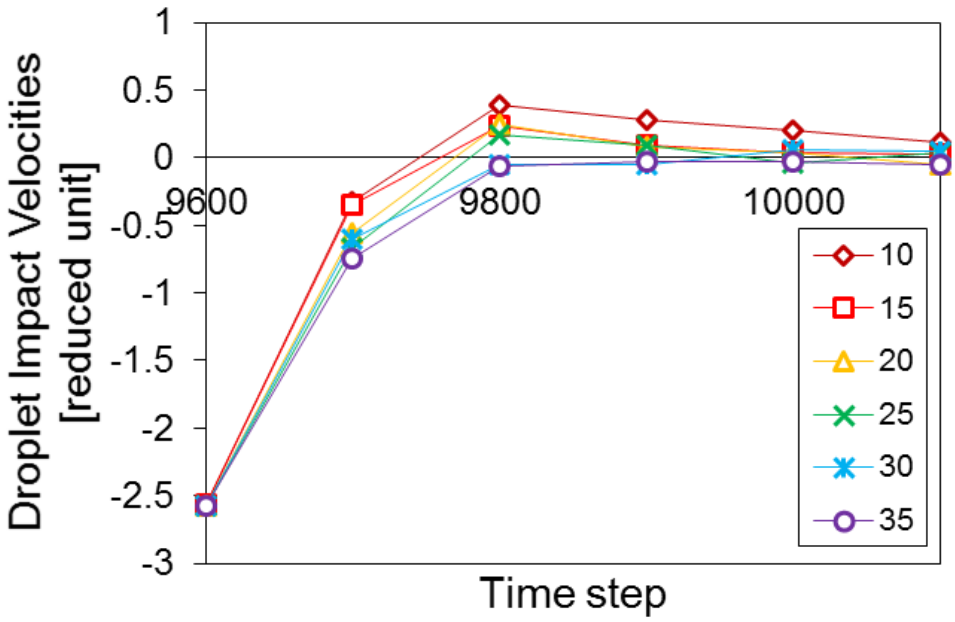

Figure 6.3: Effect of solid-liquid attraction on impact velocity of nano-droplet wetting on a substrate.

6.4.2 Developing MDPD's Proper Calculation for Solid-Liquid Interaction

Due to MDPD limitations, MDPD simulation can be performed by using parameters based on optimization. Even the calculation for liquid-liquid attraction can imitate from DPD but there is no proper calculation for further attractions especially solid-solid and solid-liquid attractions. If the proper calculation for these important parameters can be succeeded, then, MDPD can become a powerful simulation method in the range of mesoscale with more versatility in computation similarly to MD.

6.4.3 Further Studies on Agglomeration Problem

Because agglomeration problem is significantly severe for very small scale, thus, further studies on agglomeration problem can be extended in different ways. For examples, the effect of each physical parameters can be investigated in order to control sensitivity of the problem. MDPD can be used to observe agglomeration morphologies of special UV inks with more additives or more complicated compositions. Especially, when MDPD already has the proper calculation for its interaction parameters, the simulation results should be more accurate and provide better insights of agglomeration problem. Not only agglomeration problem but de-agglomeration techniques can also be effectively captured by the implementation of the proper MDPD interaction parameters' calculation with better theoretical compatability.

REFERENCES

1. ASTM Standard F2792-10, "Standard terminology for additive manufacturing technologies,",June 2010, ASTM International, West Conshohocken, PA.
2. *INTRODUCTION*, in *3D Printing and Additive Manufacturing*. 2014, WORLD SCIENTIFIC. p. 1-18.
3. Kruth, J.P., M.C. Leu, and T. Nakagawa, *Progress in Additive Manufacturing and Rapid Prototyping.* CIRP Annals - Manufacturing Technology, 1998. **47**(2): p. 525-540.
4. Wong, K.V. and A. Hernandez, *A Review of Additive Manufacturing.* ISRN Mechanical Engineering, 2012. **2012**: p. 10.
5. Bechmann, F., *Changing the future of additive manufacturing.* Metal Powder Report, 2014. **69**(3): p. 37-40.
6. Melchels, F.P.W., et al., *Additive manufacturing of tissues and organs.* Progress in Polymer Science, 2012. **37**(8): p. 1079-1104.
7. Sachs, E., M. Cima, and J. Cornie, *Three-Dimensional Printing: Rapid Tooling and Prototypes Directly from a CAD Model.* CIRP Annals - Manufacturing Technology, 1990. **39**(1): p. 201-204.
8. Berman, B., *3-D printing: The new industrial revolution.* Business Horizons, 2012. **55**(2): p. 155-162.
9. Ru, C.L., Jun; Xie, Shaorong; Sun, Yu, *A review of non-contact micro- and nano-printing technologies.* Journal of Micromechanics and Microengineering, Volume 24, Issue 5, article id. 053001, 2014.
10. de Gans, B.J., P.C. Duineveld, and U.S. Schubert, *Inkjet Printing of Polymers: State of the Art and Future Developments.* Advanced Materials, 2004. **16**(3): p. 203-213.
11. Castrejón-Pita, J.R., et al., *Future, opportunities and challenges of inkjet technologies.* Atomization and Sprays, 2013. **23**(6): p. 571-595.
12. Stratasys Ltd., How PolyJet 3D Printing Works, 2016. All rights reserved. http://www.stratasys.com/3d-printers/technologies/polyjet-technology.

13. Changhai, R., et al., *A review of non-contact micro- and nano-printing technologies.* Journal of Micromechanics and Microengineering, 2014. **24**(5): p. 053001.
14. Ivanova, O., C. Williams, and T. Campbell, *Additive manufacturing (AM) and nanotechnology: promises and challenges.* Rapid Prototyping Journal, 2013. **19**(5): p. 353-364.
15. Luo, J., et al., *Modeling and characterization of metal droplets generation by using a pneumatic drop-on-demand generator.* Journal of Materials Processing Technology, 2012. **212**(3): p. 718-726.
16. Gysling, H.J., *Nanoinks in inkjet metallization — Evolution of simple additive-type metal patterning.* Current Opinion in Colloid & Interface Science, 2014. **19**(2): p. 155-162.
17. Amirzadeh, A., M. Raessi, and S. Chandra, *Producing molten metal droplets smaller than the nozzle diameter using a pneumatic drop-on-demand generator.* Experimental Thermal and Fluid Science, 2013. **47**(0): p. 26-33.
18. Faddoul, R., et al., *Inkjet printing of silver nano-suspensions on ceramic substrates – Sintering temperature effect on electrical properties.* Microelectronic Engineering, 2013. **105**(0): p. 31-39.
19. Prasad, P.S.R.K., et al., *Studies on rheology of ceramic inks and spread of ink droplets for direct ceramic ink jet printing.* Journal of Materials Processing Technology, 2006. **176**(1–3): p. 222-229.
20. Maleksaeedi, S., et al., *Property enhancement of 3D-printed alumina ceramics using vacuum infiltration.* Journal of Materials Processing Technology, 2014. **214**(7): p. 1301-1306.
21. Peymannia, M., et al., *Production of a stable and homogeneous colloid dispersion of nano CoAl2O4 pigment for ceramic ink-jet ink.* Journal of the European Ceramic Society, 2014. **34**(12): p. 3119-3126.
22. Chovancova, V., A. Pekarovicova, and P.D. Fleming, *Hot Melt Inks for 3D Printing.* NIP & Digital Fabrication Conference, 2005. **2005**(3): p. 143-147.
23. van den Berg, A.M.J., et al., *Inkjet printing of polyurethane colloidal suspensions.* Soft Matter, 2007. **3**(2): p. 238-243.
24. Aurore, D., et al., *The influence of carbon nanotubes in inkjet printing of conductive polymer suspensions.* Nanotechnology, 2009. **20**(38): p. 385701.

25. Le, H.P., *Progress and Trends in Ink-jet Printing Technology.* Journal of Imaging Science and Technology, 1998. **42**(1): p. 49-62.
26. Andrew, H. and L. Long, *Challenges of UV curable ink-jet printing inks – a formulator's perspective.* Pigment & Resin Technology, 2004. **33**(5): p. 280-286.
27. Bentley, P.G., *Inkjet printing using solvent-based ink compositions*. 2008, Google Patents.
28. Hudd, A., *Inkjet Printing Technologies*, in *The Chemistry of Inkjet Inks*. 2011, WORLD SCIENTIFIC. p. 3-18.
29. Hancock, A. and L. Lin, *Challenges of UV curable ink-jet printing inks – a formulator's perspective.* Pigment & Resin Technology, 2004. **33**(5): p. 280-286.
30. Pappas, S.P., *UV curing by radical, cationic and concurrent radical-cationic polymerization.* Radiation Physics and Chemistry (1977), vol. 25, issue 4-6, pp. 633-641, 1985.
31. NAZDAR Ink Technologies, *Ultraviolet Curable Inks Technical Manual,*. www.nazdar.com.
32. Ifkovits, J.L. and J.A. Burdick, *Review: photopolymerizable and degradable biomaterials for tissue engineering applications.* Tissue Eng, 2007. **13**(10): p. 2369-85.
33. Kodaira, T., K. Hayashi, and T. Ohnishi, *Photopolymerization of Styrene in the Presence of Oxygen. Role of the Charge-Transfer Complex.* Polym J, 1973. **4**(1): p. 1-9.
34. Takagi, K., et al., *Synthesis of Branched Polystyrene by Photopolymerization of Selenium-Containing Styrene Monomer.* Polym J, 2000. **32**(11): p. 970-973.
35. Stratasys Ltd., PolyJet Material Selection Guide, 2015. All rights reserved. http://www.stratasys.com/materials/polyjet/compare-polyjet-materials.
36. Qiu, Y.-H., et al., *Ion and water transport in charge-modified graphene nanopores.* Chinese Physics B, 2015. **24**(10): p. 108201.
37. Di Risio, S., *Fundamental Investigation of Inkjet Deposition and Physical Immobilization of Horseradish Peroxidase on Cellulosic Substrates.* Doctoral Thesis, 2009. **handle:1807/26455**.
38. Yang, C. and Z.-G. Yang, *Synthesis of low viscosity, fast UV curing solder resist based on epoxy resin for ink-jet printing.* Journal of Applied Polymer Science, 2013. **129**(1): p. 187-192.

39. Li, X., et al., *3D-Printed Biopolymers for Tissue Engineering Application.* International Journal of Polymer Science, 2014. **2014**: p. 13.
40. Serra, T., et al., *Relevance of PEG in PLA-based blends for tissue engineering 3D-printed scaffolds.* Mater Sci Eng C Mater Biol Appl, 2014. **38**: p. 55-62.
41. Bose, S., S. Vahabzadeh, and A. Bandyopadhyay, *Bone tissue engineering using 3D printing.* Materials Today, 2013. **16**(12): p. 496-504.
42. Guo, X., et al., *A New Strategy of Lithography Based on Phase Separation of Polymer Blends.* Scientific Reports, 2015. **5**: p. 15947.
43. Kim, J.-K., et al., *Periodic Porous Stripe Patterning in a Polymer Blend Film Induced by Phase Separation during Spin-Casting.* Langmuir, 2008. **24**(16): p. 8898-8903.
44. Banhart, J., *Manufacture, characterisation and application of cellular metals and metal foams.* Progress in Materials Science, 2001. **46**(6): p. 559-632.
45. Taki, K., et al., *CO2 foaming of poly(ethylene glycol)/polystyrene blends: Relationship of the blend morphology, CO2 mass transfer, and cellular structure.* Journal of Applied Polymer Science, 2005. **97**(5): p. 1899-1906.
46. van Dongen, S.F.M., et al., *A Block Copolymer for Functionalisation of Polymersome Surfaces.* Macromolecular Rapid Communications, 2008. **29**(4): p. 321-325.
47. Egli, S., et al., *Biocompatible functionalization of polymersome surfaces: a new approach to surface immobilization and cell targeting using polymersomes.* J Am Chem Soc, 2011. **133**(12): p. 4476-83.
48. Iguerb, O. and P. Bertrand, *Graft photopolymerization of polyethylene glycol monoacrylate (PEGA) on poly(methyl methacrylate) (PMMA) films to prevent BSA adsorption.* Surface and Interface Analysis, 2008. **40**(3-4): p. 386-390.
49. Lu, Z., X. Huang, and J. Huang, *Synthesis and characterization of amphiphilic diblock copolymer of polystyrene and polyvinyl alcohol using ethanolamine–benzophenone as photochemical binary initiation system.* Journal of Polymer Science Part A: Polymer Chemistry, 1998. **36**(1): p. 109-115.
50. Singer, M.M. and R.S. Tjeerdema, *Fate and effects of the surfactant sodium dodecyl sulfate.* Rev Environ Contam Toxicol, 1993. **133**: p. 95-149.
51. Sigma-Aldrich, All Rights Reserved. https://www.sigmaaldrich.com
52. Kodas, Toivo T. (Toivo Tarmo) & Hampden-Smith, Mark J (1999). Aerosol processing of materials. Wiley, New York.

53. Hofmann, T. and F. von der Kammer, *Particles in Water. Properties and Processes. Edited by John Gregory.* Angewandte Chemie International Edition, 2007. **46**(20): p. 3611-3611.
54. Özcan-Taşkin, N.G., G. Padron, and A. Voelkel, *Effect of particle type on the mechanisms of break up of nanoscale particle clusters.* Chemical Engineering Research and Design, 2009. **87**(4): p. 468-473.
55. Peng, Z., E. Doroodchi, and G. Evans, *DEM simulation of aggregation of suspended nanoparticles.* Powder Technology, 2010. **204**(1): p. 91-102.
56. G. Inci, A. Arnold, A. Kronenburg, and R. Weeber, "Modelling nano-particle agglomeration using local interactions". Aerosol Sci. Technol., under review (2014).
57. Chen, S. and G.D. Doolen, *Lattice Boltzmann method for fluid flows.* Annual review of fluid mechanics, 1998. **30**(1): p. 329-364.
58. Koumoutsakos, P., *MULTISCALE FLOW SIMULATIONS USING PARTICLES.* Annual Review of Fluid Mechanics, 2005. **37**(1): p. 457-487.
59. Monaghan, J.J., *Smoothed Particle Hydrodynamics.* Annual Review of Astronomy and Astrophysics, 1992. **30**(1): p. 543-574.
60. Binder, C., et al., *Simulation of the hydrodynamic drag of aggregated particles.* Journal of Colloid and Interface Science, 2006. **301**(1): p. 155-167.
61. Cundall, P.A. and O.D.L. Strack, *A discrete numerical model for granular assemblies.* Géotechnique, 1979. **29**(1): p. 47-65.
62. Kroupa, M., et al., *Discrete Element Modeling (DEM) of Agglomeration of Polymer Particles.* Procedia Engineering, 2012. **42**(0): p. 58-69.
63. Fermi, E., et al., *Los Alamos Report No.* LA-1940, 1955. **978**.
64. Rahman, A., *Correlations in the Motion of Atoms in Liquid Argon.* Physical Review, 1964. **136**(2A): p. A405-A411.
65. Allen, M.P. and D.J. Tildesley, *Computer simulation of liquids*. 1989: Clarendon Press. 385.
66. Fermeglia, M. and S. Pricl, *Multiscale molecular modeling in nanostructured material design and process system engineering.* Computers & Chemical Engineering, 2009. **33**(10): p. 1701-1710.
67. Groot, R.D. and K.L. Rabone, *Mesoscopic Simulation of Cell Membrane Damage, Morphology Change and Rupture by Nonionic Surfactants.* Biophysical Journal, 2001. **81**(2): p. 725-736.

68. MOEENDARBARY, E., T.Y. NG, and M. ZANGENEH, *DISSIPATIVE PARTICLE DYNAMICS: INTRODUCTION, METHODOLOGY AND COMPLEX FLUID APPLICATIONS — A REVIEW.* International Journal of Applied Mechanics, 2009. **01**(04): p. 737-763.

69. Dünweg, B.L., Anthony J. C., *Lattice Boltzmann Simulations of Soft Matter Systems.* Advanced Computer Simulation Approaches for Soft Matter Sciences III, Advances in Polymer Science, Volume 221. ISBN 978-3-540-87705-9. Springer Berlin Heidelberg, 2009, p. 89, 2009.

70. Pastorino, C., et al., *Comparison of Dissipative Particle Dynamics and Langevin thermostats for out-of-equilibrium simulations of polymeric systems*. Vol. 76. 2007. 026706.

71. Dünweg, B. and A.J.C. Ladd, *Lattice Boltzmann Simulations of Soft Matter Systems*, in *Advanced Computer Simulation Approaches for Soft Matter Sciences III*, C. Holm and K. Kremer, Editors. 2009, Springer Berlin Heidelberg: Berlin, Heidelberg. p. 89-166.

72. Fiedler, S.L., S. Izvekov, and A. Violi, *The effect of temperature on nanoparticle clustering*. Carbon, 2007. **45**(9): p. 1786-1794.

73. JIMÉNEZ, J.F.C., *PARTICLE AGGLOMERATION IN FLOW MODELLED WITH MOLECULAR DYNAMICS COUPLED TO A THERMAL LATTICE BOLTZMANN CODE*. TASK QUARTERLY, 2013. **17**(3-4): p. 181-213.

74. Eggersdorfer, M.L., et al., *Aggregate Morphology Evolution by Sintering: Number & Diameter of Primary Particles.* Journal of aerosol science, 2012. **46**: p. 7-19.

75. Wu, M.K. and S.K. Friedlander, *Note on the Power Law Equation for Fractal-like Aerosol Agglomerates.* Journal of Colloid and Interface Science, 1993. **159**(1): p. 246-248.

76. Weber, A.P., *Characterization of Metallic Nanoparticle Agglomerates*, in *Metal Nanopowders*. 2014, Wiley-VCH Verlag GmbH & Co. KGaA. p. 107-132.

77. Goudeli, E., M.L. Eggersdorfer, and S.E. Pratsinis, *Coagulation-agglomeration of fractal-like particles: structure and self-preserving size distribution.* Langmuir, 2015. **31**(4): p. 1320-7.

78. Eggersdorfer, M.L. and S.E. Pratsinis, *The Structure of Agglomerates consisting of Polydisperse Particles.* Aerosol science and technology : the journal of the American Association for Aerosol Research, 2012. **46**(3): p. 347-353.

79. To, D., et al., *Deagglomeration of nanoparticle aggregates via rapid expansion of supercritical or high-pressure suspensions.* AIChE Journal, 2009. **55**(11): p. 2807-2826.
80. Zhu, W., et al., *Atomistic simulation study of surfactant and polymer interactions on the surface of a fenofibrate crystal.* European Journal of Pharmaceutical Sciences, 2011. **42**(5): p. 452-461.
81. Biswas, N. and A. Datta, *Polymer entanglement – A barrier to nanoparticles aggregation.* Chemical Physics Letters, 2012. **531**(0): p. 177-182.
82. Ding, P. and A.W. Pacek, *De-agglomeration of goethite nano-particles using ultrasonic comminution device.* Powder Technology, 2008. **187**(1): p. 1-10.
83. Guillemin, J.P., et al., *A mass conservative approach to model the ultrasonic de-agglomeration of ZnO nanoparticle suspension in water.* Powder Technology, 2012. **219**(0): p. 59-64.
84. Doktycz, S.J. and K.S. Suslick, *Interparticle collisions driven by ultrasound.* Science (New York, N.Y.), 1990. **247**(4946): p. 1067-1069.
85. Mandzy, N., E. Grulke, and T. Druffel, *Breakage of TiO 2 agglomerates in electrostatically stabilized aqueous dispersions.* Powder Technology, 2005. **160**(2): p. 121-126.
86. Greenwood, R. and K. Kendall, *Selection of suitable dispersants for aqueous suspensions of zirconia and titania powders using acoustophoresis.* Journal of the European Ceramic Society, 1999. **19**(4): p. 479-488.
87. Tadros, T., *Electrostatic and Steric Stabilization of Colloidal Dispersions*, in *Electrical Phenomena at Interfaces and Biointerfaces*. 2012, John Wiley & Sons, Inc. p. 153-172.
88. Widegren, J. and L. Bergstrom, *The effect of acids and bases on the dispersion and stabilization of ceramic particles in ethanol.* Journal of the European Ceramic Society, 2000. **20**(6): p. 659-665.
89. Tantra, R., J. Tompkins, and P. Quincey, *Characterisation of the de-agglomeration effects of bovine serum albumin on nanoparticles in aqueous suspension.* Colloids and Surfaces B: Biointerfaces, 2010. **75**(1): p. 275-281.
90. Holmberg, K., D.O. Shah, and M.J. Schwuger, *Handbook of applied surface and colloid chemistry*. 2002: Wiley.
91. Izvekov, S. and G.A. Voth, *Multiscale coarse graining of liquid-state systems.* The Journal of Chemical Physics, 2005. **123**(13): p. -.

92. Pivkin, I.V., B. Caswell, and G.E. Karniadakisa, *Dissipative Particle Dynamics*, in *Reviews in Computational Chemistry*. 2010, John Wiley & Sons, Inc. p. 85-110.
93. Groot, R.D. and P.B. Warren, *Dissipative particle dynamics: Bridging the gap between atomistic and mesoscopic simulation.* The Journal of Chemical Physics, 1997. **107**(11): p. 4423-4435.
94. M.J. Buehler, Y. Yung, "Deformation and failure of protein materials in extreme conditions and disease", Nature Materials, Vol. 8(3), pp. 175-188, 2009.
95. Hoogerbrugge, P.J. and J.M.V.A. Koelman, *Simulating Microscopic Hydrodynamic Phenomena with Dissipative Particle Dynamics.* EPL (Europhysics Letters), 1992. **19**(3): p. 155.
96. Español, P. and P. Warren, *Statistical Mechanics of Dissipative Particle Dynamics.* EPL (Europhysics Letters), 1995. **30**(4): p. 191.
97. Español, P., M. Serrano, and I. Zuñiga, *Coarse-Graining of a Fluid and its Relation with Dissipative Particle Dynamics and Smoothed Particle Dynamic.* International Journal of Modern Physics C, 1997. **08**(04): p. 899-908.
98. Flekkøy, E.G. and P.V. Coveney, *From Molecular Dynamics to Dissipative Particle Dynamics.* Physical Review Letters, 1999. **83**(9): p. 1775-1778.
99. Flekkøy, E.G., P.V. Coveney, and G. De Fabritiis, *Foundations of dissipative particle dynamics.* Physical Review E, 2000. **62**(2): p. 2140-2157.
100. Kinjo, T. and S. Hyodo, *Linkage between atomistic and mesoscale coarse-grained simulation.* Molecular Simulation, 2007. **33**(4-5): p. 417-420.
101. Pool, R. and P.G. Bolhuis, *Can purely repulsive soft potentials predict micelle formation correctly?* Physical chemistry chemical physics : PCCP, 2006. **8**(8): p. 941-948.
102. Junghans, C., M. Praprotnik, and K. Kremer, *Transport properties controlled by a thermostat: An extended dissipative particle dynamics thermostat.* Soft Matter, 2008. **4**(1): p. 156-161.
103. Fan, X., et al., *Simulating flow of DNA suspension using dissipative particle dynamics.* Physics of Fluids, 2006. **18**.
104. Symeonidis, V., G.E. Karniadakis, and B. Caswell, *Schmidt number effects in dissipative particle dynamics simulation of polymers.* The Journal of Chemical Physics, 2006. **125**(18): p. -.

105. Groot, R.D. and T.J. Madden, *Dynamic simulation of diblock copolymer microphase separation.* The Journal of Chemical Physics, 1998. **108**(20): p. 8713-8724.

106. Maiti, A. and S. McGrother, *Bead--bead interaction parameters in dissipative particle dynamics: Relation to bead-size, solubility parameter, and surface tension.* The Journal of Chemical Physics, 2004. **120**(3): p. 1594-1601.

107. Gibson, J.B., K. Chen, and S. Chynoweth, *THE EQUILIBRIUM OF A VELOCITY-VERLET TYPE ALGORITHM FOR DPD WITH FINITE TIME STEPS.* International Journal of Modern Physics C, 1999. **10**(01): p. 241-261.

108. Hafskjold, B., C.C. Liew †, and W. Shinoda ‡, *Can such Long Time Steps Really be used in Dissipative Particle Dynamics Simulations?* Molecular Simulation, 2004. **30**(13-15): p. 879-885.

109. Warren, P.B., *Dissipative particle dynamics.* Current Opinion in Colloid & Interface Science, 1998. **3**(6): p. 620-624.

110. Besold, G., Vattulainen, I. T., Karttunen, M., & Polson, J. M. (2000). Towards better integrators for dissipative particle dynamics simulations. Physical Review E. Statistical, Nonlinear, and Soft Matter Physics, 62(6), R7611-R7614.

111. Shardlow, T. [2003] "Splitting for dissipative particle dynamics,"SIAM Journal of Scientific Computing, 24(4): 1267–1282.

112. Lowe, C.P., *An alternative approach to dissipative particle dynamics.* EPL (Europhysics Letters), 1999. **47**(2): p. 145.

113. Nikunen, P., M. Karttunen, and I. Vattulainen, *How would you integrate the equations of motion in dissipative particle dynamics simulations?* Computer Physics Communications, 2003. **153**(3): p. 407-423.

114. Vasileios, S., *A Seamless Approach to Multiscale Complex Fluid Simulation*, K. George Em and C. Bruce, Editors. 2005. p. 39-46.

115. Revenga, M., I. Zúñiga, and P. Español, *Boundary conditions in dissipative particle dynamics.* Computer Physics Communications, 1999. **121–122**(0): p. 309-311.

116. MOEENDARBARY, E., T.Y. NG, and M. ZANGENEH, DISSIPATIVE PARTICLE DYNAMICS IN SOFT MATTER AND POLYMERIC APPLICATIONS - A REVIEW. International Journal of Applied Mechanics, 2010. 02(01): p. 161-190.

117. Yun, Y., et al., *Polymer inkjet printing: Construction of three-dimensional structures at micro-scale by repeated lamination.* Macromolecular Research, 2009. **17**(3): p. 197-202.
118. Kong, Y., et al., *Effect of solvent quality on the conformation and relaxation of polymers via dissipative particle dynamics.* The Journal of Chemical Physics, 1997. **107**(2): p. 592-602.
119. Lees, A.W. and S.F. Edwards, *The computer study of transport processes under extreme conditions.* Journal of Physics C: Solid State Physics, 1972. **5**(15): p. 1921.
120. Pagonabarraga, I. and D. Frenkel, *Dissipative particle dynamics for interacting systems.* The Journal of Chemical Physics, 2001. **115**(11): p. 5015-5026.
121. Trofimov, S.Y., E.L.F. Nies, and M.A.J. Michels, *Thermodynamic consistency in dissipative particle dynamics simulations of strongly nonideal liquids and liquid mixtures.* The Journal of Chemical Physics, 2002. **117**(20): p. 9383-9394.
122. Warren, P.B., *Vapor-liquid coexistence in many-body dissipative particle dynamics.* Physical Review E, 2003. **68**(6): p. 066702.
123. Chen, C., et al., *A Many-Body Dissipative Particle Dynamics Study of Spontaneous Capillary Imbibition and Drainage.* Langmuir, 2010. **26**(12): p. 9533-9538.
124. Laboratories, S.N., et al., *A Mesoscale Study of Pinch-off Under High Strain*. 2012: United States. National Nuclear Security Administration.
125. Lin, T.H., et al. *Simulation and Analysis of Interfacial Wettability by Dissipative Particle Dynamics*. in *2006 1st IEEE International Conference on Nano/Micro Engineered and Molecular Systems*. 2006.
126. Yong, X., *Hydrodynamic Interactions and Entanglements of Polymer Solutions in Many-Body Dissipative Particle Dynamics.* Polymers, 2016. **8**(12): p. 426.
127. *Nanoscale Inkjet Printing : MIT Technology Review (2007,September 13). Retrieved from https://www.technologyreview.com/s/408664/nanoscale-inkjet-printing*.
128. *Park, J.-U., et al., Nanoscale Patterns of Oligonucleotides Formed by Electrohydrodynamic Jet Printing with Applications in Biosensing and Nanomaterials Assembly. Nano Letters, 2008. 8(12): p. 4210-4216.*
129. Park, J.-U., et al., *High-resolution electrohydrodynamic jet printing.* Nature Materials, 2007. **6**: p. 782.

130. Shuoran, C., et al., *Fabrication of Nanoscale Circuits on Inkjet-Printing Patterned Substrates.* Advanced Materials, 2015. **27**(26): p. 3928-3933.
131. Onses, M.S., et al., *Hierarchical patterns of three-dimensional block-copolymer films formed by electrohydrodynamic jet printing and self-assembly.* Nat Nanotechnol, 2013. **8**(9): p. 667-75.
132. Lee, M. and H.-Y. Kim, *Toward Nanoscale Three-Dimensional Printing: Nanowalls Built of Electrospun Nanofibers.* Langmuir, 2014. **30**(5): p. 1210-1214.
133. Lee, S.H., et al., *Fabrication of a 3 dimensional dielectrophoresis electrode by a metal inkjet printing method.* Micro and Nano Systems Letters, 2013. **1**(1): p. 5.
134. *Hancock, A. and L. Lin, Challenges of UV curable ink-jet printing inks – a formulator's perspective. Pigment & Resin Technology, 2004. 33(5): p. 280-286.*
135. Layani, M., I. Cooperstein, and S. Magdassi, *UV crosslinkable emulsions with silver nanoparticles for inkjet printing of conductive 3D structures.* Journal of Materials Chemistry C, 2013. **1**(19): p. 3244-3249.
136. Alan H. (2009) Inkjet Printing Technologies. In The Chemistry of Inkjet Inks, WORLD SCIENTIFIC, 3-18.
137. BIOVIA, BIOVIA Materials Studio, 2002-2016 DASSAULT SYSTÈMES - ALL RIGHTS RESERVED http://accelrys.com/products/collaborative-science/biovia-materials-studio/.
138. XU, H., et al., *THE SIMULATION OF POLYSTYRENE/NANOPARTICLES COMPOSITE MICROSPHERES USING DISSIPATIVE PARTICLE DYNAMICS.* Journal of Theoretical and Computational Chemistry, 2013. **12**(02): p. 1250111.
139. van der Meulen, M-J. (2015). Meniscus motion and drop formation in inkjet printing Enschede: Universiteit Twente DOI: 10.3990/1.9789036538282.
140. Hansen, C.M., *Hansen Solubility Parameters: A User's Handbook, Second Edition*. 2007: CRC Press.
141. Sakurai S. Control of morphology in block copolymers. Trends Polym Sci 1995; 3: 90–98
142. Dinner, A.R., T. Lazaridis, and M. Karplus, *Understanding β-hairpin formation.* Proceedings of the National Academy of Sciences of the United States of America, 1999. **96**(16): p. 9068-9073.
143. Lee, J. and S. Shin, *Understanding β-Hairpin Formation by Molecular Dynamics Simulations of Unfolding.* Biophysical Journal, 2001. **81**(5): p. 2507-2516.

144. Pieranski P(1980) Two-dimensional interfacial colloidal crys-tals, Physical Review Letters, vol. 45, no. 7, pp. 569–572.

.

145. Fiedler SL, Izvekov S, Violi A. (2007) The effect of temperature on nanoparticle clustering. Carbon, 45, 1786-1794.

146. Jensen, G.V., et al., *Direct Observation of the Formation of Surfactant Micelles under Nonisothermal Conditions by Synchrotron SAXS.* Journal of the American Chemical Society, 2013. **135**(19): p. 7214-7222.

147. Schreier, S., S.V.P. Malheiros, and E. de Paula, *Surface active drugs: self-association and interaction with membranes and surfactants. Physicochemical and biological aspects.* Biochimica et Biophysica Acta (BBA) - Biomembranes, 2000. **1508**(1): p. 210-234.

148. Plimpton, S., *Fast Parallel Algorithms for Short-Range Molecular Dynamics.* Journal of Computational Physics, 1995. **117**(1): p. 1-19.

149. Ghassemieh, E., H.K. Versteeg, and M. Acar, *The effect of nozzle geometry on the flow characteristics of small water jets.* Proceedings of the Institution of Mechanical Engineers, Part C: Journal of Mechanical Engineering Science, 2006. **220**(12): p. 1739-1753.

150. He, B., et al., *The roles of wettability and surface tension in droplet formation during inkjet printing*. Vol. 7. 2017.

151. Martínez, L., et al., *PACKMOL: A package for building initial configurations for molecular dynamics simulations.* Journal of Computational Chemistry, 2009. **30**(13): p. 2157-2164.

152. Lim, TC. Journal of Mathematical Chemistry (2003) 33: 29. https://doi.org/10.1023/A:1023243413549.

153. Sukhomlinov, S.V. and M.H. Müser, *Determination of accurate, mean bond lengths from radial distribution functions.* The Journal of Chemical Physics, 2017. **146**(2): p. 024506.

154. Jamali, S., et al., *Generalized mapping of multi-body dissipative particle dynamics onto fluid compressibility and the Flory-Huggins theory.* J Chem Phys, 2015. **142**(16): p. 164902.

155. *Application of many-body dissipative particle dynamics to determine liquid characteristics.* International Journal of Numerical Methods for Heat & Fluid Flow, 2015. **25**(7): p. 1619-1637.

156. Sirk, T., et al., *An enhanced entangled polymer model for dissipative particle dynamics*. Vol. 136. 2012. 134903.
157. Fan, X., et al., *Microchannel Flow of a Macromolecular Suspension*. Vol. 15. 2003. 11-21.
158. Symeonidis, V., G. Karniadakis, and B. Caswell, *Dissipative Particle Dynamics Simulations of Polymer Chains: Scaling Laws and Shearing Response Compared to DNA Experiments*. Vol. 95. 2005. 076001.
159. Liba, O., et al., *A dissipative particle dynamics model of carbon nanotubes.* Molecular Simulation, 2008. **34**(8): p. 737-748.
160. Füchslin, R.M., et al., *Coarse graining and scaling in dissipative particle dynamics.* The Journal of Chemical Physics, 2009. **130**(21): p. 214102.
161. Vaezi, M., H. Seitz, and S. Yang, *A review on 3D micro-additive manufacturing technologies.* The International Journal of Advanced Manufacturing Technology, 2013. **67**(5): p. 1721-1754.
162. Spenley, N.A., *Scaling laws for polymers in dissipative particle dynamics.* EPL (Europhysics Letters), 2000. **49**(4): p. 534.
163. Liu, H. and G. Cao, *Effectiveness of the Young-Laplace equation at nanoscale.* Scientific Reports, 2016. **6**: p. 23936.
164. He, B., et al., *The roles of wettability and surface tension in droplet formation during inkjet printing.* Scientific Reports, 2017. **7**(1): p. 11841.
165. Subramanian, V., et al., *High-Speed Printing of Transistors: From Inks to Devices.* Proceedings of the IEEE, 2015. **103**(4): p. 567-582.
166. Su, W., et al., *Fully inkjet-printed microfluidics: a solution to low-cost rapid three-dimensional microfluidics fabrication with numerous electrical and sensing applications.* Scientific Reports, 2016. **6**: p. 35111.
167. Simon, J.F., et al., *The industrial emergence of commercial inkjet printing.* European Journal of Innovation Management, 2014. **17**(2): p. 126-143.
168. Henry, C., J.-P. Minier, and G. Lefèvre, *Towards a description of particulate fouling: From single particle deposition to clogging.* Advances in Colloid and Interface Science, 2012. **185-186**(Supplement C): p. 34-76.
169. Aphinyan, S., et al., *Numerical characterization of ultraviolet ink fluid agglomeration and the surfactant effect in nanoinkjet printing.* Polymers for Advanced Technologies, 2017. **28**(9): p. 1057-1064.

170. Lehrsch, G.A., R.E. Sojka, and A.C. Koehn, *Surfactant effects on soil aggregate tensile strength.* Geoderma, 2012. **189-190**: p. 199-206.
171. Ghoufi, A., J. Emile, and P. Malfreyt, *Recent advances in Many Body Dissipative Particles Dynamics simulations of liquid-vapor interfaces.* The European Physical Journal E, 2013. **36**(1): p. 10.
172. Lee, A., et al., *Optimization of Experimental Parameters to Suppress Nozzle Clogging in Inkjet Printing.* Industrial & Engineering Chemistry Research, 2012. **51**(40): p. 13195-13204.
173. Meinhart, C.D. and H. Zhang, *The flow structure inside a microfabricated inkjet printhead.* Journal of Microelectromechanical Systems, 2000. **9**(1): p. 67-75.
174. Li, J., F. Rossignol, and J. Macdonald, *Inkjet printing for biosensor fabrication: combining chemistry and technology for advanced manufacturing.* Lab on a Chip, 2015. **15**(12): p. 2538-2558.
175. Van, D.G. and D. Tilemans, *Uv curable inkjet compositions for high-density print heads*. 2011, Google Patents.
176. De, M.R. and N. Willems, *Manufacturing of decorative surfaces by inkjet*. 2016, Google Patents.
177. Howald, N. and M. Rrahimi, *Radiation-curable acrylate-based ink-jet printing ink*. 2015, Google Patents.
178. Ylitalo, C.M., R.K. Thery, and R.L. Severance, *Ink jet ink compositions containing fluorochemical surfactants*. 2003, Google Patents.
179. Nakane, H. and J. Ito, *Uv-curable ink jet ink composition*. 2014, Google Patents.
180. Saleh, E., et al., *3D inkjet-printed UV-curable inks for multi-functional electromagnetic applications.* Additive Manufacturing, 2017. **13**(Supplement C): p. 143-148.
181. *Wetting at the nanoscale: A molecular dynamics study.* The Journal of Chemical Physics, 2017. **146**(11): p. 114704.
182. Ramiasa-MacGregor, M., et al., *Tuning and predicting the wetting of nanoengineered material surface.* Nanoscale, 2016. **8**(8): p. 4635-4642.
183. Chen, P., et al., *Diffusion and Directionality of Charged Nanoparticles on Lipid Bilayer Membrane.* ACS Nano, 2016. **10**(12): p. 11541-11547.
184. Richner, P., et al., *Charge effects and nanoparticle pattern formation in electrohydrodynamic NanoDrip printing of colloids.* Nanoscale, 2016. **8**(11): p. 6028-6034.

185. Changxue, X., et al., *Electric field-assisted droplet formation using piezoactuation-based drop-on-demand inkjet printing.* Journal of Micromechanics and Microengineering, 2014. **24**(11): p. 115011.

186. Ligon, S.C., et al., *Polymers for 3D Printing and Customized Additive Manufacturing.* Chemical Reviews, 2017. **117**(15): p. 10212-10290.

187. Hashemi Sanatgar, R., C. Campagne, and V. Nierstrasz, *Investigation of the adhesion properties of direct 3D printing of polymers and nanocomposites on textiles: Effect of FDM printing process parameters.* Applied Surface Science, 2017. **403**: p. 551-563.